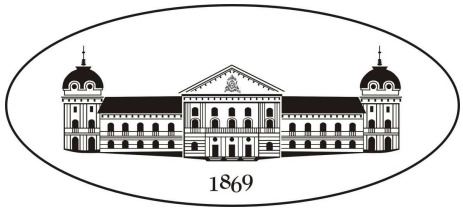

BULGARIAN ACADEMY OF SCIENCES

INSTITUTE OF ASTRONOMY AND
NATIONAL ASTRONOMICAL OBSERVATORY

Stellar systems in the Local group: Large Magellanic Cloud star clusters

Grigor Boykov Nikolov

Supervisor: Dr. Haralambi Markov

Advisor: Dr. Mary Kontizas

A thesis submitted for the degree of

Doctor of Philosophy

Sofia, 2019

Acknowledgements

My deepest gratitude is to Mary Kontizas for all that I know about the Southern heavens I learned from her. My scientific supervisor Haralambi Markov deserves my very sincere gratitude for accepting the challenge to guide me to bring this research to a complete end. To Ilian Iliev and Ivanka Stateva I am grateful for the invaluable advices throughout my professional career. Nikola Petrov enlightened me about the work and the life of an astronomer. I am grateful to Petko Nedyalkov, Evgeni Ovcharov and all my colleagues at the Sofia University that they were able to share their knowledge formally and informally, and especially to Valeri Golev for all the support during my studies. To my colleagues from Athens - Antonios Karampelas, Evdokia Livanou, Ioannis Bellas-Velidis, and Evangelos Kontizas I am grateful for sharing the Greek way of life and the opportunities to work together, and particularly to Anastasios Dapergolas, who thought me what to do with HST data. To all my colleagues from the Institute - I do appreciate your support during the years of working together. And to my fellow colleagues - Maya Belcheva, Kiril Stoyanov, Plamen Nikolov, Georgi Latev, and Alexander Kurtenkov, thanks for the shared moments and ideas. This work was partially supported by Bulgarian National Science Fund project number КП-06-Н28/2. Finally, I would also like to express my gratefulness to my family - my sister and my mother for supporting me my whole life. My fiance Maria has my love and my most sincere appreciation for being next to me.

Contents

Chapter 1

Introduction

The Local Group of galaxies is a stable collection of more than two dozen systems. These are the only galaxies not moving away from us, of which the largest are the Andromeda Spiral, our Milky Way and the Triangulum Spiral. Next in order of size come the two Magellanic Cloud galaxies, M 32 and NGC 2005, the latter being satellites of the Andromeda galaxy. Most of the rest are dwarfs, some of them not much populous than the rich globular clusters but are much less symmetrical and well defined.

The Magellanic Clouds are part of so called Magellanic System which covers great area on the sky (Mathewson and Ford 1984) and includes the Large Magellanic Cloud (LMC) galaxy, the Small Magellanic Cloud (SMC) galaxy, the Bridge and the Magellanic Stream. The Magellanic Clouds are from particular importance because they host a big variety of astronomical objects: giant and dwarf stars, doubles and multiples, novae, star clusters and planetary nebulae, all studied for nearly a century (Bok 1966). The Magellanic Clouds are under intense exploration based on X-ray, UV, optical, infrared and radio observations. Regardless of the vast amount of available data the structure, history and evolution of this system is still a matter of debate.

The measured three-dimensional velocities of the two Clouds were found to be close to the escape velocity in a standard 10^{12} M$\odot$ Milky Way dark halo, meaning that the Clouds may be on their first passage, as suggested by Besla et al. (2007). Also, the relative velocity between the LMC and SMC as measured from HST as-

trometry (Kallivayalil et al. 2009) is large enough, leaving open the possibility that the Clouds may not be bound to each other.

1.1 The Large Magellanic Cloud

The LMC is the most luminous and most massive irregular galaxy in the Local group visible from the Southern hemisphere in the constellations Dorado and Mensa, spanning some 11 by 9 degrees. The proximity of the Large Magellanic Cloud allows us to resolve into single stars the youngest and the most compact star clusters, down to the sub–solar masses. Star clusters in the Milky Way and both Magellanic Clouds have been extensively studied, and direct comparison of the characteristics of these systems is possible.

The distance to the Large Magellanic Cloud is of great importance for establishing the scale of the Universe. Being relatively close to the Milky Way, many astronomical objects in the LMC can be spatially resolved and thoroughly studied, and their integrated properties then extrapolated to more distant and unresolved galaxies.

From various studies of Cepheid and RR Lyrae variables the distance modulus to the LMC is estimated to between 18.25 and 18.73 magnitudes, taking into account the geometry and tilt of the galaxy, with the centre of the LMC disk at $(m - M)_0 = 18.5$ mag. The two estimated distance moduli of 18.2 mag and 18.7 mag are considered to represent the "short" and the "long" LMC distance scale, which correspond to 45 kpc and 55 kpc, respectively, or 50 kpc for the LMC centre. It is well established, that the east side of the LMC is closer than the west part (Westerlund (1990) and references therein). The inclination of the LMC estimated by Choi et al. (2018) is 25.85 ± 0.19 degrees and the position angle is 149.23 ± 0.49 degrees, based on the galaxy population of red clump stars.

In a recent study Inno et al. (2016) estimated a distance modulus to the LMC of $(m - M)_0 = 18.48 \pm 0.10$ mag, in excellent agreement with the currently most accurate measurement of Pietrzyński et al. (2013), who derived LMC distance 49.97±0.19 (statistical) ±1.11 (systematic) kiloparsecs. We use this distance modulus as a first estimate when fitting isochrones or synthetic clusters to the observed stellar populations in Sections 6.1, 6.2 and 6.3.

1.2 Large Magellanic Cloud star clusters

Star clusters are the fundamental building blocks of a galaxy. Their physical characteristics bring valuable information not only on the processes of their own formation, but also on the history of the evolution of the galaxies they reside in. On the other hand, most stars are observed to form within clusters (probably 70% to 90% Lada and Lada (2003)). Therefore, understanding cluster formation is the key to understanding the processes of star formation in galaxies.

Star clusters are observed in all but the smallest Local Group galaxies. They span a wide range of ages, metallicities, masses and sizes (Grebel 2016) even in the LMC only (Kontizas et al. 1993). Weidner et al. (2010) showed that the irregular galaxies are more likely to form super-star clusters than the spiral galaxies, like the Milky Way. In the irregular galaxies the lack of large-scale rotation enables collapse of the giant molecular cloud into one massive cluster, whereas the disk-galaxies are more likely to form loose systems, like OB association.

The LMC galaxy contains about 4300 star clusters (Bica et al. 2008, 1999; Kontizas et al. 1990). Though modern star cluster searches can report thousands of newly discovered cluster candidates, the false detection rate can be rather high, reaching 90%, as noted by Piatti (2018). Many of the LMC clusters appear double or multiple systems with similarly old components (Bhatia and Hatzidimitriou 1988; Dieball et al. 2002), while only 56% of the pairs are expected due to chance superpositions on the sky. This can lead to the interpretation that the true binary clusters are much more common in LMC compared to the Milky Way. The distribution of the LMC clusters (Glatt et al. (2010); Kontizas and Kontizas (1991) shows the older objects to be outside the shell regions and the younger objects to be located along the rims and inter-cloud regions.

In the LMC, two main epochs of prominent cluster formation have been identified (e.g., Bertelli et al. (1992)), at > 9 Gyr ago and $\sim 3 - 4$ Gyr ago, but a lack of clusters with ages 5–9 Gyr can not be fully explained (Grebel 2016). During the past ~ 4 Gyr, star clusters have been forming continuously until the present epoch, giving the LMC the observed population of intermediate-age clusters. In the LMC a dozen globular clusters are found that are as old as the oldest Galactic globulars older than ~ 10 Gyr (Baumgardt et al. 2013; Olsen et al. 1998). In this Thesis we

study 4 old clusters in Section 5.2.

1.3 Dynamical processes and parameters in star clusters

A wide range of self-gravitating systems may be idealized as configurations of point masses interacting through gravity. The large number of stars in a star cluster allows for a representation of such systems through the Boltzmann collisionless equation. The main processes of the dynamical evolution are the deflection of stars due to the collective gravitational field of the system and the stellar encounters. In star clusters, and also in galaxies, the effects of interactions between individual stars accumulate gradually (Binney and Tremaine 1987).

Within a stellar system, the individual stellar encounters slowly perturb stars away from the trajectories they would have taken if the gravitational field were perfectly smooth; in effect the stars diffuse in the phase space away from their original orbits. After many such encounters the star eventually loses its memory of the original orbit, and finds itself on a wholly unrelated one. The characteristic time over which this loss of memory occurs is called *relaxation time*. In other words, the relaxation time T_{rlx} is the time over which the cumulative effect of stellar encounters becomes comparable to a star's initial velocity.

$$T_{rlx} \approx \frac{N}{10 \ln N} T_c \tag{1.1}$$

where v is the encounter velocity, T_c is the crossing time, and N is the number of stars in the system. Overall the stellar encounters lead to dynamical relaxation, a state where the system is in a "thermal" equilibrium.

In stellar systems with large N the relaxation time is much longer than the crossing time. The relaxation time is less than the crossing time only for systems with $N < 40$ (Binney and Tremaine 2008), therefore relaxation due to stellar encounters is expected to play an important role in the evolution of star clusters. A typical rich globular cluster has $N \simeq 10^5, T_c \simeq 10^5$ and lifetime of 10 Gyr, whereas a typical galaxy has 10^{11} stars and $T_c \simeq 100$ Myr but is less than 100 crossing times old, so

the cumulative effects of encounters between stars in a galaxy are insignificant.

Portegies Zwart and Chen (2008) find that the initial relaxation time for young clusters in the LMC ranges from 200 Myr to approx. 2 Gyr, and it does not change significantly with the evolution of a cluster. Their conclusions are based on simulations of clusters younger than 300 Myr, in the same age range as our young clusters sample presented in Section 5.1.

For a realistic dynamical model of globular clusters the following inequality needs to be satisfied (King 2008) between the crossing, relaxation and evolution times:

$$T_c \ll T_{rlx} \ll T_e \tag{1.2}$$

A typical stellar system contains stars with a wide range of masses. From the kinetic theory we know that encounters tend to produce *equipartition* of kinetic energy, to equalize the kinetic energy of different mass stars, rather than their velocity. On average, particles with large kinetic energy $\frac{1}{2}mv^2$ lose energy to particles with less kinetic energy. Since the mass can not change significantly, the energy is transferred through change of the velocity. In an ordinary system. e.g. a gas, this process leads to a state in which the mean-square velocity of a population of particles is inversely proportional to mass. By contrast, in a stellar system, massive stars that lose kinetic energy tend to have smaller velocities and fall deeper into the gravitational potential well. Conversely, less massive stars preferentially diffuse towards the outer parts of the stellar system, where the velocity dispersion may be smaller. This is what we call *mass segregation* in star clusters.

Bonnell and Davies (1998) showed that the timescale for mass segregation is well fitted by the cluster's relaxation time, T_{rlx}. This is the same result as is found for systems with three mass components by Spitzer and Shull (1975). Thus systems younger than T_{rlx} are not expected to be fully dynamically mass-segregated, although some degree of mass segregation might occur very early in their evolution (Allison et al. 2009a; McMillan et al. 2015, e.g.).

Sometimes an encounter gives a star enough energy to *escape* the stellar system. Thus, generally, there is a slow but irreversible leakage of stars from the system, so stellar systems gradually evolve towards a final state consisting of only two stars in a Keplerian orbit, all the others having escaped to infinity. The timescale over

which the stars "evaporate" in this way can be related to the relaxation timescale as $T_{evap} \simeq 140\, T_{rlx}$, as shown in Binney and Tremaine (2008). Thus, it is expected that a stellar system would lose a substantial fraction of its stars only after hundred times T_{rlx}.

King (2008) outlines the following basic assumptions in modelling a cluster. We consider a spherical cluster in which all motions are isotropic. A self-gravitating star cluster needs to be in equilibrium. First of all it needs to satisfy the Virial Theorem; and second - the velocity distribution has to correspond to the spatial density distribution in such a way that as the individual stars move around on their orbits, stars take the place of other stars in a way that the cluster dynamical stability is maintained.

1.3.1 King model

In 1962 King proposed an empirical formula that represents the radial density from the centre to the end of globular clusters and generally valid for spherically symmetrical systems, tidally truncated by external tidal field of the host galaxy. The corresponding theoretical model is developed in King (1965, 1966). It represents adequately the stellar distribution in the Milky Way globular clusters and also Sculptor-type dwarf galaxies.

The King model was introduced as:

$$f(r) = f_0 \left\{ \frac{1}{\sqrt{1 + (r/r_c)^2}} - \frac{1}{\sqrt{1 + (r_t/r_c)^2}} \right\}^2 \tag{1.3}$$

where r_c is a scale factor, called core-radius, r_t is the tidal-radius, and f_0 represents the central density. The ratio $c = log(r_t/r_c)$ is called "concentration parameter". While this model is derived empirically, it has solid physical basis (King 2008). The radial extent of a star cluster should be limited by the tidal field of the host galaxy, in the case of the Galactic globular clusters, this is the tidal field of the Milky Way. Any stars that reach this tidally defined radius will escape the cluster gravitational field. This spatial limitation imposes a cut-off on the maximum velocity a star in a cluster may have, and then below this limit a good assumption for the velocity

distribution of the stars is a Maxwellian, since the relaxation of the cluster tends to evolve the velocity distribution towards it. In the simplest possible case, that of an isotropic velocity distribution, this set of assumptions leads to a model, which agree very closely with the empirical King model developed in (King 1962, 1965, 1966). Such models are a simplification of a real cluster, since they are completely valid only for systems of equal mass stars with an isotropic velocity distribution. Still, they provide a valuable point of view for exploration of star cluster systems and their internal dynamics, as well as further investigation of more realistic models, such as multi-mass systems.

The importance of deriving King model structural parameters of Magellanic Clouds star clusters, and its implementation, is described thoroughly in the series of papers of Kontizas and Kontizas (1983), Kontizas (1984) and Kontizas et al. (1987). We have to emphasize that from ground-based observations, due to their wide field-of-view, the tidal radius is more reliably determined than the radius of the core. They suffer from severe crowding in the clusters central regions, which prevents the cores to be spatially resolved in stars, but can measure the surrounding of the cluster well beyond its tidal radius.

1.3.2 Elson, Fall & Freeman model

In a series of papers Elson et al. (1987, 1989) developed a theoretical power-law model which represents well the stellar distribution in young LMC clusters. The authors show that for clusters not truncated by an external tidal field of the host galaxy, the King models reduce to 1.4 at small radii. The model is represented analytically by the equation:

$$f(r) = f_0 \left(1 + \frac{r^2}{a^2}\right)^{-\gamma/2} \tag{1.4}$$

where f_0 is the central density, γ is the power-law slope, and a is a scale radius, connected to the cluster's core radius r_c as $r_c = a\sqrt{2^{(2/\gamma)} - 1}$

The Equation 1.4 reduces to a modified Hubble law for $\gamma = 2$, which is a good approximation of the King model for globular clusters (King 1966) not truncated by galactic tidal field.

1.4 Stellar mass segregation in star clusters

1.4.1 Dynamical or primordial

Stellar segregation in LMC clusters is reported as early as 1961 by Westerlund, who finds evidence of the most bright stars of NGC 2100 being concentrated in the innermost region of the cluster. Later Elson et al. (1987) also found indication of mass segregation for NGC 1866. Kontizas et al. (1998) find strong evidence of segregation in the young NGC 2098 determined from the mass function slope. Subramaniam et al. (1993) studied the spatial distribution of the stellar masses in five young LMC clusters. In one of those, namely NGC 1711, they found evidence of mass segregation, interpreted as indicating the different sites of formation of stars of different mass in the proto-cluster at its formation. In the present Thesis we report our results on NGC 1711 in Section 5.1.

The observed mass segregation in young star clusters could either indicate that energy equipartition was achieved faster than predicted by single-mass type of models, or that the segregation is primordial - the massive stars were formed preferentially near the centres of these clusters (Allison et al. 2009a; Lightman and Shapiro 1978).

Bonnell and Davies (1998) performed N-body simulations of massive young stellar clusters. The primary result of their investigation is that the massive stars that are found in the centre of very young clusters like the Orion Nebula Cluster cannot have formed in their outer regions. The mass of a star is to some degree a function of its initial position within a cluster, the more centrally located stars tending to have larger masses. The authors investigate the timescale necessary for mass segregation to occur, and thus to set constraints to the probable initial distribution (i.e., sites of formation) of the massive stars within the cluster. They argued that dynamical mass segregation occurs on timescale approximately equal to the cluster relaxation time T_{rlx} and during this process the cluster loses all traces of its initial condition.

Simon et al. (2007) have presented observations of the young SMC cluster NGC 346 from Spitzer Space Telescope. They found 111 embedded young stellar objects (YSOs), showing that star-formation is still ongoing in this region today. The most massive YSOs in their sample (if they are single objects) are located in the central

sub-clusters, presenting strong evidence for primordial mass segregation.

The mechanism invoked to explain primordial mass segregation relies mainly on the higher accretion rate for stars in the centres of young clusters. In such competitive accretion scenario, the higher the mass of the proto-star, the faster it accretes material from the surrounding cloud. However, the efficiency of this mechanism is still a matter of debate (Krumholz et al. (2005),Bonnell and Bate (2006)) and, more generally, the processes of massive star formation and feedback remain poorly understood.

1.4.2 How to investigate the mass segregation

It is commonly accepted that star formation does usually not occur in isolation but that a large majority of young stars, up to 90 %, are part of a cluster (Evans et al. 2009; Lada and Lada 2003). The dynamical evolution of a star cluster leaves a variety of imprints in the phase space of its stellar population which are good tracers of the *dynamical* age of the cluster. This quantity is in particular interesting when compared to the *physical* age. A higher dynamical than physical age means that observable dynamical imprints did not have enough time to evolve dynamically and thus must have been present - at least partially - already at the beginning. This is usually known as *primordial* origin.

One of the most widely discussed aspects of the dynamical evolution of young star clusters is that of mass segregation. From theoretical work it is well known that this process is inevitably entangled with the dynamical evolution of a self-gravitating system of at least two different mass components (Farouki et al. 1983; Khalisi et al. 2007; Spitzer 1969; Spurzem and Takahashi 1995). Due to energy equipartition – hence via two-body encounters – the more massive particles tend to settle towards the cluster centre over time while the lower-mass particles are preferentially pushed to the outer parts. However, it is a much more challenging task to identify mass segregation observationally in real objects than theoretically from "clean" numerical simulations. This is even more severe for young star clusters that are usually still embedded in their natal gas and the dynamical and physical age of which is much more difficult to estimate.

However, the investigation of mass segregation in young stellar systems is of

particular interest for a deeper understanding of the star formation process. These fundamental questions are part of the scientific discussion in this context: a) Do young star clusters (really) show mass segregation? b) Could the observed mass segregation have developed dynamically or can it be only explained by primordial origin? An investigation of these important aspects of the star formation process requires a tool that is at best independent of the method used to determine the stellar masses and independent of the geometry of the object, that provides an unambiguous measure and is equally well applicable to observational and numerical data. Note that also dynamical models have the equivalent problem to identify mass segregation clearly and quantitatively.

So far the following four parameters have been used mainly to investigate mass segregation in (young) star clusters:

- the slope of the differential mass function in different annuli around the cluster centre, M^d_{MF} (Bolte (1989); Hillenbrand (1997)),
- the slope of the cumulative mass function in different annuli around the cluster centre, M^c_{MF} (e.g. Hillenbrand and Hartmann (1998); Pandey et al. (1992)),
- the characteristic radius of different mass-groups of stars, M^{ch}_R (e.g. Farouki et al. (1983), effective radius by Gouliermis et al. (2009)),
- the length of the minimum spanning tree (MST) of different mass-groups, M^{Λ}_{MST} (Allison et al. (2009b))

Most of these methods suffer from several weaknesses. The first three, M^d_{MF} , M^c_{MF} , and M^{ch}_R , implicitly assume a spherical symmetry and thus depend on the determination of cluster centre. The first two of them introduce additional bias due to radial binning and uncertainties in deriving the slope of the mass function. Furthermore, M^d_{MF} suffers from uncertainties due to mass binning, see e.g. Stolte et al. (2006), for a comparison of M^d_{MF} and M^c_{MF} applied to observational data. There is a fundamental difference in the concept of the first and the last two methods: the former (M^d_{MF}) presents the mass distribution in different spatial volumes, while the (M^c_{MF}) is a measure of the spatial distribution of different sets of most massive stars. Consequently, M^{ch}_R and M^{Λ}_{MST} do not require a direct measure of stellar

masses but only a qualitative criterion for correct ordering. This property is a huge advantage in the face of observational data.

The minimum spanning tree method is not practical for the images we have used because of the irregular shape of WFPC2. Since we see the central region of the cluster and approximately two thirds of its surroundings we need to suggest spherical symmetry of the investigated clusters. Although the LMC clusters are known to have some small degree of ellipticity (Kontizas et al. 1989) we do not have a reason to expect that the various stars have different ellipticity. As a consequence, the ellipticity of a cluster will not change the interpretation of the results of this work.

Examining the core-radii variation of specific mass groups is widely used method for assigning mass segregation (Brandl et al. 1996; de Grijs et al. 2002a). Thus the M^c_{MF} is the preferred diagnostic for mass segregation in this Thesis.

1.5 Open clusters

According to King (2008) a relatively poor open cluster (about hundred stars) relaxes in just about the time it takes a star to cross it. The crossing time is of the order of the relaxation time for such a system and the inequality $T_c \ll T_{rlx}$ is not satisfied.

The LMC clusters that are discussed here in the context of radial density profiles and mass segregation are more rich in stars. The amount of detected stars in the images under exploration in this Thesis is of the order of several thousand. Even if we consider only cluster members (stars above the mean stellar background) then again the cluster population will surpass thousand stars or more.

1.6 Multiple stellar populations

The high precision photometry achievable with the instruments of HST allows derivation of unprecedentedly detailed color-magnitude diagrams even for clusters in the Magellanic Clouds. Such CMD accuracy revealed some unexpected features. The extended Main Sequence turn-of point (eMSTO) is such a feature observed in young MC clusters (ages of 1–2 Gyr), that could not be explained by photomet-

ric uncertainties or stellar binarity. It was firstly reported by Bertelli et al. (2003) and later found to be a common phenomenon in many young and intermediate age clusters (Bastian and Lardo 2018; Chantereau et al. 2019).

Li et al. (2014) studied the sub-giant branch morphology of NGC 1651, an eMSTO cluster with an age of $\approx$ 2 Gyr, and concluded that the observed eMSTO can be explained by a single-age stellar population. By using new stellar tracks, derived with and without stellar rotation of the stars in the region comprising MSTO and the sub-giants branch, the authors argued that eMSTOs in the intermediate-age clusters are most likely caused by significant dispersion in axial rotation of cluster members.

Bastian et al. (2016) in a study based on HST data reported that the apparent width observed in the CMD of NGC 1850 is due to significant dispersion in stellar rotation, not multiple populations. Then Bastian et al. (2017) indeed found a higher fraction of rapidly rotating Be stars in the cluster, between 30–60% near the MSTO, much higher than in the field. These observations support the idea that the split MS observed in some clusters is caused by a bi-modal rotational distribution. Recently Li et al. (2016) in a letter published in the "Nature" journal propose an accretion scenario for explaining the formation of multiple stellar populations in star clusters. Later Cabrera-Ziri et al. (2016b) showed that the apparent multiplicity in Li et al. (2016) paper can be explained by poor field star removal and not a real cluster populations.

An implication of multiple stellar population observed in LMC clusters is discussed in this Thesis in Section 6.2.

1.7 Motivation on this thesis

The processes of star clusters formation is not yet well understood. How does the star clusters form, what is their early evolution? Can a mass segregation be identified in young LMC clusters?

In this Thesis I will try to shed light on some of these topics. The goal is to use the superb resolving capabilities of the Hubble Space Telescope and the available archive observations to study the distribution of stars in sample of LMC clusters based on star-count radial density profiles. This allows for a mass segregation to be

investigated in the studied star clusters. The data for NGC 2004 and NGC 2031 provide also an opportunity for detailed study of their stellar populations and an age estimation using the latest theoretical models of stellar evolution.

Chapter 2

Observational data

In this work we use archival observations from the Hubble Space Telescope WFPC2 camera, obtained from the STScI[1]. This chapter presents the Hubble Space Telescope (HST), Wide-Field and Planetary Camera 2, datasets images used, the Space Telescope Science Institute (STScI) archive pipeline calibrations.

2.1 Hubble Space Telescope

The Hubble Space Telescope (HST) is a cooperative program of the European Space Agency (ESA) and the US National Aeronautics and Space Administration (NASA) to operate a space-based observatory for the benefit of the international astronomical community. HST is an observatory first envisioned in the 1960s (e.g. Spitzer 1968), designed and built in the 1970s and 1980s. HST is a 2.4-meter Ritchey-Chrétien telescope (see Figure 2.1), which was deployed in low-Earth orbit of 600 kilometers above the Earth, operational since the 1990 and scheduled to operate at least through 2020.

Responsibility for conducting and coordinating the science operations of the Hubble Space Telescope rests with the Space Telescope Science Institute on the Johns Hopkins University Homewood Campus in Baltimore, Maryland. STScI is operated for NASA by the Association of Universities for Research in Astronomy, Inc. (AURA).

[1] `http://archive.stsci.edu`

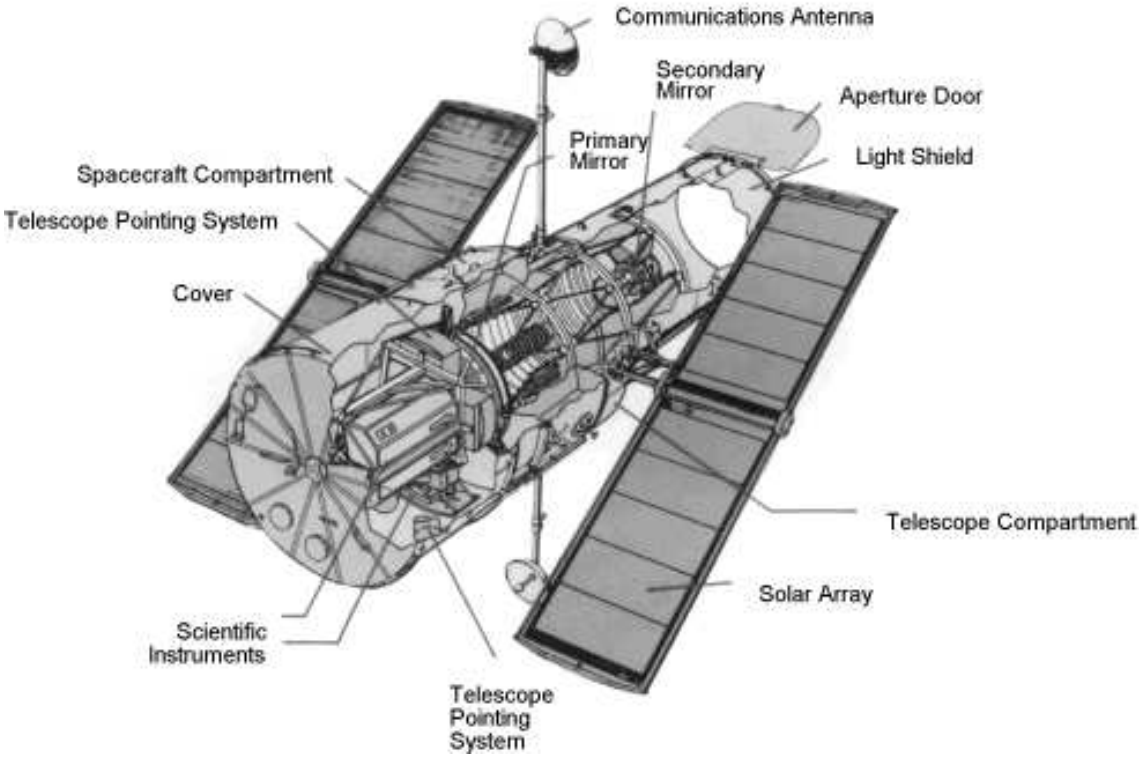

Figure 2.1: Scheme of the Hubble Space Telescope.

Because of HST's location above the Earth's atmosphere, its science instruments can produce sharp high-resolution images of astronomical objects. Most of the ground-based telescopes are limited in their resolution by the Earth's atmosphere, which causes a variable distortion in the images. Hubble can observe ultraviolet radiation, which is blocked by the atmosphere and therefore unavailable to ground-based telescopes, also in the infrared portion of the spectrum the Earth's atmosphere adds a lot of background, absent in Hubble observations.

2.1.1 WFPC2

The Wide Field and Planetary Camera 2 (WFPC2) was installed on-board HST during the first servicing mission in December 1993. It was the main imaging camera of HST until it was decommissioned in May 2009. The design of the camera is illustrated in Figure 2.3, as presented in McMaster and et al. (2008). This in-

strument is a two-dimensional imaging photometer which covers the spectral range between approximately 1150Å to 10500Å. The WFPC2 field-of-view is divided into four cameras by a four-faceted pyramid mirror near the HST focal plane. The configuration of the field-of-view of the camera is shown on Figure 2.2. Each of the four cameras contains an 800 by 800 pixel CCD detector with pixel physical size of 152 by 152μm. Three of the cameras have similar hardware configuration and comprise the Wide Field Camera (WFC) with an "L" shaped field-of-view. Every WFC detector operates at F/12.9 with a resolution of 0.1″ per pixel. The fourth camera operates at 0.0455″ per pixel (F/28.3) and is referred to as the Planetary Camera (PC). Thus, there are four sets of relay optics and CCD sensors in WFPC2. The four cameras are labeled PC, WF2, WF3, and WF4 in Figure 2.2. Each WFPC2 image is a mosaic of three WFC images with a scale of 0.1 arcsec per pixel and one PC image with a scale 0.0455 arcsec per pixel.

2.1.2 Dithering WFPC2 Observations

Although the optics of WFPC2 provide a superb PSF, the detectors at the focal plane undersample the image. This problem is most severe on the three WF chips, where the width of a pixel is comparable to the FWHM of the optics in the near-infrared, and exceeds it in the blue wavelengths. While some spatial frequency information in the image is permanently destroyed by smearing with the response of the pixels, the quality of the image can nevertheless be greatly improved by combining sub-pixel dithered images. In sub-pixel dithering, the pointing of the telescope is moved by small, non-integral pixel amounts between exposures. Typical shifts used in observations are of 5.5 pixels in both directions. Each of the pixels from the different exposures can then be thought of as sampling a final, higher-resolution image, which is the “true image" of the sky convolved with the optical PSF and the pixel-response function of the CCD. As a result, dithering allows one to regain a substantial fraction of the spatial information lost to undersampling in a single image.

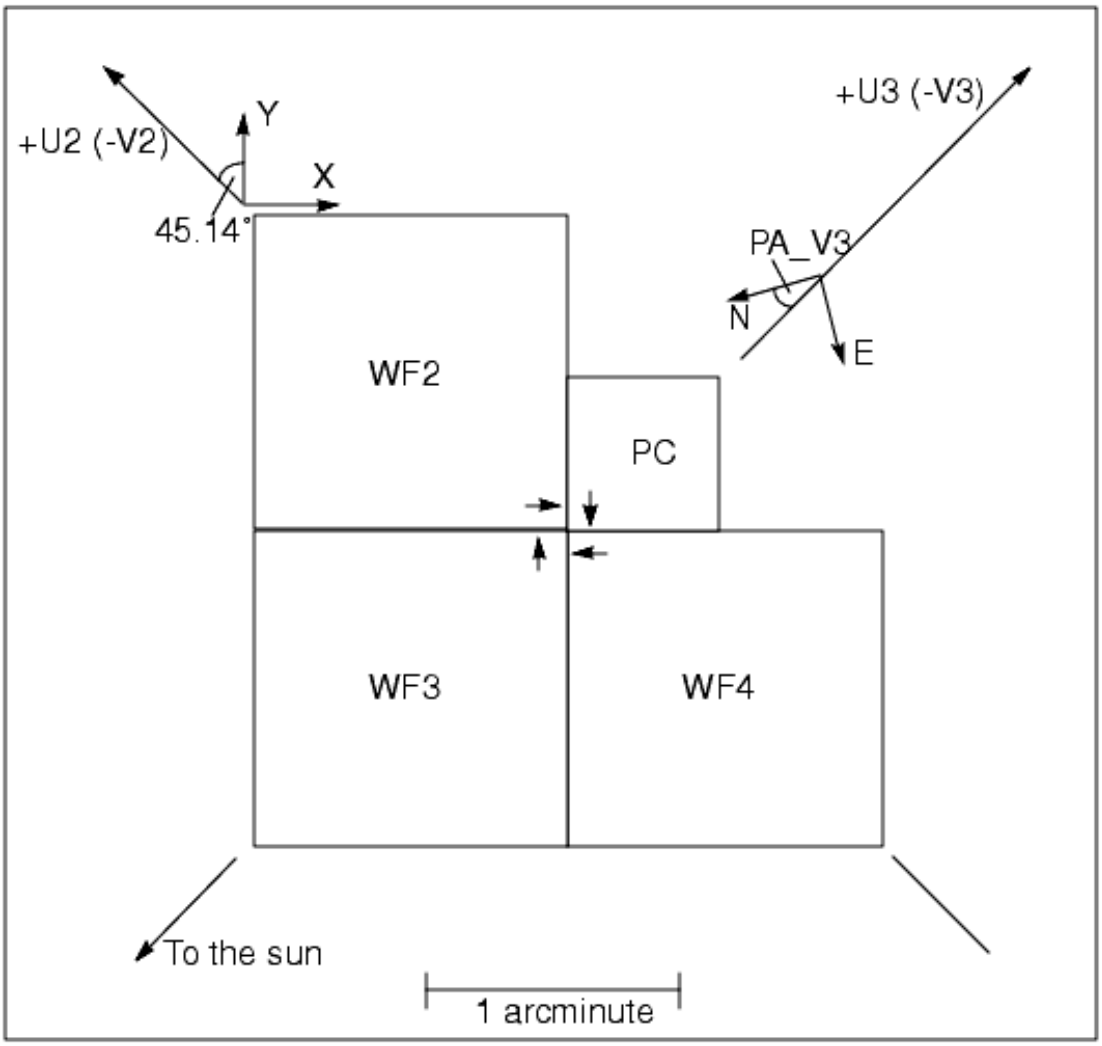

Figure 2.2: WFPC2 field-of-view projected on the sky. The readout direction is marked with arrows near the start of the first row in each CCD. The position angle of V3 varies with pointing direction and observation epoch, and is given in the calibrated science header by keyword PA_V3. The X–Y coordinate directions are the global coordinates directions with reference to the PC pixel (0,0).

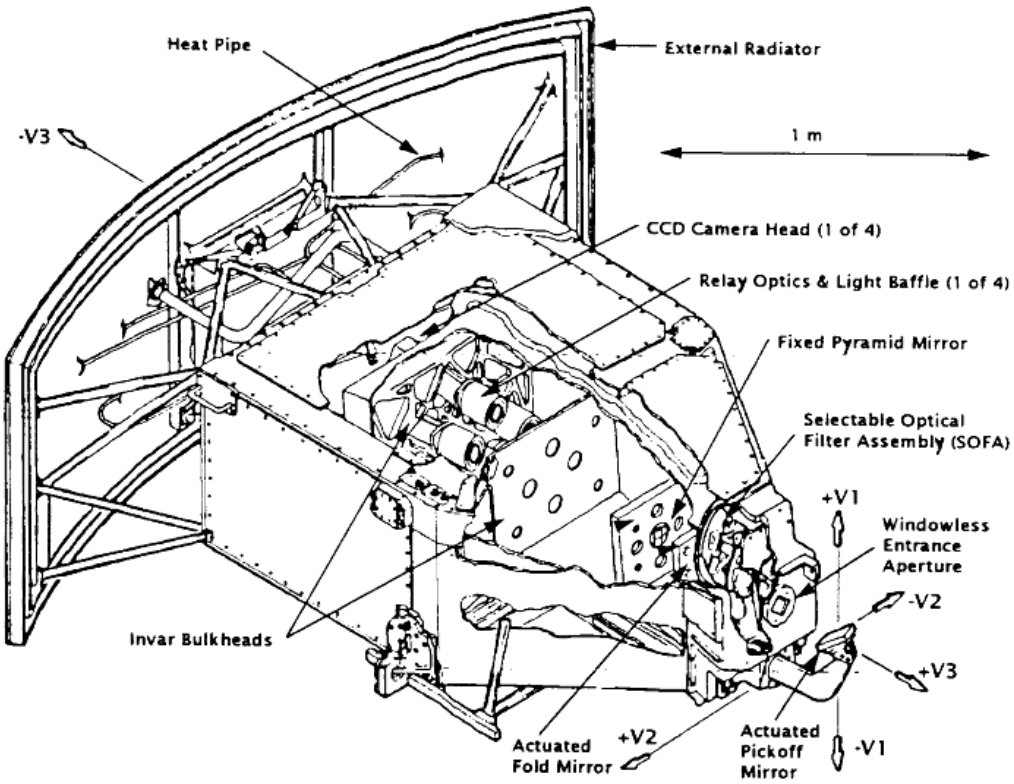

Figure 2.3: Wide Field and Planetary Camera 2 Concept Illustration, from WFPC2 Instrument Handbook Figure 2.1.

2.2 HST archive

The HST observations are freely available to the scientific community, distributed by STScI. The images used in this Thesis were calibrated with the final calibration procedures before decommissioning of WFPC2 and processed according to the standard HST pipeline. As a part of the preprocessing the images were corrected for bias level, dark current and flat-field. During this preprocessing a calibration output data quality file is generated (c1f), a mask that contains a map of all the known bad pixels and columns. The photometric study presented in this Thesis is based on photometry of the calibrated images (c0f) and their corresponding data quality masks.

2.3 Observations used

We use observations taken with two HST filters, namely F555W and F814W, which correspond to Johnson's V and I passbands. Wherever possible we used observations with long and short exposures, if available, to ensure faint stars to be well exposed but bright stars to not be saturated. When collecting observational data from the archive, a special care was taken in order to select the best-quality images from each proposal. From the available images only those with header keyword "QUALITY = 'OK'" (no errors during exposure e.g. guiding, telemetry or acquisition) were chosen. Details of the observations are presented in Table 2.1 and Table 2.2.

Table 2.1: Proposal IDs of the observations used.

PropID	PI Last Name	List of targets used.
8134	Nota	NGC 1984, NGC 2011, NGC 2214
5904	Fischer	BSDL 103, BSDL 101, NGC 1711, NGC 2004, NGC 2031
5916	Suntzeff	NGC 1754, NGC 1898, NGC 2005, NGC 2019

Table 2.2: List of the observations used.

Dataset name	Filter name	Exposure time [s]	Dataset name	Filter name	Exposure time [s]
BSDL 103 and BSDL 101					
U2Y8050JR	F555W	300	U2Y8050ER	F814W	300
U2Y8050KR	F555W	300	U2Y8050FR	F814W	300
U2Y8050LR	F555W	300	U2Y8050GR	F814W	300
U2Y8050HR	F555W	300	U2Y8050MR	F814W	300
U2Y8050IR	F555W	300	U2Y8050NR	F814W	290
NGC 1711					
U2Y80501M	F555W	300	U2Y80502R	F555W	300
U2Y80504R	F814W	300	U2Y80505R	F814W	300
U2Y80506R	F814W	300	U2Y80507R	F814W	300
U2Y80508R	F814W	300	U2Y80509R	F555W	300
U2Y8050BR	F555W	10	U2Y8050CR	F555W	10
U2Y8050DR	F814W	10			
NGC 1754					
U2XQ0101T	F555W	20	U2XQ0102T	F555W	20
U2XQ0103T	F555W	500	U2XQ0104T	F555W	500
U2XQ0105T	F555W	500	U2XQ0106T	F814W	20
U2XQ010BT	F814W	600	U2XQ0107T	F814W	20
U2XQ0108T	F814W	20	U2XQ010AT	F814W	600
U2XQ0109T	F814W	600			
NGC 1898					
U2XQ0303T	F555W	500	U2XQ0304T	F555W	500
U2XQ0305T	F555W	500	U2XQ0301T	F555W	20
U2XQ0302T	F555W	20	U2XQ0309T	F814W	600
U2XQ030AT	F814W	600	U2XQ030BT	F814W	600
U2XQ0306T	F814W	20	U2XQ0307T	F814W	20
U2XQ0308T	F814W	20			
NGC 1984					
U5AY0901R	F555W	350	U5AY0902R	F555W	350
U5AY0903R	F555W	10	U5AY0904R	F814W	350
U5AY0905R	F814W	350	U5AY0906R	F814W	10
U5AY0907R	F814W	350	U5AY0908R	F814W	350
U5AY0909R	F555W	350	U5AY090AR	F555W	350
NGC 2004					

Continued on next page

Table 2.2: continued.

Dataset name	Filter name	Exposure time [s]	Dataset name	Filter name	Exposure time [s]
U2Y80201T	F555W	300	U2Y80202T	F555W	300
U2Y80203T	F555W	300	U2Y80204T	F814W	300
U2Y80205T	F814W	300	U2Y80206T	F814W	300
U2Y80207T	F814W	300	U2Y80208T	F814W	300
U2Y80209T	F555W	300	U2Y8020AT	F555W	300
U2Y8020BT	F555W	10	U2Y8020CT	F555W	10
U2Y8020DT	F814W	10			
NGC 2005					
U2XQ0501T	F555W	20	U2XQ0502T	F555W	20
U2XQ0503T	F555W	500	U2XQ0504T	F555W	500
U2XQ0505T	F555W	500	U2XQ0506T	F814W	20
U2XQ0507T	F814W	20	U2XQ0508T	F814W	20
U2XQ0509T	F814W	600	U2XQ050AT	F814W	600
U2XQ050BT	F814W	600			
NGC 2011					
U5AY0801R	F555W	350	U5AY0802R	F555W	350
U5AY0803R	F555W	10	U5AY0804R	F814W	350
U5AY0805R	F814W	350	U5AY0806R	F814W	10
U5AY0807R	F814W	350	U5AY0808R	F814W	350
U5AY0809R	F555W	350	U5AY080AR	F555W	350
NGC 2019					
U2XQ0601T	F555W	20	U2XQ0602T	F555W	20
U2XQ0603T	F555W	500	U2XQ0604T	F555W	500
U2XQ0605T	F555W	500	U2XQ0606T	F814W	20
U2XQ0607T	F814W	20	U2XQ0608T	F814W	20
U2XQ0609T	F814W	600	U2XQ060AT	F814W	600
U2XQ060BT	F814W	600			
NGC 2031					
U2Y80301T	F555W	300	U2Y80302T	F555W	300
U2Y80303T	F555W	300	U2Y80304P	F814W	300
U2Y80305P	F814W	300	U2Y80306P	F814W	300
U2Y80307P	F814W	300	U2Y80308P	F814W	300
U2Y80309P	F555W	300	U2Y8030AP	F555W	300
U2Y8030BP	F555W	10	U2Y8030CP	F555W	10

Continued on next page

Table 2.2: continued.

Dataset name	Filter name	Exposure time [s]	Dataset name	Filter name	Exposure time [s]
U2Y8030DP	F814W	10			
NGC 2214					
U5AY0201R	F555W	350	U5AY0202R	F555W	350
U5AY0203R	F555W	10	U5AY0204R	F814W	350
U5AY0205R	F814W	350	U5AY0206R	F814W	10
U5AY0207R	F555W	350	U5AY0208R	F555W	350
U5AY0209R	F814W	350	U5AY020AR	F814W	350

Chapter 3

Photometry

3.1 HSTphot package

The photometry presented in this Thesis was done using HSTphot[1] (Dolphin 2000b) - a package designed especially for simultaneous point-spread function (PSF) photometry of multiple WFPC2 images. Photometric reductions with *HSTphot* follow the Stetson's recipe outlined in Stetson (1987), but optimized for the conditions of the WFPC2.

The calibrated science (c0f.fits) images obtained from the STScI archive, were first masked by the corresponding data quality mask (c1f.fits) to reject bad pixels with already known defects. Each individual science image was masked with its data quality mask provided during the pipeline calibration. Pixels with data quality values of 1 (decoding error), 2 (calibration file defect), 4 (permanent camera defect), 16 (missing data), 32 (bad pixel), 256 (questionable pixel), or 512 (unrepaired warm pixel), as well as saturated pixels, are rejected using the HSTphot routine *mask* and subsequently ignored.

3.1.1 Sky background determination

The image sky level was determined initially using the routine *getsky* - for each pixel the mean of neighbouring pixels' values found in a certain annulus was calculated, and then smoothed. There is an option in HSTphot for this estimated sky value

[1] `http://americano.dolphinsim.com/hstphot/`

to be recomputed and modified during the PSF photometry, thus ensuring a even better sky level estimation (Dolphin 2000b). The *getsky* routine determines the a priori sky value at each pixel, while *hstphot* can determine a modified sky value for a star immediately before the photometry solution and very close to the star, which we use in our investigations. In fields with rapidly-varying background, there is also an option to estimate a local sky for each individual star just outside the photometry aperture. Our experience showed that turning on that option does not improve the quality of the photometry (Nikolov 2018a), in some cases even making it worse by affecting the aperture corrections and photometric zeropoints for the camera. Besides, the background in the broad-band images we used is not rapidly-varying on small scales (order of arcsec) to demand a local sky determination but rather sky level modification during the PSF photometry was the preferred approach.

3.1.2 Hot pixels removal

Camera pixels, which have equally high signal in all images regardless of filter or exposure time, the "hot pixels", need to be removed from the images, since they will create false detections in the photometric data. The HSTphot routine *hotpixels* calculates the average and standard deviation of all eight adjacent pixels (after sky subtraction). If its value was 10 times higher than the average of the adjacent pixels and if it was above 7 times the standard deviation, the corresponding pixel was flagged as hot. This approach locates well hot pixels that are on blank sky, although the procedure will not recognize those that damage stellar images. These strict limits are used in order to avoid any chance of cutting off WFC stellar profiles, which can have very sharp peaks as well. If a hot pixel is found, it is flagged with a bad data value and ignored in subsequent photometric measurements.

3.1.3 Cosmic rays removal

The observations we used consist of several images per pointing and filter, allowing easy cosmic rays mitigation. To remove cosmic rays from dithered data one needs to obtain several exposures of similar length at each of the dither pointings and remove the cosmic rays from these positions separately using standard cosmic ray removal techniques. The individual images we use were grouped by filter, exposure time and

positioning. The HSTphot cosmic-ray rejection routine, *crmask* identifies cosmic rays on a pixel-by-pixel basis and flags cosmic rays by looking for pixels whose values significantly exceed those in other observations in the set. A registration factor of 1 and a σ-threshold of 3 were used. This registration factor is conservative, to ensure that images with fractional pixel shifts do not give rise to erroneous identification of cosmic rays. After the cosmic rays were removed from the images, then every 2 or more images with the same pointing, exposure time and filter were combined by the routine *coadd* to produce a single deep clean image ready for the photometry process.

3.1.4 Photometry

The photometric solutions were done by the HSTphot routine *hstphot*. It iteratively locates brightness peaks in the image using a grid of 5 by 5 pixels and tries to find a PSF solution for any such peak. The one that returns the smallest χ / S/N is selected as a star's centre with a sub-pixel accuracy. The point-spread functions for the filters we use are precomputed, tested and distributed with the HSTphot package.

The routine *hstphot* does the photometric solutions with detection threshold of 3.5σ. During the photometry two options have been turned on. The first re-fits the sky during the photometry, which is recommended for general use in the HSTphot manual, and the other does an artificial star tests (see below). The photometry done with HSTphot is corrected for the filter-dependent plate scale changes (Dolphin 2000b) and the 34-th row error (Anderson and King 1999; Shaklan et al. 1995), where every 34-th CCD pixel row is about 3% narrower due to a manufacturing peculiarity.

The output photometry list is provided in both instrumental and standard Johnson-Cousins system. Magnitudes in instrumental F555W filter are converted to standard V, and F814W – to I magnitudes during photometry, following the calibrated transformations of Dolphin (2000a). After the photometry the positions of the objects are calibrated for the geometric distortions of the WFPC2 camera (Holtzman et al. 1995b) applying the *distort* routine. At this step a conversion of the individual WF pixel coordinates to a common "global" coordinate system with reference to

the Planetary Camera is performed also - these common pixel coordinates have the orientation and scale of the PC frame.

3.1.5 Artificial star tests

Artificial-star experiments are a standard procedure to test the level of completeness of photometric data. The experiment consists of adding onto an image "artificial" stars generated from the scaled PSF obtained during the main photometry process and then repeating the photometry measurements for these simulated stars with the same settings to retrieve their magnitudes and positions (Mackey and Gilmore 2003; Piotto et al. 2002).

We added more than half a million artificial stars in each cluster to estimate the photometry completeness (*hstphot* option 64). The artificial stars are distributed following the light distribution in the original image. We simulated stars, which cover the parameter space on the CMD as the observed stars, namely in filters V and I with magnitudes from 13 mag to 27 mag and colour indicies (V-I) ranging from -0.5 mag to $+2.25$ mag. The number of simulated stars is approximately 40 000 stars per magnitude bin of one magnitude. This gives roughly 1000 stars per radial distance and magnitude bin, which is statistically significant amount of stars to estimate the completeness of a given radial-magnitude bin when constructing the RDPs of a cluster.

3.2 Data quality

On the output photometry list we apply a data quality selection. For each detected object *hstphot* provides position, χ of the PSF fit, signal-to-noise ratio, sharpness, roundness, major axis and object type, which is helpful to distinguish stellar from non-stellar objects. We keep only stellar objects with good photometry and reject objects which do not cover the quality criteria, namely: χ less than 2.5, positive signal-to-noise ratio, to be classified as a star (*hstphot* type $\leq$ 3), and sharpness between -0.3 and $+0.3$. Such values are recommended in the *HSTphot* manual for stellar photometry and used in Dolphin (2000a). In Figure 3.1 the χ of the fit is plotted vs. sharpness of the objects. The vast majority of the stellar objects are

concentrated within the applied limits for χ and sharpness. The sharpness is zero for a perfectly-fit star, positive for a star that is too sharp (e.g. cosmic ray), and negative for a star that is too broad (e.g. unresolved galaxy or cluster). By imposing a limit on the sharpness we reject such non-stellar objects from the final photometry list. The artificial stars photometry followed the same data quality cleaning process, with exactly the same criteria, as the real stars.

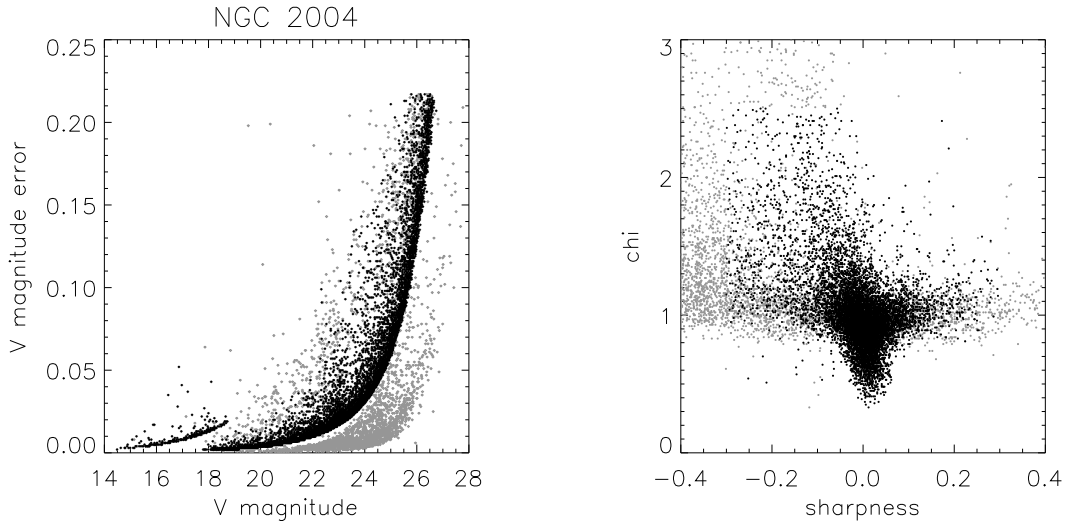

Figure 3.1: Left: The distribution of the estimated *hstphot* photometric errors as a function of magnitude for the cluster NGC 2004, in grey are the rejected objects that do not cover the data-quality criteria, Right: Goodness of fit χ vs. sharpness, a diagnostics for data quality. In black are the objects that do cover all the data quality criteria.

The typical photometric errors of our photometry are presented in Figure 3.1 Left panel with data from cluster NGC 2004 in filter V. In the full magnitude range the errors reach up to 0.22 magnitudes, but in the subsequent analyses the contribution of stars fainter than 25 mag in V is negligible. The positive effect of using images with short and long exposure times is evident in the figure, bright stars photometry is based on the short exposures, where they are not saturated.

In a comparison with ground based observations (Figure 3.2 Right) it is clear that both the magnitude limit and the photometric errors are lower for HST observations. The ground based observations of M 15 we used for this comparison are presented

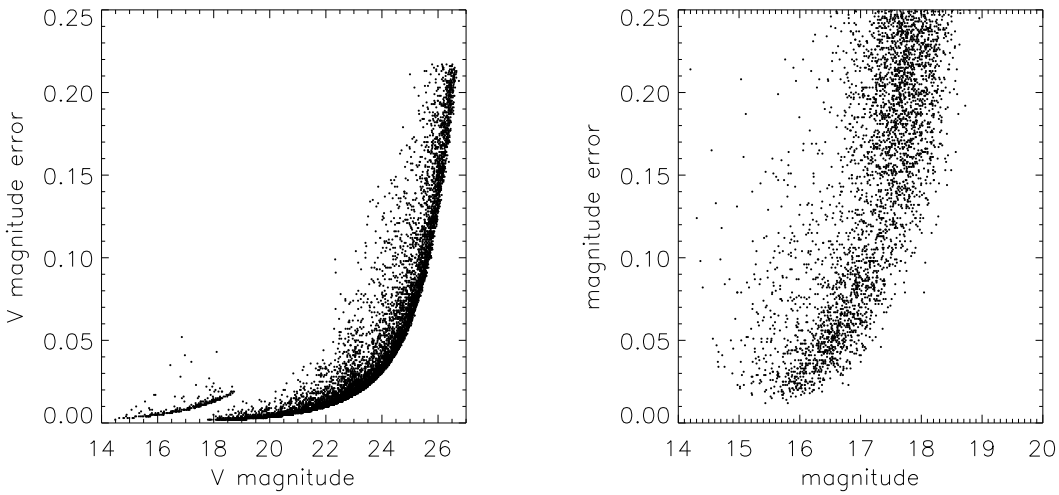

Figure 3.2: Left: The distribution of the estimated *hstphot* photometric errors as a function of magnitude for the cluster NGC 2004, Right: Distribution of photometric errors of cluster M 15 from ground based observations. The Y range on both images is the same for easier comparison.

in Nikolov (2018b) and are typical for the star cluster studies done in late 20-th century. Images were reduced following the standard PSF photometry in IRAF[1] *daophot* package. From this comparison it is evident, that after the data quality cleaning the spread of magnitudes obtained from HST observations is much lower, than the one obtained with ground based observations. This high signal-to-noise of the HST observations in wide magnitude range of more than 10 magnitudes, allows us to observe tight main sequences on the clusters' CMDs in Section 6 and to determine with confidence the ages of the stellar populations of the studied clusters.

[1]Image Reduction and Analysis Facility, `http://iraf.noao.edu/`

Chapter 4

Methods

In this chapter we describe the methods used for analyses in the following Chapters. From the obtained photometric measurements, how do we calculate the stellar density, construct the radial density profiles, derive structural parameters of the clusters via model fitting.

4.1 RDP construction

Radial density profiles (RDP) are used for decades to describe the stellar spatial distribution of the stars within star clusters. The method is based on counting the number of stars in concentric annuli around cluster centre, assuming spherical symmetry of the cluster. This approach was followed in our investigation. In the images selected for the present work the core of the investigated clusters is always centered onto the Planetary Camera. Due to the peculiar L-shape of the WFPC2, parts of the outer cluster regions were not covered by the WFCs. We have no reason to expect non-symmetrical distribution of stars in the area not covered by WFPC2 (see Elson (1991)). Following this presumption we have analyzed density profiles based on star counts in radial bins on the actually observed area of the camera only. To obtain the stellar density we divided the number of stars in every concentric ring by its area calculated in Section 4.1.1.

4.1.1 Areas calculation

Important step which needs clarification on constructing the RDP is the annuli effective area evaluation, namely to account for vignetted region strips typical for WFPC2 mosaic images and the L-shape of the camera. The measurement reduction is additionally complicated by the dithering applied during observations, which is typically between 5 and 11 pixels and is different for the different clusters.

The areas of the rings for the RDPs are computed individually for each cluster. This is necessary, since every cluster centre was imaged in different position on the camera and also because of the presence of vignetted regions between the four WFPC2 CCDs. To calculate the area of the rings we first determine the limits of the gaps between the WFPC2 cameras. This is done from the final photometry list of a cluster. Given that we use a common (global) coordinate system with the reference and pixel scale of the Planetary Camera, we compute the effective area of the observation by integrating the elementary areas (area of one PC pixel) over the positions of the detected stars. For each of the four chips we took the sum of the elementary areas from the minimum to the maximum of the positions in pixels of the detected stars over the chip. This method accounts for the size of the gaps between the chips individually for each cluster, which varies due to the dithering pattern of the observations. The validity of the described procedure is discussed in Section 3.1, since the HSTphot routine *distort* provides coordinate transformation and rescaling of WF cameras to the coordinate system of the PC, thus giving us all the actually observed WFPC2 area in one common PC-based global coordinate system. For better coverage of the field we use the combined catalog of all detected stars with a good photometry (that pass the data quality restrictions set in Section 3.2) omitting this way the border areas between the frames. The total effective area of the observations used for a cluster we estimate to 4.83 ± 0.02 square arcminutes. An example is presented in Figure 4.1 with stars of NGC 2031 in the global coordinates, with scale and orientation of the PC, limits of the cameras indicated by red lines.

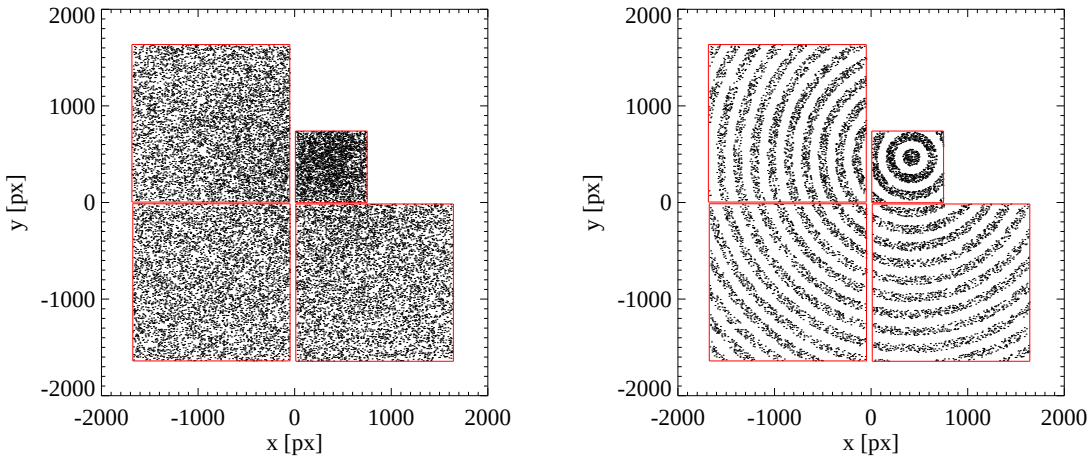

Figure 4.1: Left: The field-of-view of the WFPC2 with stars of NGC 2031 and limits of the gaps between cameras indicated with lines in red. Coordinates in (x,y) are pixel coordinates in global coordinate system. Right: Every other ring of stars from the cluster centre with radial step of 4 arcsec is plotted.

4.1.2 Incompleteness corrections

Even with the superb HST spatial resolution, the crowding and saturation can cause a number of stars to be missed by an automated detection software. This deficiency badly affects clusters's RDP and must be accounted for (Schechter et al. (1993)). Here we adopt the methodology followed by Mackey and Gilmore (2003). To quantify the completeness correction, we apply artificial star tests available in HSTphot during stellar photometry measurements, by generating approximately 5.7×10^5 artificial stars, covering parameter space on the CMD where the observed stars are located (see Section 3.1.5). Artificial stars are measured photometrically following the same steps and settings as real stars. Only if the measured artificial star coordinates coincide with that of the simulated one within 1 pixel and its brightness is within 1 magnitude tolerance, then the artificial star is considered recovered. Otherwise the artificial star is flagged as non-recovered. The completeness factor C_f is defined as the ratio of the number of successfully recovered (unflagged) stars ($N_{recovered}$) to the number of artificial stars ($N_{simulated}$) generated and varies between 0 and 1. The completeness correction C_c applied on the RDP is the inverse of the

completeness factor.

$$C_f = \frac{N_{recovered}}{N_{simulated}} = C_c^{-1} \tag{4.1}$$

4.1.3 Density calculation

Stellar density is calculated by dividing the number of stars detected in each bin by the actually observed annulus area as measured in the previous section, in square arcminutes. This way the stellar density radial profile ranging from the centre of the cluster out to 90 arcseconds is constructed. The centre of every cluster we study is adopted from the homogeneous study of (Mackey and Gilmore 2003) since in the majority of the clusters they use the same images as the presented in this Thesis. The distance from the cluster centre is calculated for every star in arcseconds as $d = \sqrt{(x - x_c)^2 + (y - y_c)^2}$, where x_c and y_c are the pixel coordinates of the cluster centre, and x,y are the star coordinates. The width of the radial step in RDP construction was set to 4 arcsec, which provided optimal profile resolution and enough stars in each ring. The corresponding uncertainty on the RDP is calculated from the square root of the number of stars in each radial annulus, divided by the actual area of the annulus. The stellar density in i-th ring is calculated as number of stars per its area, including the completeness correction C_c:

$$f(i) = \frac{N_{stars}(i)\ C_c(i)}{A(i)} \tag{4.2}$$

For every cluster we investigate three types of radial density profiles for different subgroups of stars. Each one is modeled with an EFF87 or King-like model to derive structural parameters in Sections 5 and 6 for the young and old clusters in the study, respectively.

A) We construct a single radial density profile based on all stars photometered in a cluster and fit it with a model to determine the structural parameters of the cluster as a whole system. These are suitable for a direct comparison with previous studies.

B) We construct and fit RDPs of two subgroups of stars, *bright* and *faint* – stars brighter or fainter than 20.0 magnitude in V filter. This limiting magnitude is in the middle of the magnitude range of our photometry. This approach can show the

general behaviour of the core-radius with magnitude.

C) We construct and fit a radial density profile of stars of every magnitude, with bin width of 1 magnitude (e.g. $19 \leq V < 20$, then $20 \leq V < 21$, etc.). Naturally, we need several stars to construct the RDP, at least 4 at different radial distances, so for the brightest stars in a cluster no RDP can be constructed. Using this approach we can sample the behaviour of the core-radii with magnitude. This allows us to use this radii in a comparative study within a cluster and as a tool to assess mass segregation of the subgroups.

4.2 Profile fitting

The observed RDPs were approximated using MPFIT (Markwardt 2009), a minimization package in IDL[1], developed with the perspective of astronomical data analysis. It does a hypothesis testing by least squares fitting for a certain model to represent the observational data by minimizing the difference between the model and the data.

The cluster's RDPs in Section 5.2 were fitted with King (1962) model, Equation 1.3 in its analytical form, with the background stellar density level f_b incorporated during fitting as:

$$f(r) = f_0 \left\{ \frac{1}{\sqrt{1 + (r/r_c)^2}} - \frac{1}{\sqrt{1 + (r_t/r_c)^2}} \right\}^2 + f_b \tag{4.3}$$

The young clusters presented in Section 5 were analyzed via EFF87 model as in Equation 1.4, with the background stellar density level f_b incorporated during fitting as:

$$f(r) = f_0 \left(1 + \frac{r^2}{a^2}\right)^{(-\gamma/2)} + f_b \tag{4.4}$$

where $f(r)$ is the stellar density, f_0 is the density in the center of the cluster, a is a scale factor, related to the core-radius of the cluster as $r_c = a\sqrt{2^{2/\gamma} - 1}$, parameter γ is the power factor and f_b is the background density level. We have incorporated

[1]Interactive Data Language,
`https://www.harrisgeospatial.com/Software-Technology/IDL`

the background density into the model we fit. We assume a constant background density, which is a reasonable assumption having the field-of-view of the camera. The small and irregular shape of WFPC2 does not allow us to have a independent determination of stellar background near the cluster, and for most of the clusters there are no additional images observed. Our experiments showed that the derived structural parameters when fitting the background or when subtracting it from the profile are practically the same.

4.3 Structural parameters and segregation diagnostics diagram

Cluster structural parameters are derived in Section 5.2 as parameters of King (1962) profile as presented in Equation 4.3 which provides the radius of the core r_c and tidal radius r_t, also the central and the background stellar densities f_0 and f_b. The profiles of the young Magellanic clouds clusters we investigate are fitted with an Elson et al. (1987) model, Equation 4.4, that provides the scale parameter a, which translates to the King model core-radius r_c, the slope γ of the profile and f_0 and f_b – the central and background densities. The core-radii derived per subgroups of stars within a cluster are then used to trace mass segregation on a diagnostics diagram (e.g. Figure 5.1), the derived core-radius r_c as a function of the mean magnitude of the stars in the subgroup (de Grijs et al. 2002b).

4.4 Isochrones fitting and synthetic clusters

Age estimations of the cluster population is done via fitting theoretical isochrones to the observed CMDs of the clusters studied in Section 6 and a comparison with synthetic cluster. For this purpose the Astronomical Observatory of Padova PARSEC isochrones[1] were used. The isochrones were computed using the stellar evolution models, as presented in Marigo et al. (2008) and Marigo et al. (2017). An initial estimate of the distance modulus towards the studied clusters of $(m - M) = 18.5$ is used. The isochrones are then fitted by eye selecting the one that best represents

[1]Isochrones available at `http://stev.oapd.inaf.it/cgi-bin/cmd`

the observed stellar population. The uncertainty can be estimated from the set of isochrones, the nearest younger and the nearest older than the best-fitting isochrone.

For comparison, also a synthetic cluster for the corresponding age is generated from the SYCLIST[1] tool from the Geneva stellar models, following the approach of Georgy et al. (2014). Results on age determination of clusters NGC 2004 and NGC 2031 are presented in Sections 6.3 and 6.2.

[1]Synthetic clusters available at `https://www.astro.unige.ch/syclist/`

Chapter 5

Dynamical evolution of the studied clusters

The Large Magellanic Cloud (LMC) and the Small Magellanic Cloud (SMC) provide the unique opportunity to study populous star clusters, which cover wider age range than those observed in the Milky Way, where the most populated clusters are the globular clusters with ages comparable to the age of the Universe. The mechanisms of formation of the MC clusters and their dynamical evolution are still under intensive exploration. The dynamical models predict that after the cluster is formed the less massive stars are given additional kinetic energy from the massive stars via two-body encounters (Lightman and Shapiro 1978; Meylan and Heggie 1997; Spitzer 1987). Eventually some of them overcome the cluster's gravitational potential and escape. The massive stars, on the other hand, in time tend to sink towards the cluster's centre, and the most massive stars form the core of the cluster. This is the expected outcome of the dynamical evolution of a star cluster past the relaxation time, the cluster age at which a Maxwellian distribution of the velocities is achieved. This process leads to the stellar segregation (or stratification) in star clusters. Observationally, the spatial distribution of massive stars shows a central concentration with a core-radius being smaller than that of the less massive stars.

An alternative explanation of the stellar segregation observed in clusters is that it has a primordial origin (Bonnell and Davies 1998), i.e. the massive stars are born inside the cluster's core at an early cluster formation epoch. In this case the massive

stars central concentration is displayed before relaxation time. For this reason the estimation of the cluster age, relaxation and segregation is of great importance for more reliable understanding of star cluster formation and dynamical evolution.

We have selected a sample of LMC star clusters, presented in Table 5.1, to investigate them by means of their radial number density profiles. This approach allows us to determine the radial distribution of the stars of various magnitudes. Since the brighter stars are more massive than the fainter stars, these profiles can be used to trace mass segregation in star clusters. In the following sections we have fitted the observed RDPs with theoretical models by Elson, Fall & Freeman (Elson et al. 1987) and King (1962) to determine the core-radius and the concentration of the stars per magnitude range for the investigated clusters. In Table 5.1 the cluster coordinates and core-radii are from Mackey and Gilmore (2003), and the age reference is indicated in the table.

Table 5.1: Coordinates, core-radii and ages of the studied clusters.

Cluster name	RA [hms]	DEC [dms]	r_c [arcsec]	Age [Gyr]	Age Ref.[a]
NGC 1711	4:50:37.3	-69:59:04	8.78	0.08	(1)
NGC 1754	4:54:18.9	-70:26:31	3.61	13.5	(4)
NGC 1898	5:16:42.4	-69:39:25	8.40	13.5	(5)
NGC 1984	5:27:40.8	-69:08:05	4.07	0.01	(1)
NGC 2004	5:30:40.9	-67:17:09	6.47	0.02	(2)
NGC 2005	5:30:10.3	-69:45:09	3.63	13.5	(4)
NGC 2011	5:32:19.6	-67:31:14	4.81	0.01	(1)
NGC 2019	5:31:56.6	-70:09:33	3.61	13.5	(4)
NGC 2031	5:33:41.1	-70:59:13	10.81	0.13	(3)
NGC 2214	6:12:55.8	-68:15:38	8.79	0.04	(1)

[a] Age references: (1) Wolf et al. (2007), (2) Niederhofer et al. (2015), (3) Dirsch et al. (2000), (4) McLaughlin and van der Marel (2005), (5) Olsen et al. (1998)

5.1 Indication of mass segregation in the young LMC star clusters NGC 1711, NGC 1984, NGC 2004, NGC 2011, NGC 2031, and NGC 2214

Here we present a study on mass segregation in six populous star clusters located in the Large Magellanic Cloud. The selection criteria of targets are the following:

- clusters that have available HST archive observations at different exposure times, since the most bright stars (and therefore more massive) are saturated at long exposures;
- clusters that are candidates for mass segregation from previous studies;
- clusters of various ages in order to examine the distribution of stars at different dynamical evolution stages. Details on the selected target clusters are presented in Table 5.1.

We use archival observations from the Hubble Space Telescope WFPC2 camera, as listed in Table 2.1 and 2.2. The selected target clusters have been observed in two broad-band filters, F555W and F814W, which correspond to Johnson's V and I. The calibrated images we use were reduced at the STScI archive according to the standard HST pipeline (see Section 2.2). The photometric reduction are done using HSTphot (Dolphin 2000b). The individual images with the same pointing and rotation were combined in order to obtain a better signal-to-noise ratio, then used for PSF photometry. Details are presented in Section 3.1. The magnitude errors from the photometry are typically larger than 0.1^m only for the stars fainter than $V > 25^m$.

5.1.1 Profiles construction and fitting

We construct the profiles by counting the number of stars in concentric rings from the center of the cluster. The number of stars in each ring is corrected for the incompleteness of the photometry and then divided by the area of the ring to determine the stellar density. Three types of profiles are considered: from all stars in the

cluster; *bright* and *faint* stars; per magnitude bin of one magnitude. In more detail the procedure of RDP construction is described in Section 4.1.

To the constructed profiles of young LMC clusters we fit an Elson et al. (1987) model of the form of Equation 4.4. We use the MPFITEXPR routine from MPFIT package (Markwardt 2009) to find the best-fitting model to the profiles. During the profiles fitting we restrict the scale-radius a, the central f_0 and background density f_b to be positive in order to speed-up the fitting process. In the majority of the investigated clusters profiles the fit converges between 10 and 30 iterations.

Table 5.2: The cluster structural parameters derived from the EFF87 profile fitting.

magnitude range	f_0 $stars/arcmin^2$	f_b $stars/arcmin^2$	a arcsec	r_c arcsec
NGC 1711				
all	16670 ± 375	807.87 ± 9.37	20.10 ± 0.76	13.00 ± 0.22
bright	5396 ± 139	51.63 ± 12.62	12.96 ± 0.96	10.01 ± 0.31
faint	11530 ± 298	754.79 ± 8.09	23.94 ± 1.06	14.15 ± 0.25
15 – 16	95 ± 5141	0.00 ± 1.59	5.68 ± 7.91	8.61 ± 3.66
16 – 17	724 ± 132	5.87 ± 0.77	10.37 ± 1.31	7.09 ± 0.54
17 – 18	574 ± 111	6.94 ± 0.42	26.82 ± 4.45	12.38 ± 0.98
18 – 19	1323 ± 58	18.21 ± 5.23	22.75 ± 3.36	12.21 ± 0.63
19 – 20	2370 ± 216	22.50 ± 8.39	12.22 ± 1.32	10.27 ± 0.61
20 – 21	2569 ± 17	82.49 ± 2.43	39.61 ± 1.28	15.27 ± 0.10
21 – 22	2944 ± 509	134.67 ± 26.97	22.84 ± 3.63	13.29 ± 1.24
22 – 23	3354 ± 204	179.54 ± 11.44	14.28 ± 1.14	11.88 ± 0.51
23 – 24	2709 ± 108	330.83 ± 4.93	33.44 ± 2.96	16.28 ± 0.39
NGC 1984				
all	13012 ± 559	2209.04 ± 13.34	6.02 ± 0.31	5.74 ± 0.18
bright	3137 ± 208	130.46 ± 2.30	12.81 ± 1.39	7.19 ± 0.30
faint	10422 ± 189	2048.07 ± 13.64	4.44 ± 0.22	4.96 ± 0.13
16 – 17	663 ± 92	3.12 ± 0.89	4.00 ± 1.47	3.92 ± 0.85
17 – 18	405 ± 131	6.94 ± 2.41	10.68 ± 2.63	7.62 ± 1.05

Table 5.2: continued.

magnitude	f_0	f_b	a	r_c
18 – 19	683 ± 3625	27.09 ± 7.93	19.13 ± 5.46	7.38 ± 1.90
19 – 20	855 ± 129	77.59 ± 2.01	15.79 ± 3.45	8.91 ± 0.71
20 – 21	1602 ± 148	120.15 ± 2.98	6.45 ± 0.63	6.01 ± 0.37
21 – 22	1796 ± 702	353.96 ± 5.35	10.80 ± 1.80	7.85 ± 0.92
22 – 23	3060 ± 2416	662.14 ± 8.22	2.54 ± 0.89	3.28 ± 1.07
23 – 24	7803 ± 3495	880.49 ± 25.50	1.35 ± 6.35	2.00 ± 2.27
NGC 2004				
all	11145 ± 790	703.21 ± 21.61	14.06 ± 1.07	11.66 ± 0.55
bright	5222 ± 1523	24.80 ± 8.31	7.00 ± 0.90	7.10 ± 0.78
faint	6552 ± 550	688.93 ± 18.20	20.07 ± 2.02	14.17 ± 0.76
15 – 16	128 ± 21	3.70 ± 0.59	28.36 ± 10.75	15.49 ± 2.18
16 – 17	567 ± 56	5.75 ± 1.49	5.27 ± 1.14	4.71 ± 0.57
17 – 18	502 ± 39	6.60 ± 0.59	21.88 ± 4.28	11.45 ± 0.80
18 – 19	1249 ± 227	5.21 ± 2.24	8.86 ± 1.02	8.05 ± 0.69
19 – 20	2638 ± 1628	6.73 ± 4.58	4.90 ± 0.97	5.70 ± 1.10
20 – 21	3556 ± 697	0.00 ± 17.17	3.05 ± 3.89	4.37 ± 2.42
21 – 22	1507 ± 56	133.62 ± 2.46	28.07 ± 3.41	14.25 ± 0.40
22 – 23	7548 ± 1450	114.38 ± 41.24	4.29 ± 1.61	5.17 ± 1.89
23 – 24	1950 ± 38	309.22 ± 8.34	14.45 ± 1.04	11.81 ± 0.23
NGC 2011				
all	5170 ± 327	1014.96 ± 13.28	16.89 ± 1.76	11.86 ± 0.52
bright	1063 ± 81	29.03 ± 4.46	9.29 ± 1.89	9.37 ± 0.90
faint	4083 ± 405	983.23 ± 11.70	19.72 ± 2.95	12.35 ± 0.73
15 – 16	82190 ± 89312	3.57 ± 2.28	0.06 ± 22.10	0.07 ± 8.39
16 – 17	77 ± 5	3.83 ± 0.55	8.67 ± 6.48	7.89 ± 1.76
17 – 18	83 ± 6	6.01 ± 0.30	38.91 ± 1.59	15.00 ± 0.61
18 – 19	235 ± 14	7.80 ± 0.49	15.80 ± 2.38	9.89 ± 0.76
19 – 20	516 ± 90	9.00 ± 5.02	3.90 ± 4.86	6.80 ± 3.69
20 – 21	789 ± 45	44.36 ± 1.71	13.41 ± 1.16	10.64 ± 0.49
21 – 22	972 ± 255	59.54 ± 27.08	6.56 ± 1.59	9.31 ± 1.81

Table 5.2: continued.

magnitude	f_0	f_b	a	r_c
22 – 23	609 ± 102	210.59 ± 2.33	40.46 ± 6.74	15.60 ± 1.33
23 – 24	875 ± 936	279.80 ± 4.24	27.89 ± 5.87	10.75 ± 2.23
24 – 25	855 ± 82	334.16 ± 2.04	37.30 ± 2.89	14.38 ± 0.67
NGC 2031				
all	13146 ± 222	2218.02 ± 44.22	18.49 ± 0.86	16.17 ± 0.30
bright	3249 ± 63	31.75 ± 8.96	9.34 ± 0.47	10.29 ± 0.24
faint	10184 ± 182	2215.38 ± 39.88	22.02 ± 1.25	17.54 ± 0.34
16 – 17	243 ± 17	3.78 ± 0.87	7.06 ± 1.04	6.79 ± 0.56
17 – 18	918 ± 37	1.92 ± 1.12	5.07 ± 0.49	5.34 ± 0.35
18 – 19	894 ± 39	12.79 ± 3.14	15.83 ± 1.35	11.92 ± 0.39
19 – 20	1344 ± 40	0.00 ± 2.03	9.99 ± 0.41	12.86 ± 0.40
20 – 21	1945 ± 35	70.90 ± 7.91	15.02 ± 0.81	14.02 ± 0.27
21 – 22	2403 ± 75	147.88 ± 17.86	9.38 ± 1.05	11.51 ± 0.58
22 – 23	1934 ± 98	311.37 ± 32.76	16.40 ± 2.57	18.60 ± 0.85
23 – 24	2329 ± 119	642.11 ± 13.61	23.48 ± 1.99	17.84 ± 0.69
24 – 25	2061 ± 66	949.21 ± 7.29	50.01 ± 5.43	20.58 ± 0.58
NGC 2214				
all	11318 ± 170	397.99 ± 14.27	14.50 ± 0.50	12.45 ± 0.19
bright	2691 ± 55	21.81 ± 2.45	13.06 ± 0.71	10.68 ± 0.28
faint	8635 ± 183	380.13 ± 15.34	15.17 ± 0.67	12.99 ± 0.25
16 – 17	235 ± 34	5.12 ± 1.98	6.72 ± 3.60	5.63 ± 1.21
17 – 18	204 ± 125	7.28 ± 0.82	38.25 ± 7.39	14.75 ± 2.18
18 – 19	792 ± 51	17.61 ± 3.81	19.55 ± 3.13	11.55 ± 0.75
19 – 20	1229 ± 77	0.00 ± 0.20	13.16 ± 0.83	11.45 ± 0.50
20 – 21	1980 ± 69	0.00 ± 2.10	10.18 ± 0.46	10.15 ± 0.32
21 – 22	1268 ± 22	63.82 ± 3.34	25.30 ± 1.63	15.18 ± 0.20
22 – 23	1630 ± 60	78.71 ± 3.04	19.90 ± 1.51	14.35 ± 0.41
23 – 24	1568 ± 152	118.18 ± 7.54	20.36 ± 3.08	14.79 ± 0.99
24 – 25	2394 ± 35	93.26 ± 8.43	8.54 ± 0.38	10.40 ± 0.20

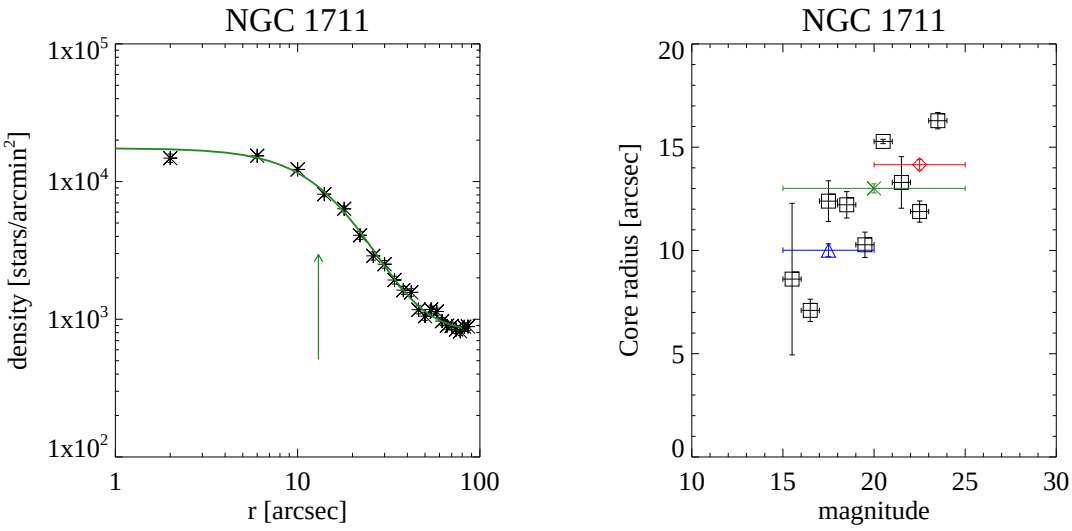

Figure 5.1: Left: Radial density profile for NGC 1711: the distance from the cluster center (in arcsec) vs. stellar density (star count per square arcminute). The best-fit Elson et al. (1987) model is plotted with a solid curve. The cluster core-radius is indicated by an arrow. Right: Segregation diagnostics diagram - core-radius as a function of the magnitude of the stars.

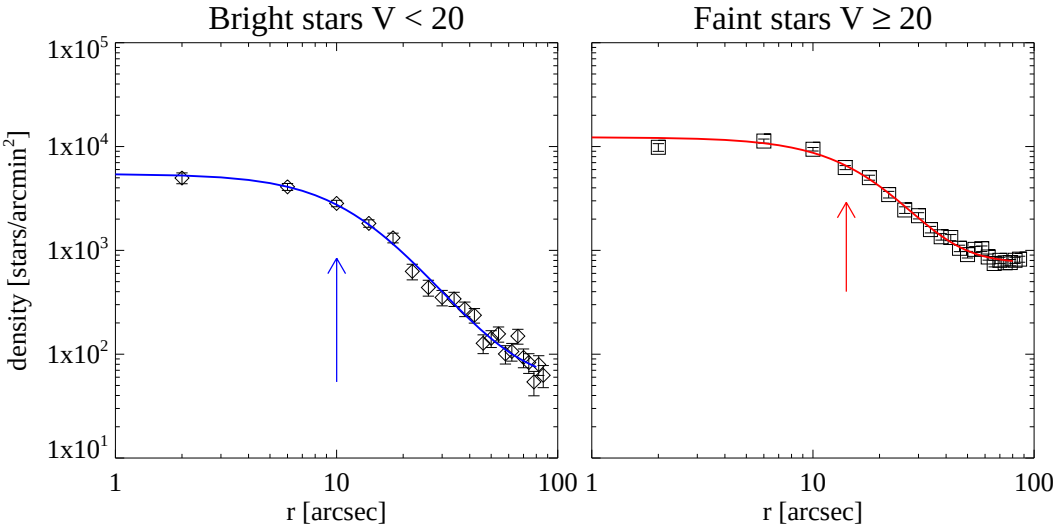

Figure 5.2: Radial density profile for stars brighter (Left panel) and fainter (Right panel) than 20^m for NGC 1711. The best-fit Elson et al. (1987) model is shown with a solid curve. The cluster core-radius is indicated by an arrow.

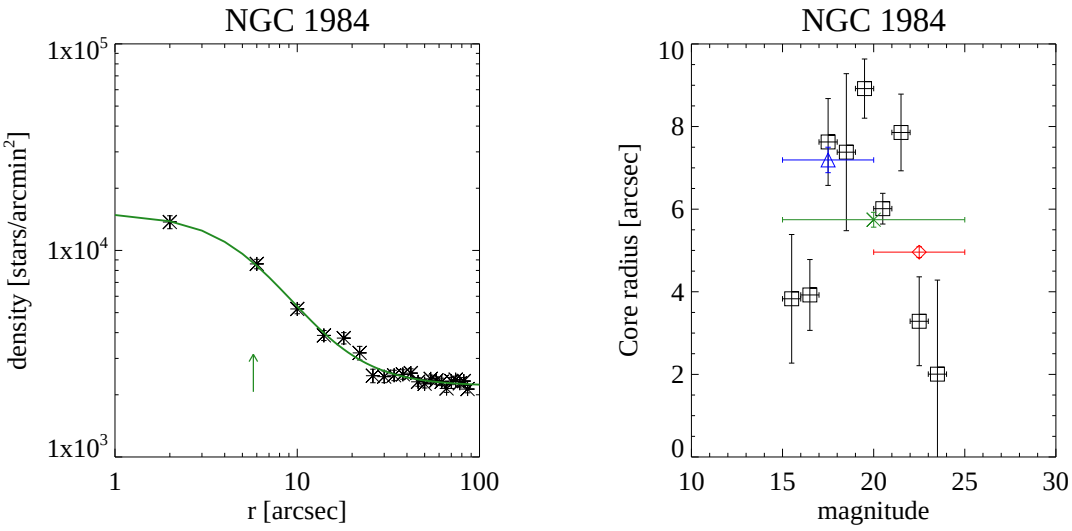

Figure 5.3: Same as 5.1 for NGC 1984.

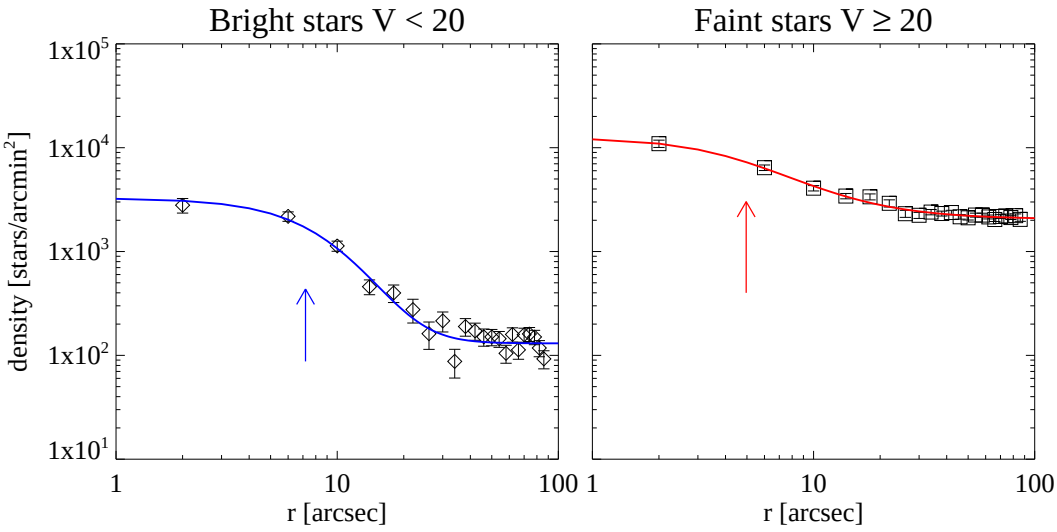

Figure 5.4: Same as 5.2 for NGC 1984.

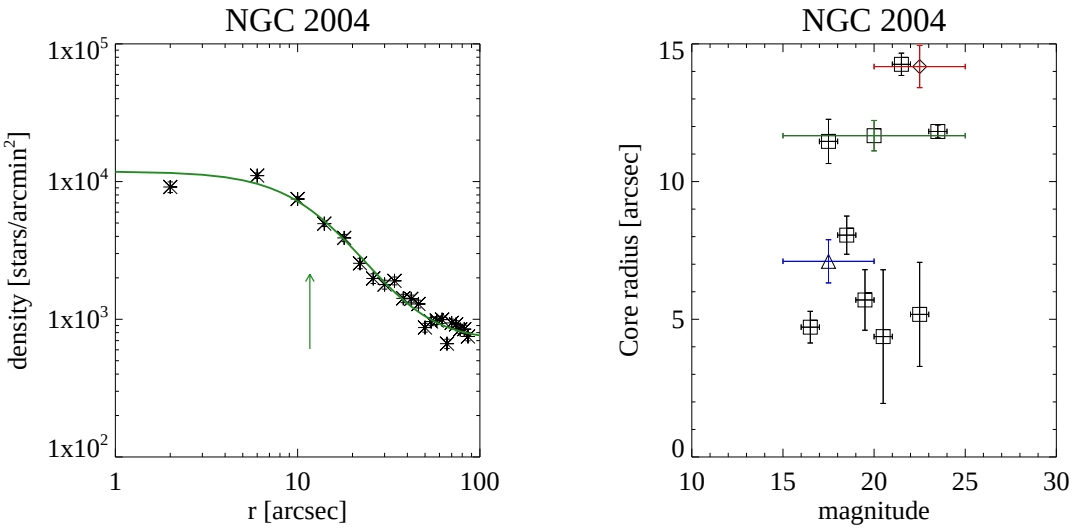

Figure 5.5: Same as 5.1 for NGC 2004.

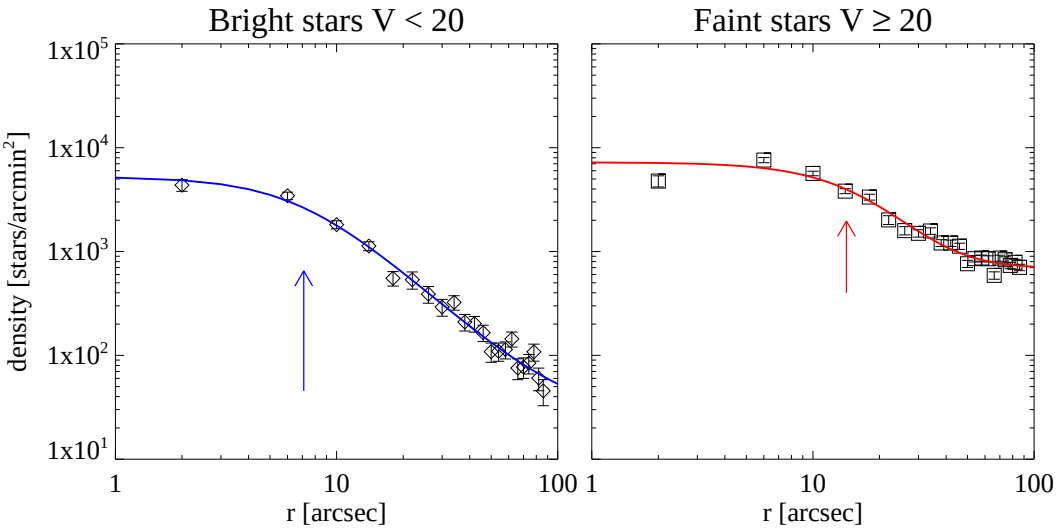

Figure 5.6: Same as 5.2 for NGC 2004.

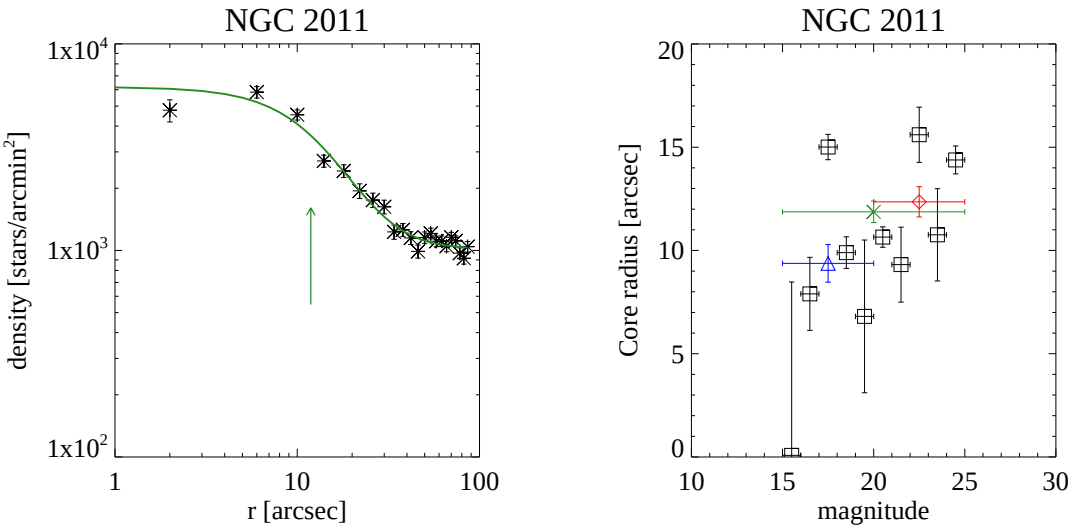

Figure 5.7: Same as 5.1 for NGC 2011.

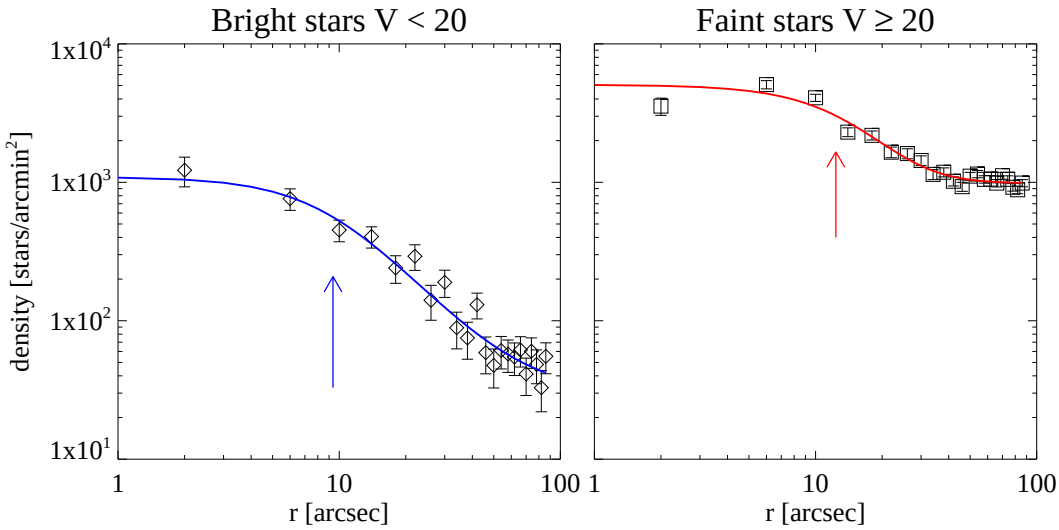

Figure 5.8: Same as 5.2 for NGC 2011.

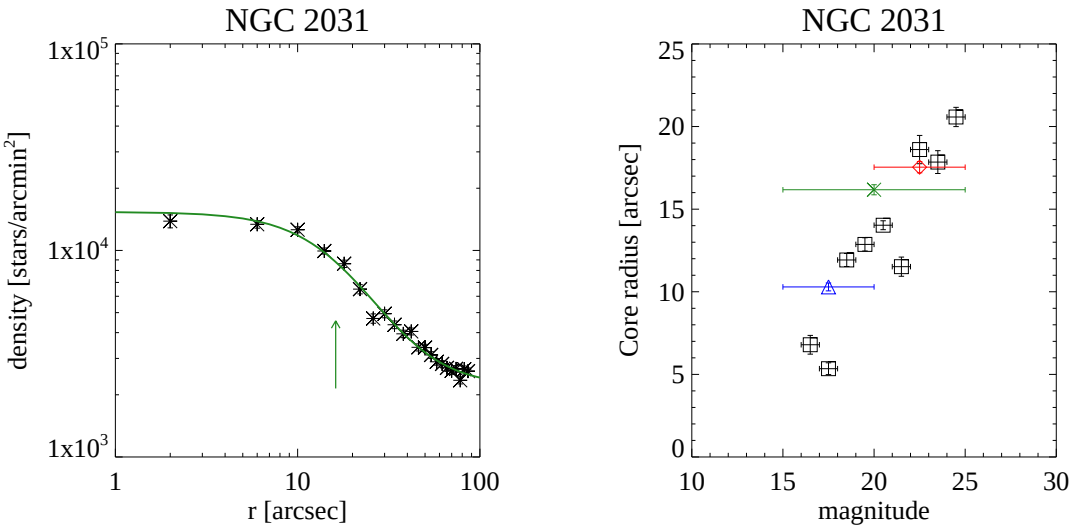

Figure 5.9: Same as 5.1 for NGC 2031.

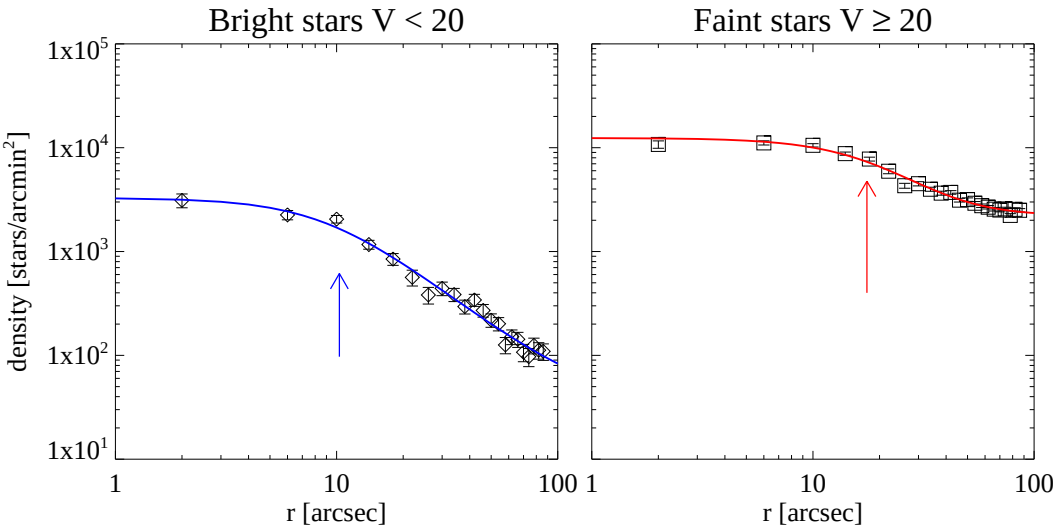

Figure 5.10: Same as 5.2 for NGC 2031.

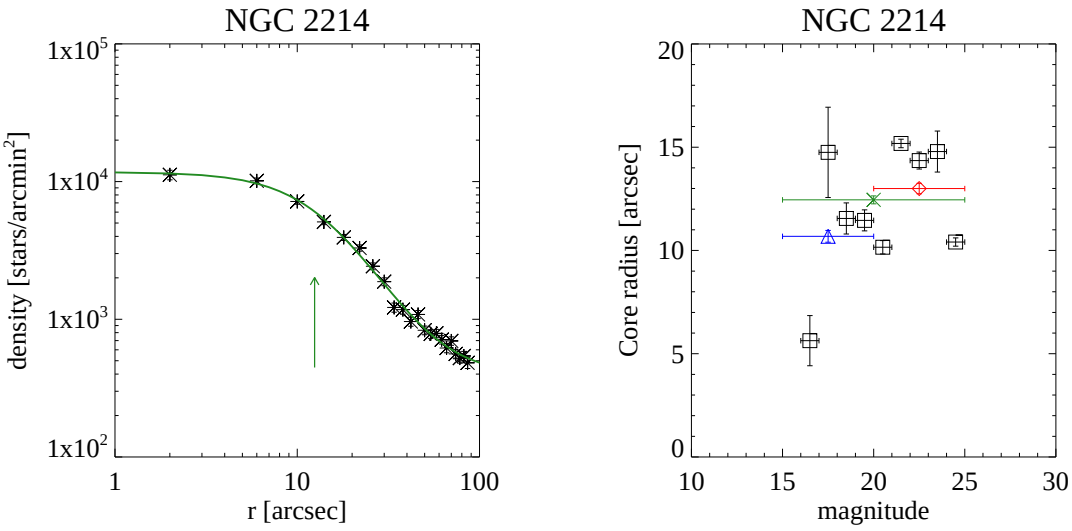

Figure 5.11: Same as 5.1 for NGC 2214.

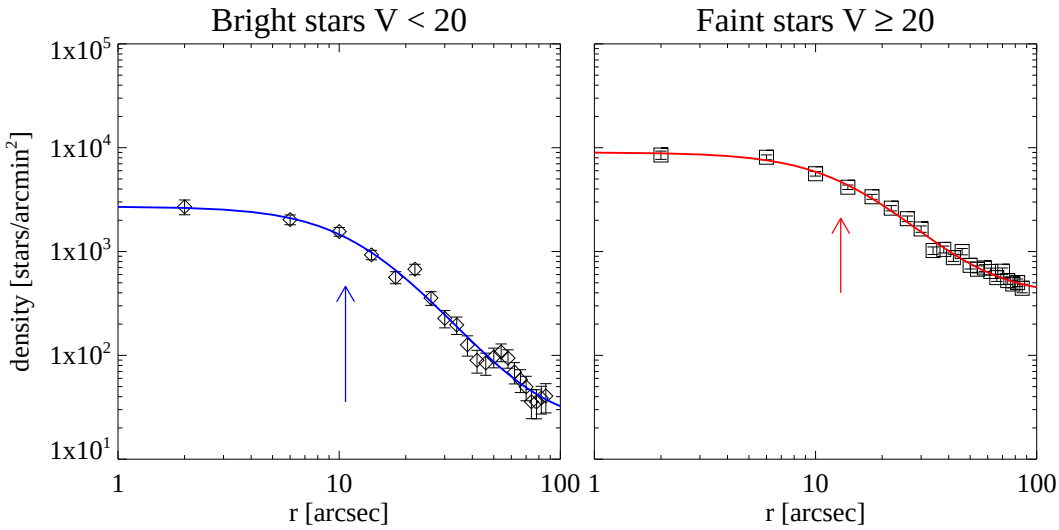

Figure 5.12: Same as 5.2 for NGC 2214.

5.1.2 Stellar segregation discussion

Figures 5.1 – 5.11 show the derived core-radius for each magnitude bin of stars vs. the mean value of the magnitude bin with black squares. The values for *bright* stars ($V < 20$) and *faint* stars ($V \geq 20$) are indicated with blue triangles and red diamonds respectively. In green with asterisks is marked the core-radius derived for all magnitudes of stars in the indicated cluster.

The dependencies of the core-radius with magnitude in a cluster, as presented in Table 5.2 and in Figures 5.1 – 5.11 are used as a diagnostics of mass segregation, namely: if there is a trend of increasing core-radius with fainter magnitudes we argue that there is an indication of mass segregation. Among the targets investigated in this study is NGC 1711, a cluster already suspected in mass segregation by Subramaniam et al. (1993). In the diagrams presented here in Figure 5.1 Right for NGC 1711, there is clearly evidence of increasing of the derived core-radius with magnitude. The value of the radius of the core for *bright* stars of 10.01 arcsec determined in our study agrees well with the result based on photographic plates $r_c = 2.2$ pc (9.05 arcsec) obtained by Kontizas et al. (1987). This confirmation of mass segregation in NGC 1711 is also a validation for the method we use.

NGC 1984 is located in a populous LMC region with an ongoing star formation. The relatively high number of field stars fainter than 20^m probably significantly influence the observed RDPs (Figure 5.3) of the *faint* stars and especially in the range V $\geq$ 22.

NGC 2004 is a very young cluster with some very bright O and B stars in its core. Some of these bright stars are saturated in our images. This limits the constructed profiles to V $<$ 24, as fainter stars suffer from incompleteness in the central region. Richtler et al. (1997) report evidence of mass segregation in NGC 2004 from mass function slope, and they also find stars of 1.1 solar masses, or of magnitude 22–23 in V to be outliers. Our results show, that NGC 2004 is mass segregated. Although the uncertainties of the core-radii determined per magnitude are of the order of an arcsec, the diagnostics diagram in Figure 5.5 presents a segregation in the cluster, and the values we determine for *bright* and *faint* stars strongly confirm it.

NGC 2011 is a young LMC cluster located in the OB association region LH 75. This cluster also shows an indication of stellar stratification (Figure 5.7 Right). The

large uncertainty of the core-radius of the brightest stars of magnitude 15–16 in V can be explained by the low number of stars of this magnitude.

NGC 2031 is a cluster with an age of 227 Myr. It is well resolved on the images we use and our photometry, also the profiles presented in Figures 5.9 and 5.10 do not suffer from much incompleteness. The derived from fitting core-radius in Figure 5.9 shows a pronounced increasing trend with magnitude, implying a clear segregation of the stars. Most massive stars are indeed found within the core of the cluster, while the faint less massive stars are more wide spread to the outer region of the cluster.

NGC 2214 is a young LMC cluster, possibly in a process of merging (Bhatia and MacGillivray 1988). In our photometry we cover a magnitude range of more than 10^m with a limiting magnitude fainter than 25 in V. Figure 5.11 shows the radial density profile of the cluster and the best EFF87 model fit is shown with green line. Figure 5.12 shows the representative density profiles for stars brighter than 20^m. The best-fitting model is presented with a blue line (Figure 5.12 left panel). The RDP of stars fainter than 20^m best-fit model is shown with red line in the right panel. The reason why we separate the stars in two groups brighter and fainter than 20^m, is because in this way we get much better statistics for the stellar density than in magnitude bins of 1^m. On Figure 5.11 we show the derived core-radius from fitting the profile for each magnitude bin. It is evident that the derived core-radius values as a function of stellar brightness tend to become larger with increasing magnitude, indicating mass segregation in the cluster.

From the above investigation we can confirm that the core-radius at various magnitudes may serve as a truthful indicator for mass segregation in star clusters.

5.2 Distribution of the stars in the old LMC clusters NGC 1754, NGC 1898, NGC 2005, and NGC 2019

Here we present our investigation of a sample of Large Magellanic Cloud star clusters. This galaxy is among the closest neighbours of the Milky Way. From our sample we selected four clusters with similar ages older than 10 Gyr, namely NGC 1754, NGC 1898, NGC 2005 and NGC 2019. We constructed the radial profiles of the clusters and derived their structural parameters to investigate again the variation of the core-radius with stellar brightness. Indication of stellar segregation is found in NGC 1754, NGC 1898 and NGC 2005.

5.2.1 Studied clusters

The clusters studied in this section are old, metal-poor and populous, similar to the Milky way globular clusters (Olsen et al. 1998). NGC 1898, NGC 2005 and NGC 2019 are located in the inner parts of of the Large Magellanic Cloud near the LMC bar, thus the field contribution from the host galaxy is rather significant. For this reason we incorporate the background/foreground stellar density during fitting. NGC 1754 is located in the outskirts of LMC and is less affected by field stars contamination. All four clusters are listed by Mackey and Gilmore (2003) as possibly post core-collapse evolved based on their surface brightness profiles and age. Literature values are listed in Table 5.3. The V magnitudes and $B-V$ colours are from Bica et al. (1996, 1999). Metallicity $[Fe/H]$ is from Olsen et al. (1998). Half-light r_h and tidal-radius r_t and cluster age is from the catalogue of McLaughlin and van der Marel (2005).

5.2.2 Photometry

In this study we use archival data from the WFPC2 on-board the Hubble Space Telescope. The images were taken for HST proposal ID 5916. List of observations of NGC 1754, NGC 1898 NGC 2005 and NGC 2019 is presented in Table 2.2 for the corresponding cluster.

Table 5.3: Literature data for the studied clusters.

Cluster Name	V mag	B-V mag	logage	[Fe/H]	r_h arcsec	r_t arcsec
NGC 1754	11.57	0.75	10.1	-1.42	11.2	142.9
NGC 1898	11.86	0.76	10.1	-1.37	9.15	184.7
NGC 2005	11.58	0.73	10.1	-1.92	8.65	98.8
NGC 2019	10.86	0.76	10.1	-1.23	9.72	121.6

We obtained calibrated files from the archive which were processed prior downloading by the standard STScI pipeline and calibrated using the latest WFPC2 calibrations. The photometry was performed simultaneously on the calibrated images with HSTphot package (Dolphin 2000b). During photometry extensive completeness tests were performed, as described in detail in Section 3.1.

5.2.3 Structural parameters

We construct the Radial Density Profiles (RDPs) by counting stars in concentric rings around the cluster centre. This number is corrected for the incompleteness of the stars and divided by the area of the ring. The resulting density profiles of the clusters are fitted with a King profile (King 1962) in the form presented in Equation 4.3. We construct the RDPs for several magnitude ranges, as described in Section 4.1, fit those profiles with the King model, and derive the core-radii of every subsample of the cluster. Thus we can study the variation of the core-radius with magnitude – a method commonly used to search for mass segregation in star clusters (Brandl et al. 1996; de Grijs et al. 2002a).

Table 5.4: Structural parameters derived from King-like model fitting, f_{0K} is the central density, f_b - background density, r_c is the core radius and r_t - tidal radius.

Magn. range	f_{0K} (arcmin^{-2})	f_b (arcmin^{-2})	r_c (arcsec)	r_t (arcsec)
NGC 1754				
all	42875 ± 5980	748.93 ± 193.18	11.73 ± 2.06	98.47 ± 39.77
bright	4670 ± 876	33.60 ± 12.93	5.58 ± 1.10	124.48 ± 105.19
faint	38850 ± 5825	723.24 ± 179.99	12.62 ± 2.39	93.69 ± 35.76
16 – 17	134 ± 410	5.43 ± 2.44	4.39 ± 9.18	150.00 ± 0.00
17 – 18	359 ± 152	4.35 ± 1.33	4.84 ± 2.21	62.92 ± 72.78
18 – 19	999 ± 304	7.23 ± 1.98	5.65 ± 1.85	75.50 ± 47.31
19 – 20	3340 ± 669	21.83 ± 10.88	5.50 ± 1.16	140.25 ± 148.75
20 – 21	1794 ± 336	35.14 ± 4.68	7.88 ± 1.24	150.00 ± 0.00
21 – 22	3070 ± 463	99.58 ± 14.34	6.93 ± 1.25	123.26 ± 105.00
22 – 23	16159 ± 1514	225.87 ± 35.80	7.83 ± 0.85	108.63 ± 38.20
23 – 24	47274 ± 5924	280.28 ± 30.23	7.03 ± 0.64	150.00 ± 0.00
NGC 1898				
all	21166 ± 2100	2324.53 ± 59.17	13.26 ± 1.62	73.01 ± 13.58
bright	2455 ± 316	227.64 ± 9.96	9.81 ± 1.23	150.00 ± 0.00
faint	18996 ± 2024	2084.26 ± 52.83	13.75 ± 1.81	68.72 ± 11.59
17 – 18	203 ± 78	14.67 ± 2.21	9.52 ± 3.46	150.00 ± 0.00
18 – 19	312 ± 133	44.72 ± 5.08	10.34 ± 4.46	150.00 ± 0.00
19 – 20	1982 ± 292	157.71 ± 7.32	8.44 ± 1.14	150.00 ± 0.00
20 – 21	1863 ± 286	237.91 ± 8.21	11.80 ± 2.34	55.70 ± 10.37
21 – 22	2333 ± 669	625.90 ± 49.62	12.96 ± 3.70	126.68 ± 174.65
22 – 23	14786 ± 1534	1196.02 ± 37.43	13.98 ± 1.85	65.98 ± 9.42
NGC 2005				
all	29686 ± 5203	2103.62 ± 149.46	15.08 ± 3.34	56.03 ± 7.88
bright	7188 ± 1031	199.93 ± 12.02	6.91 ± 1.10	60.14 ± 14.25
faint	22129 ± 6493	1881.00 ± 185.58	19.68 ± 6.34	56.82 ± 8.75

Table 5.4: continued.

Magn. range	f_{0K} (arcmin^{-2})	f_b (arcmin^{-2})	r_c (arcsec)	r_t (arcsec)
16 – 17	182 ± 117	4.96 ± 3.29	5.98 ± 4.39	101.29 ± 389.77
17 – 18	539 ± 285	10.59 ± 2.29	4.33 ± 1.68	150.00 ± 0.00
18 – 19	2142 ± 606	34.20 ± 8.37	5.12 ± 1.43	95.97 ± 107.89
19 – 20	4294 ± 607	139.92 ± 10.96	8.31 ± 1.40	48.85 ± 6.50
20 – 21	3518 ± 525	224.17 ± 12.83	8.54 ± 1.57	47.51 ± 7.47
21 – 22	4479 ± 815	600.96 ± 26.83	16.63 ± 3.77	54.50 ± 6.89
22 – 23	40636 ± 5231	1113.42 ± 28.61	6.28 ± 0.81	68.61 ± 9.99
NGC 2019				
all	47962 ± 2907	2295.29 ± 59.44	11.03 ± 0.90	62.97 ± 5.56
bright	5240 ± 519	227.00 ± 11.81	11.15 ± 1.48	74.30 ± 14.82
faint	42725 ± 2630	2061.03 ± 54.16	11.00 ± 0.91	61.75 ± 5.32
16 – 17	209 ± 64	5.78 ± 1.35	15.47 ± 6.66	57.35 ± 15.27
17 – 18	543 ± 250	8.92 ± 4.40	6.77 ± 3.44	98.99 ± 151.48
18 – 19	1614 ± 293	44.33 ± 7.29	7.59 ± 1.67	100.70 ± 70.72
19 – 20	3129 ± 420	155.61 ± 9.30	13.39 ± 2.40	65.61 ± 11.57
20 – 21	3374 ± 626	290.62 ± 14.38	10.48 ± 2.45	62.48 ± 19.31
21 – 22	7735 ± 891	630.69 ± 21.12	11.05 ± 1.64	60.17 ± 10.16
22 – 23	31709 ± 1798	1128.92 ± 34.90	11.19 ± 0.88	60.67 ± 4.23

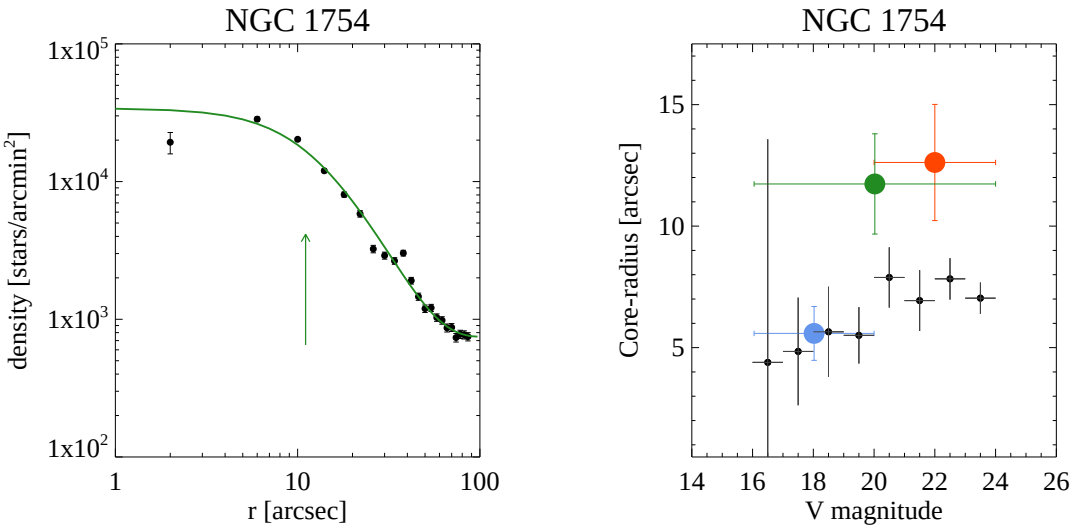

Figure 5.13: Left: RDP for cluster NGC 1754. King-like model fit is illustrated with green line, its r_c is indicated by an arrow. Right: stellar segregation diagnostics diagram for cluster NGC 1754. Core-radius from model fitting is on the y-axis, magnitude of the stars in the magnitude bin is on the x-axis.

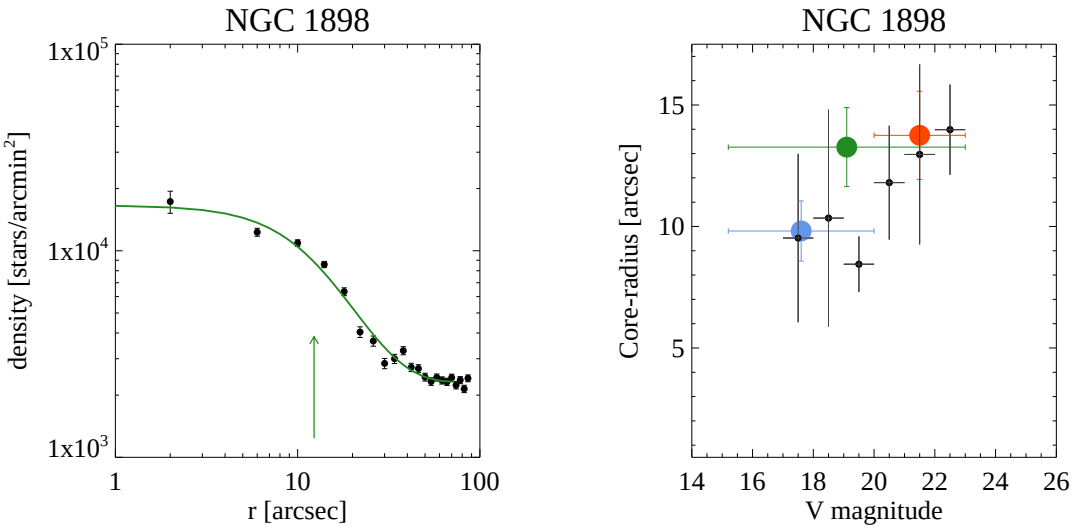

Figure 5.14: Left: RDP for cluster NGC 1898. Right: Same as Fig. 5.13 Right for cluster NGC 1898.

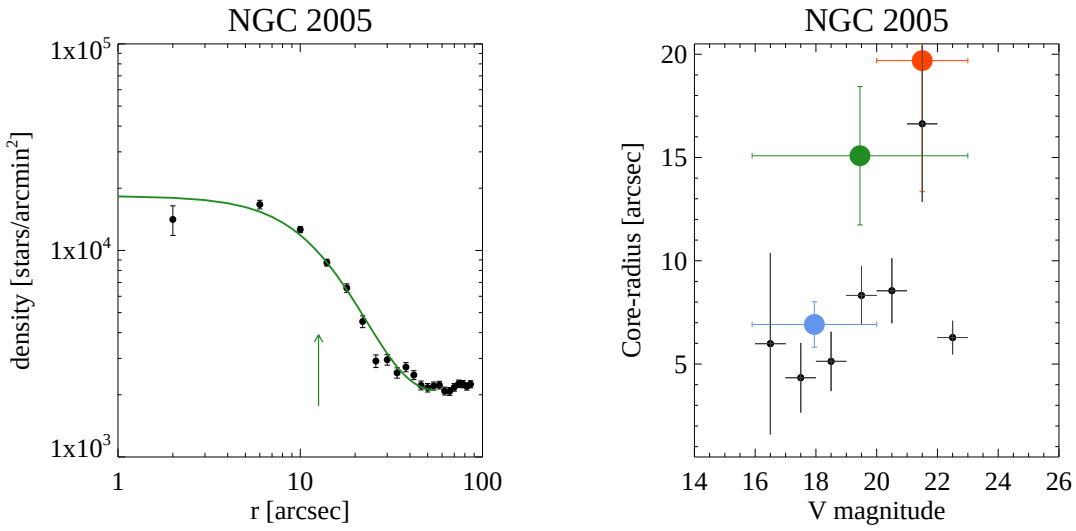

Figure 5.15: Left: RDP for cluster NGC 2005. Right: Same as Fig. 5.13 Right for cluster NGC 2005.

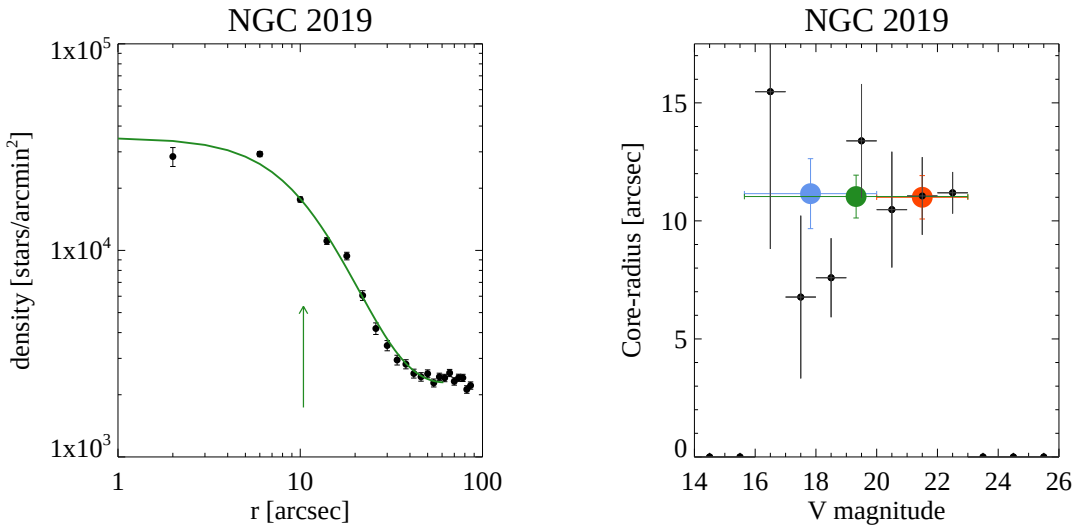

Figure 5.16: Left: RDP for cluster NGC 2019. Right: Same as Fig. 5.13 Right for cluster NGC 2019.

5.2.4 Stellar segregation assessment

In the right panel of Figures 5.13 to 5.16 the green circles mark the core-radius derived for the indicated cluster considering all magnitudes. When we consider

stars in groups, the *faint* stars (shown with red circles) generally have core-radii approximately twice as large as the *bright* stars (shown with blue circles). Inspecting the variation of the core-radius with stellar magnitude in Figure 5.13 we can conclude that the stellar distribution of NGC 1754 changes with magnitude – brighter stars are more centrally distributed, an indication of stellar segregation, possibly of dynamical origin.

NGC 1898 is one of the populous LMC star clusters. It is located in the outskirts of the LMC bar and the background/foreground density of the galaxy adds a significant contribution to the density profiles, as fitted by the f_b background density in Table 5.4. There is a jump in the estimated central density for magnitude $19 \leq V < 20$, which results in a core-radius of 8.44 arcsec. In the right panel of Figure 5.14, the cluster core-radius derived per magnitude bin shows a steady increasing trend with magnitude, an indication of mass segregation in the cluster.

The tendency of the core-radius with magnitude in NGC 2005 shows a trend of increasing for fainter magnitudes, and the groups of *bright* and *faint* stars support it (see Figure 5.15). The first and last data points are outliers, but this is not unexpected. The RDP for the brightest stars in the magnitude bin $16 \leq V < 17$ suffers from low-number statistics, so the uncertainties of the derived parameters are larger. The stars in the magnitude bin $22 \leq V < 23$, on the other hand, are more affected by the crowding and incompleteness effects, which distort the profile making it steeper with smaller core-radius.

The RDPs of NGC 2019 (Figure 5.16 Right) do not show significant tendency in the relation of the core-radius vs. magnitude. The profiles are smooth and similar in r_c for all magnitude bins within the uncertainty. These observational features give us the reason to reject the hypothesis of mass segregation in NGC 2019 from this study.

5.3 Comparison with previous results

Here we present a comparison of our results with a surface brightness profiles study of Mackey and Gilmore (2003) (hereafter M&G2003). In Figure 5.18 the core-radii determined in this Thesis are plotted against the core-radii of the same clusters determined by M&G2003 with the corresponding uncertainties. In circles are the

r_c we determine for a cluster (from all magnitudes of stars) compared to their r_c, while with triangles is our value for stars brighter than 20^m in V, compared to the measurement of Mackey and Gilmore (2003).

The differences are presented in Figure 5.17 between our measurements of *bright* stars and core-radii from Mackey and Gilmore (2003). The line indicates equality between the results. Our values are on average 2.5 arcsec larger, with a standard deviation of 1.73, than Mackey and Gilmore (2003) estimation.

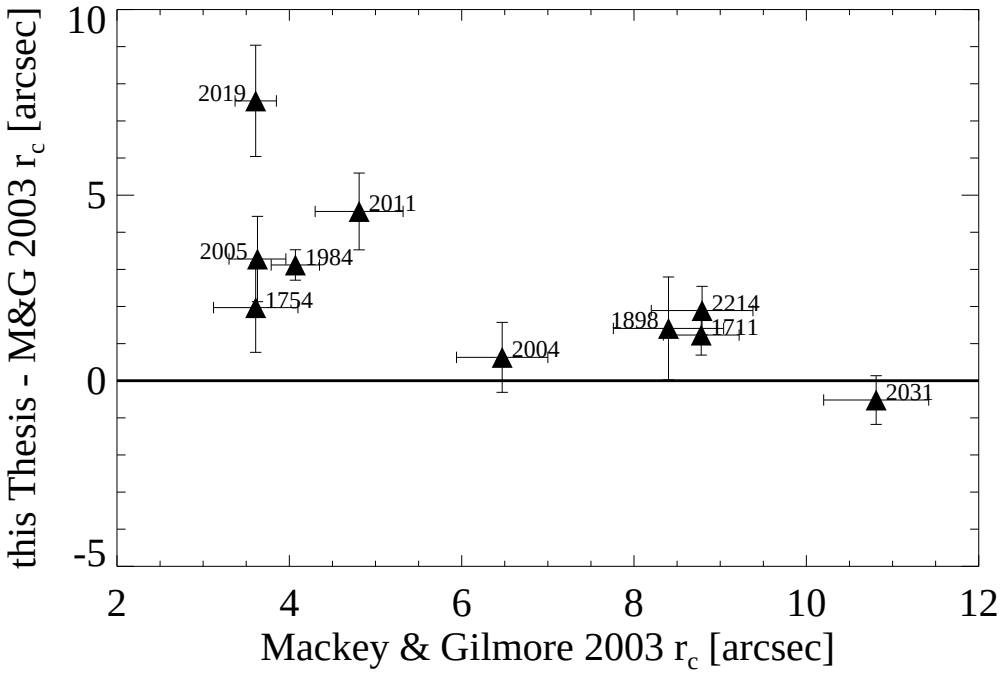

Figure 5.17: The differences between the core-radii derived for *bright* stars in this Thesis and the core-radii of the same clusters published by Mackey and Gilmore (2003). The line indicates equality between the measurements.

An important difference, which can explain the systematically larger radii determined by us: the profiles presented in this Thesis are number-density profiles based on star-counts, while Mackey and Gilmore (2003) use surface-brightness for the construction of the profiles. The brightest stars in a cluster contribute much more to the light profile than the fainter stars, while in the star-count profile all magnitudes of stars have equal weight. As a result the surface-brightness profiles

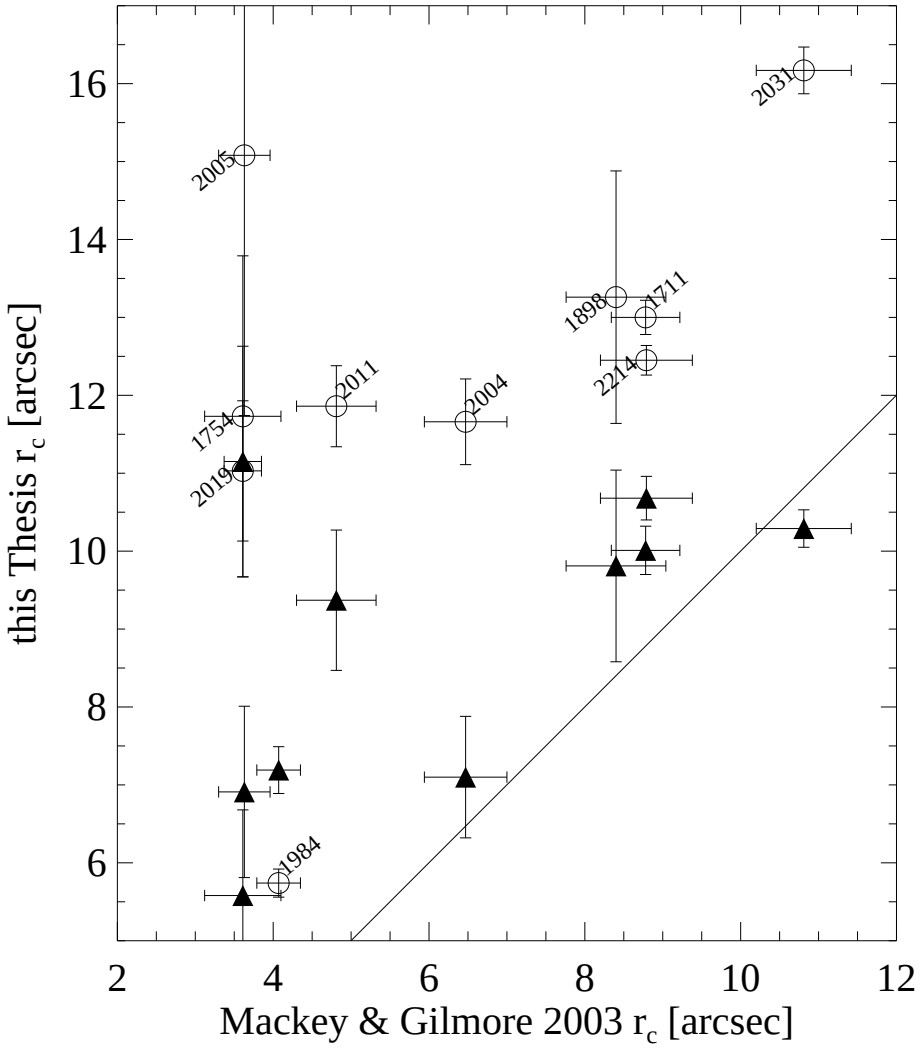

Figure 5.18: A comparison between the core-radii derived in this Thesis and the core-radii of the same clusters published by Mackey and Gilmore (2003) with the corresponding uncertainties. In circles are the r_c we determine for a cluster using all stars, while with triangles is our value of r_c for *bright* stars only. Cluster names as NGC numbers are labeled. The line indicates equality between the measurements.

of Mackey and Gilmore (2003) are representative mostly for the bright stars in the cluster, while our profiles represent also the more populous faint stars, as can be seen by the comparison in Figure 5.18. This also explain why the closest to the

values of r_c determined by Mackey and Gilmore (2003) are our estimated radii for the *bright* stars (plotted with triangles).

5.4 Summary

In this Chapter we presented a mass segregation study based on radial-density profiles of the LMC star clusters NGC 1711, NGC 1754, NGC 1984, NGC 1898, NGC 2004, NGC 2005, NGC 2011, NGC 2019, NGC 2031, and NGC 2214. The results presented in this Chapter are published in the following papers:

- Nikolov et al. (2009a): Nikolov, G.; Golev, V.; Kontizas, M.; Dapergolas, A.; Kontizas, E.; Bellas-Velidis, I., "The distortions in the density profiles in LMC clusters NGC 1850, NGC 2214 and BSDL 103", 2009, Annual of Sofia University "St. Kliment Ohridski", Faculty of Physics, vol.102, p.107

- Nikolov et al. (2010b): Nikolov, G.; Dapergolas, A.; Kontizas, M.; Golev, V.; Belcheva, M.; "Density profiles of populous star clusters in the Magellanic Clouds", 2010, Bulgarian Astronomical Journal, vol.14, p.43

- Nikolov et al. (2010c): Nikolov, G.; Dapergolas, A.; Kontizas, M.; Golev, V.; Belcheva, M.; "Density Profiles of Star Clusters in the Magellanic Clouds", 2010, Astronomical Society of the Pacific, vol.424, p.236

- Nikolov et al. (2010a): Nikolov, G.; Dapergolas, A.; Kontizas, M.; Golev, V.; "Indication of Stellar Stratification in Star Clusters in the Magellanic Clouds", 2010, Publications of the Astronomical Observatory of Belgrade, vol.90, p.73

- Nikolov et al. (2012): Nikolov, G.; Kontizas, M.; Dapergolas, A.; Belcheva, M.; Golev, V.; Bellas-Velidis, I.; "Indication of Mass Segregation in LMC Star Clusters", 2012, Astrophysics and Space Science Proceedings, vol.29, p.227

Chapter 6

Age of stellar content in LMC star clusters

The Magellanic Clouds give us the unique opportunity to study resolved stellar populations in star clusters. In this Chapter we present an age estimation of the stellar population of LMC star clusters BSDL 103, BSDL 101, NGC 2004 and NGC 2031.

6.1 Clusters BSDL 103 and BSDL 101 age and density map

The Magellanic Clouds are known to host a large variety of star clusters of various ages and morphology. Unlike the Milky Way, the Magellanic Clouds have suffered strong interactions among themselves and our galaxy through their lifetime. During those episodes, bursts of star and cluster formation has occurred, so a large number of star clusters are in the process of forming, still embedded in very disturbed environments and are often found in pairs.

This is the reason why we have selected such binary cluster candidate. Here we present the multiple cluster candidates BSDL 101 and BSDL 103 and KMHK 156, located in the LMC. The first two appear in the LMC extended catalog (Bica et al. 1999) and are not well studied yet. In this research we use archival data from Hubble Space Telescope WFPC2. The full list of the observations used is presented in detail in Table 2.2 and described in Section 2.

6.1.1 Colour-magnitude diagrams

For the photometric measurements we use the HSTphot package, as described in Sec. 3.1. The resulting catalogue of stars contains positions, data-quality parameters and magnitudes in Johnson's V and I filters, used for further analysis.

In order to establish the common origin of BSDL 101 and BSDL 103 we construct and compare their $(V, V-I)$ colour-magnitude diagrams. Figure 6.1 (right panel) presents BSDL 103 CMD, while in the left panel is the CMD of BSDL 101.

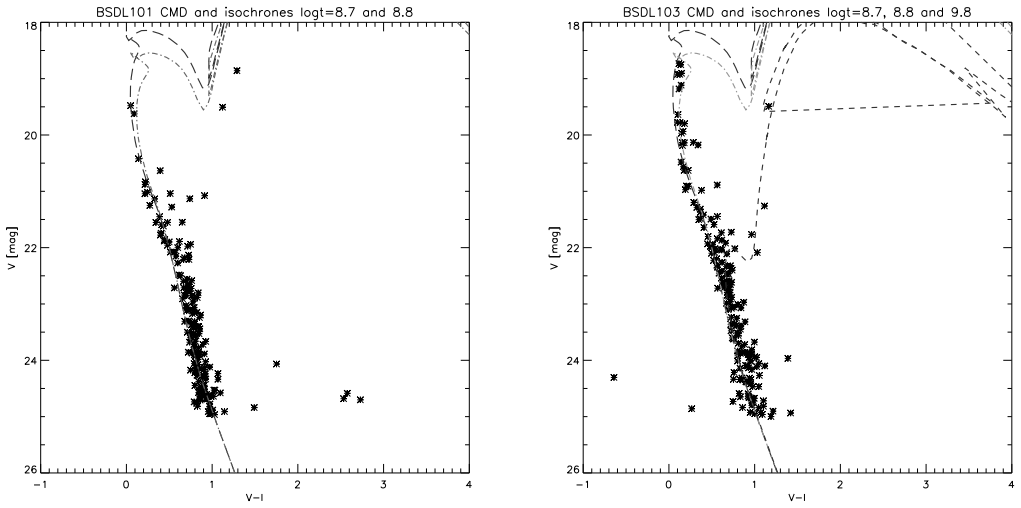

Figure 6.1: Left: CMD for the cluster BSDL 101. The same isochrones for $logage = 8.7$ and 8.8 as for the Figure 6.1 Right; Right: CMD for the cluster BSDL 103. The isochrone of $logage = 8.7$ (long-dashed line) and $logage = 8.8$ (dot-lined) well represent the cluster, while the one for $logage = 9.8$ (short-dashed line) represents the field stars.

To assess the ages of the stellar content of the clusters we use the PARSEC isochrones (Marigo et al. 2008). The isochrones overlayed in Figure 6.1 are computed for $logage = 8.7$ (long-dashed line) and 8.8 (dot-lined), corresponding to ages 5.01×10^8 and 6.31×10^8 years, respectively. We apply a LMC distance modulus of 18.5 to the isochrones to fit the observed stellar population. The age of the stellar population of both clusters lies in between the two fitted isochrones, or approximately 600 Myr and the uncertainty of ± 100 Myr arises from the low number of cluster stars. In the right panel of Figure 6.1 also an isochrone of $logage = 9.8$ (6.3×10^9 years) is shown by short-dashed line, as it well represents the observed population of field stars. We

made an investigation of the spatial distribution of the stars with $V - I > 0.75$ and $V < 22$ and found out that they are uniformly distributed in the field. The similarity of the CMDs and the best-fitting isochrones of the two clusters suggests that BSDL 101 and BSDL 103 are about the same age 600 ± 100 Myr and probably were born together from the same gas-dust cloud complex.

6.1.2 Density map

The stellar density maps can be used to trace the cluster's shape, morphology, bridges between the clusters or any hierarchical structure (Lada and Lada 2003; Santos-Silva and Gregorio-Hetem 2012). In Figure 6.2 we investigate the stellar density distribution by counting the stars in square bins of 0.8 pc wide or 64 Planetary Camera pixels. The derived density map illustrates that both clusters are small and seem embedded in the same larger structure, in which the stellar density is higher than the background away from the clusters. If they are coeval, then this map represents their original concentration from where they are born.

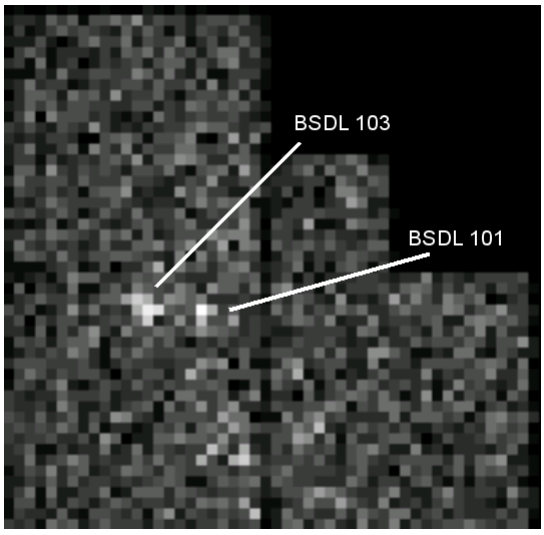

Figure 6.2: The stellar density map in and around the cluster BSDL 103. The size of the bin of the density map is 64 Planetary Camera pixels, corresponding to 0.8 pc at the distance of LMC.

KMHK 156 In field-of-view of the images we use we can find the object KMHK 156 located at RA= 04:51:00 and DEC=-70:01:24 degrees (J2000). It was categorized as a cluster in Kontizas et al. (1990) from ground-based observations. Our investigation of the WFPC2 images shows that it is actually two well resolved bright stars with an angular separation of 4.1 arcsec on the sky. They can not be resolved by the ground-based observations, but are easily recognized on the WFPC2 images, where they are resolved. An excerpt of the WFPC2 image in the area of the object is presented in Figure 6.3, with yellow ellipse is marked KMHK 156, while with blue circles are the two stars, which we subsequently identifiied in the Gaia DR2 (Gaia Collaboration et al. 2018) as sources ID 4654944864622880512 (G=13.08) and 4654944860325689984 (G=13.74).

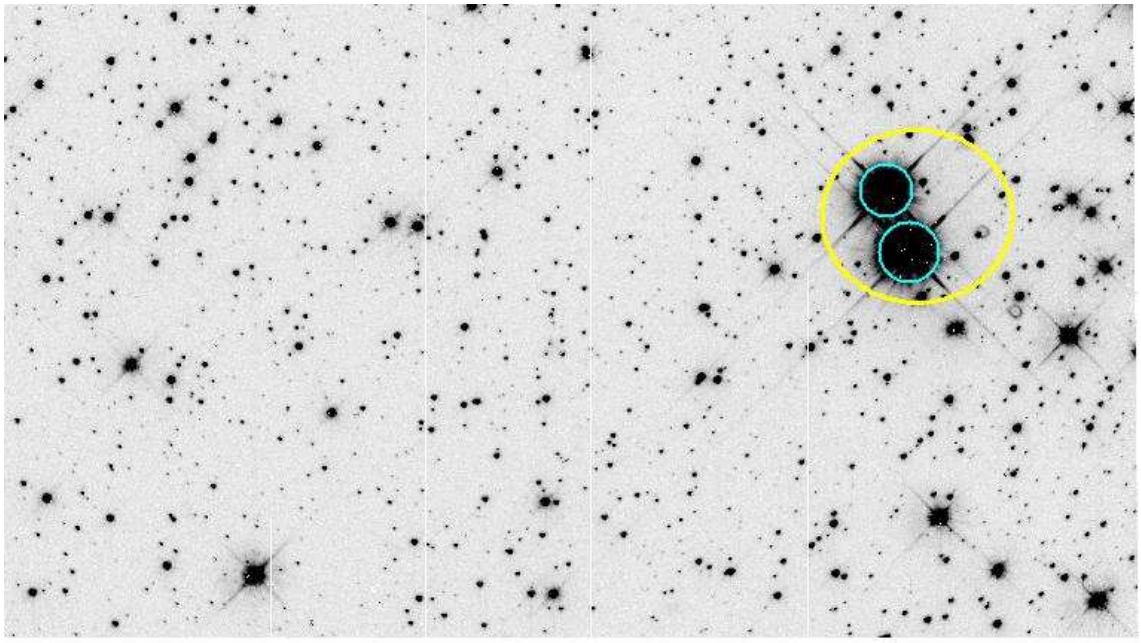

Figure 6.3: KMHK 156 ontop of WF3 CCD image, labeled in yellow ellipse. The two bright stars identified are indicated with blue circles.

6.1.3 Conclusion

Here we have constructed a density map of the clusters BSDL 103, BSDL 101 and the surrounding field to investigate the stellar density. We find out that BSDL 103

is a small cluster composed of bright Main Sequence stars. An isochrones fitting for the CMDs of BSDL 103 and BSDL 101 implies that the two clusters are the same age, $(6 \pm 1) \times 10^8$ years, and much younger than the field stars, which have an age of billions of years. The similarities of the CMDs suggest that these two clusters, BSDL 103 and BSDL 101, are coeval and most probably are a physical pair, embedded in the region where they are born.

6.2 NGC 2031 Stellar Populations

6.2.1 Introduction

For decades, astronomers have known that stars in star clusters are formed in one episode of star formation so that the stars in a cluster are coeval. However, recent discoveries of young stars in old clusters have changed these concepts (Girardi et al. 2009; Gratton et al. 2012). Extended main sequences and multiple stellar populations have been identified in intermadiate-age star clusters in the neighbouring Magellanic Clouds galaxies, but the interpretation is still unclear (Bastian et al. 2016; Cabrera-Ziri et al. 2015; Niederhofer et al. 2015).

Here we use WFPC2 images to show an example when color magnitude diagrams based based on observations from mosaic CCD camera can mimic a split in a cluster's Main Sequence. We use archival observations of the cluster NGC 2031 from the Hubble Space Telescope WFPC2 camera, obtained from the STScI archive. The observations are in the filters F555W and F814W, which correspond to Johnson's V and I. The different exposure times ensure that both bright and faint stars are well exposed and not saturated. Observations are presented in detail in Fischer et al. (1998). Details on the particular datasets used here are presented in Tables 2.1 and 2.2.

6.2.2 Photometry

The photometry was done using HSTphot package as described in Section 3.1.

The bad pixels, hot pixels and cosmic rays are removed from the images, as described in Section 3.1. The image sky level is determined prior the photometry

using the routine *getsky*. The sky level is recomputed also during the photometry to ensure better estimation.

The photometric solutions were done by the routine *hstphot*, as described in detail in Section 3.1. During the photometry an artificial star tests are conducted and we added 560000 artificial stars to estimate the completeness of the photometric data (see Section 3.1.5). For this cluster we experimented with sky background determination during *hstphot* photometry and two separate photometric catalogues were computed and compared, with only difference the sky estimation method.

Sky level determination

In fields with rapidly-varying background (e.g. star formation regions with gas clouds) or crowded regions it is recommended to estimate a local sky for each individual star just outside the photometry aperture. A drawback of this method is that it overestimates the sky background near the brightest stars. Our experiments showed that the background in the images used is not rapidly-varying on small scales of arcsec to demand a local sky determination. Alternativelly in HSTphot we can measure the global sky background for the whole CCD, a varying mean for each pixel, and produce a global sky level map for the camera.

In this study of NGC 2031 we did two runs of the photometric measurements - one with local sky (*hstphot* option = 2) and another with global sky level determination (*hstphot* option = 512). The resulting photometry lists are discussed below.

After the photometric measurements we corrected the positions of the objects for the geometric distortions of the camera using Holtzman et al. (1995a) corrections by the routine *distort*. On the output photometry list we apply a data quality selection. We reject objects, which do not cover the data-quality criteria and keep only stars with good photometry, as described in Section 3.2.

6.2.3 MS splitting effect

Figure 6.4 presents the difference of the CMDs derived from photometry with and without local sky determination during photometry. On this figure, for visibility, the four WFPC2 CCDs are marked with different symbols and only stars lying on the WF3 only are coloured in grey. It is evident, that when the sky is determined locally,

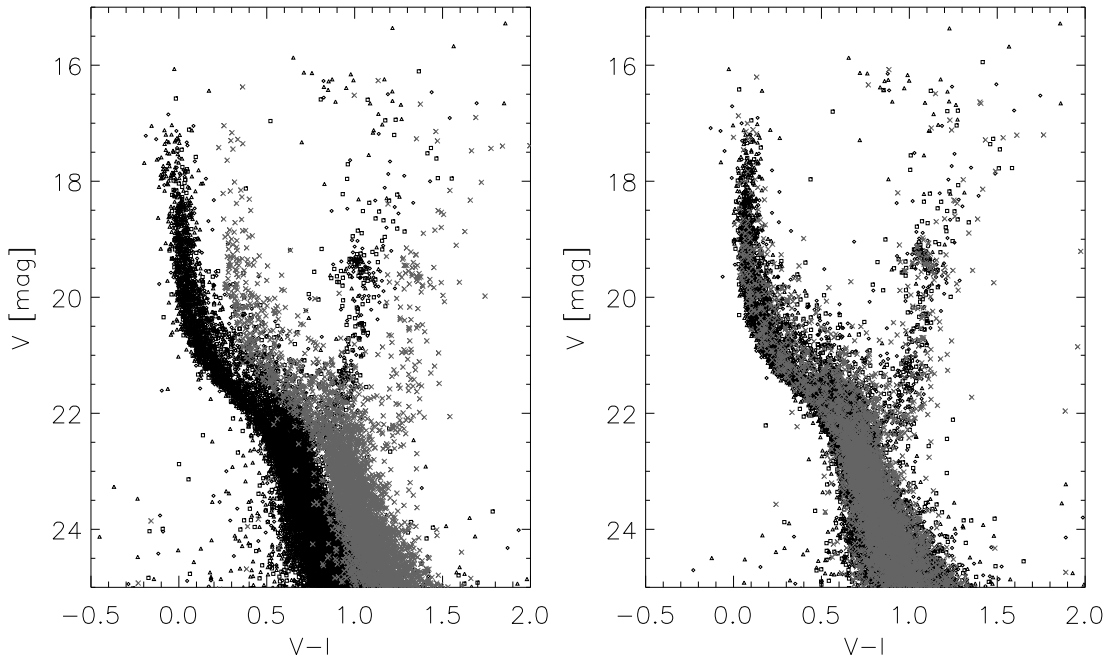

Figure 6.4: Left: CMD of the cluster NGC 2031 in standard filters V and I with stars from different WFPC2 CCDs denoted: PC as triangle, WF2 as diamond, WF4 as square, and WF3 as X (cross) and grey in colour, Right: Same as Left, global sky determination.

the stars from the WF3 are shifted in colour with respect to the color indices of the stars from the other three CCDs, broadening the Main Sequence and mimicking an older population in the cluster, or extended Main Sequence turn-off. We use images of different exposure times, so the shift is well visible in both bright and faint stars.

For comparison, the CMD of the cluster when estimating the sky level globally during photometry is presented in Figure 6.4 Right. In this case the stars from all CCDs of the camera are distributed in the same areas of the CMD, with no apparent shifts greater than the photometric uncertainties.

The root of this discrepancy is in the aperture corrections erroneously determined when local sky for the stars is computed (Dolphin, A., private communication), which consequently affect the photometric zeropoint applied to every CCD. In Table 6.1 are listed the aperture corrections applied to the photometry in the cases of local and global sky determination. When the sky is considered locally, (*hstphot* option

Table 6.1: Aperture corrections mean determined for the four CCDs of WFPC2, in magnitudes.

WFPC2 CCD	local sky	global sky
PC	0.377	0.102
WF2	0.134	0.046
WF3	0.343	0.047
WF4	0.167	0.048

= 2) then the aperture corrections in I are overestimated by the order of $0.20 - 0.25$ magnitudes, reaching 0.30 in WF3, compared to the other WFC frames, whose pixels are identical. The PC pixel size is half of the WFC pixel size, its value for aperture corrections is expected. This results in a shift on the CMD, as seen in Figure 6.4 Right. On the other hand, when the sky level is determined globally (*hstphot* option = 512), the aperture corrections applied for the three WF frames are identical, 0.047^m. Then the resulting CMD of the cluster is as expected of a single stellar population, as the one observed by Mould et al. (1993). The natural spread in colour of the main sequence in Figure 6.4 Right is much smaller, making the features on the CMD much prominent.

Many of the cameras nowadays used with the modern telescopes are a mosaic of several CCD sensors, e.g. WFC3 (Dressel 2017), SDSS (Gunn et al. 1998), Gaia (de Bruijne et al. 2010), and other. Here we show how important it is to consider the whole camera as one, though dealing with individual CCD sensors. We argue that the cluster NGC 2031 colour-magnitude diagram can be represented well by single stellar population models.

6.2.4 Age determination

Currently various theoretical models of stellar evolution exist. They are constantly improved to be more realistic, taking into account the limb darkening effects, stellar rotation, latest estimates of the solar abundance of the chemical elements, etc. In recent study Martins and Palacios (2013) made a comparison between the currently

available evolutionary tracks for massive stars and conclude that the stellar evolution beyond the Main Sequence is currently not well understood. The models include evolution through a red giant stage or a supergiant, but the correct positions on the Hertzsprung-Russel diagram, the exact luminosity and temperature the models can not yet predict. This fact is a motivation for us when fitting isochrones to the observed stellar population to try to model with higher confidence the Main Sequence and its turn-off point.

In the last decade a synthetic clusters have been developed (Ekström et al. 2012; Georgy et al. 2013), which allow for a direct comparison between the theory and observations. In this study we modelled the population of star cluster NGC 2031 by means of theoretical isochrones from the Padova group and corresponding synthetic model from the developed in the recent years by the Geneva group.

We use the V and I filter photometry to construct the CMD of the cluster to which we first fit the PARSEC v1.2S isochrones, described in Marigo et al. (2017). We find metallicity $Z = 0.0056$ to best describe the stellar population of NGC 2031, which is typical for LMC star clusters (Livanou et al. 2013). In Figure 6.5 a set of isochrones with logarithm of age 8.30, 8.35, 8.40, 8.45, 8.50 is presented.

To convert the isochrones absolute magnitudes to the observed V and I, a distance modulus of $(m - M)_0 = 18.48$ to the Large Magellanic Cloud is used (Inno et al. 2016). The reddening is estimated to be $E(V - I) = 0.17$ towards NGC 2031.

When fitting the observed stellar population with isochrones it is necessary to fit the blue part of the Main Sequence, since these are the positions of the single stars of the cluster. Unresolved binaries lie above the MS, thus making it wider in colour. From this set of isochrones we find the best-fitting isochrone of PARSEC models that fits the observed stellar population on the main sequence, and both the turn-off point and the giants has an age of 230 million years, or $logage = 8.35$.

For further comparison we use synthetic cluster simulated based on the models developed by Georgy et al. (2013), which cover stars with masses from 1.7 to 15 solar masses and metallicity $Z = 0.014(= Z\odot), 0.006, 0.002$. On the simulated population we again apply the distance modulus and reddening towards NGC 2031 to fit the observed cluster population. In figure 6.5 the simulated population of unresolved binaries is clearly visible, lying to the red and above the Main Sequence. From the existing models, the ones with metallicity of $Z = 0.0060$ are most suitable

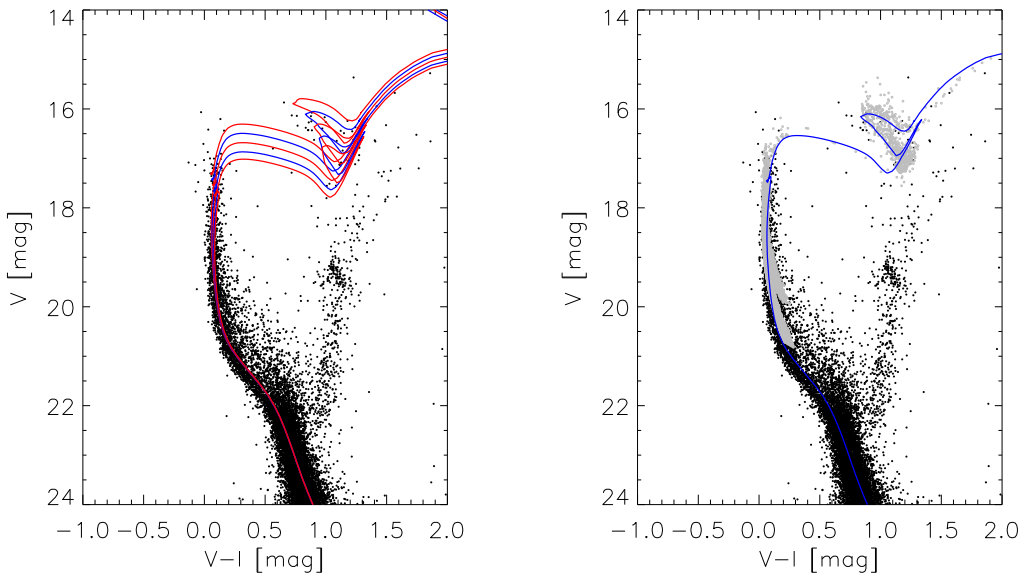

Figure 6.5: PARSEC isochrones of $logage = 8.30, 8.35, 8.40, 8.45, 8.50$ fitted to the observed NGC 2031 population.

for NGC 2031.

We requested a simulation of 9000 stars, comparable with the real number of observed stars in the images used. The fraction of unresolved binary stars is set to 30% during simulation and normal distribution of photometric uncertainty is applied with an amplitude of 0.05 in filter V and 0.08 in colour $V - I$. From the simulated cluster population we estimate the synthetic population that best represents the observed stellar population of NGC 2031 has a metallicity $Z = 0.006$ and is 224 million years old.

From the synthetic cluster and isochrone fitting we can conclude that the stellar population of NGC 2031 has an age of 227 Myr ± 3 Myr and metallicity $Z = 0.0058 \pm 0.0002$. This estimation makes NGC 2031 one of the youngest populous star clusters in the LMC.

6.3 Characterising LMC Star Cluster NGC 2004

NGC 2004 is a young populous star cluster from the Large Magellanic Cloud (LMC) located at RA=82.670208 and DEC=-67.288055 degrees (J2000). In this study we provide an accurate age estimate using the latest PARSEC and SYCLIST theoretical models of evolution.

6.3.1 Observations and photometry

For the purpose of stellar photometry performed in this study we use an archive observations of NGC 2004 taken WFPC2 onboard Hubble Space Telescope. The observations used are presented in Tables 2.1 and 2.2.

The photometry was done using HSTphot, following the procedures described in Section 3.1. The photometric solutions were done by the *hstphot* routine. During the photometry the global sky background is recomputed (*hstphot* option = 512), as recommended for general use in the HSTphot manual (Dolphin 2000b).

To account for the geometric distortions of the cameras corrections of Holtzman et al. (1995b) were applied additionally using the *distort* routine and the individual frame coordinates were translated to a global coordinate system with respect to the PC pixel coordinates. Final quality selection was performed to objects presenting the output photometry list with Johnson's V and I stellar magnitudes and positions. This way a list containing 8984 objects was prepared and used for further exploration.

6.3.2 Surface density profile

The radial profile of a cluster provides structural parameters, such as core-radius, radius of tidal stripping from the host galaxy, or concentration of the cluster. These parameters are linked to the dynamical state of the cluster (see King (2008); Meylan and Heggie (1997)) and can be used to assess mass segregation, core-collapse, expansion Bonnell and Davies (1998); Mackey et al. (2008).

A surface-number radial density profile has been constructed to determine structural parameters of the cluster NGC 2004. In Figure 6.6 Right panel, the Y error bars represent Poisson uncertainties, while the radial step on X axis is 4 arcseconds.

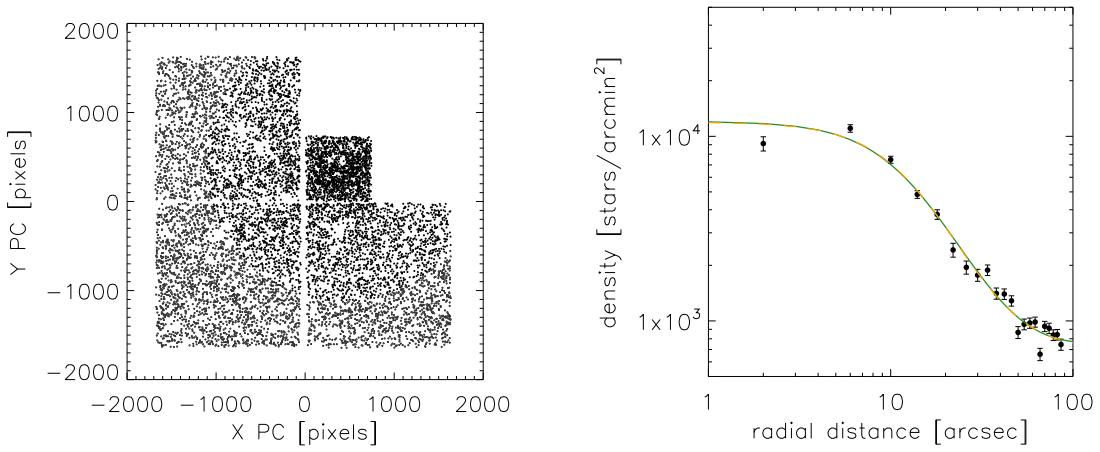

Figure 6.6: Left panel: Stars of NGC 2004. In grey are objects considered to be field contamination from the LMC. In black are stars of the inner region, centered on the cluster core. Right panel: Number density profile in logarithmic scale. Best-fitting King model is plotted with a solid line in green, while the best-fitting Elson et al. (1987) model is with dashed line in orange.

To the cluster radial-density profile we fitted an Elson et al. (1987) model, in the form of Equation 4.4. It is presented with dashed line in orange on Figure 6.6. The derived core-radius of the EFF87 model is $r_c = 11.66 \pm 0.55$ arcsec, with parameters of the model, scale parameter $a = 14.06 \pm 1.07$, $\gamma = 2.64 \pm 0.15$, central density $f_0 = 11145 \pm 790$ and background density $f_b = 703 \pm 21$ stars per square arcmin. To test our results we also fitted an King (1966) model to this cluster. The best-fit to the observed cluster's stellar density profile (Figure 6.6 Right panel, continuous curve) was achieved for King-like model with a core-radius of $r_c = 11.99 \pm 1.88$ arcsec. At the adopted distance modulus to the cluster $(m - M)_0 = 18.45$ this translates to a radius of 2.85 ± 0.46 parsecs. The estimated tidal-radius is $r_t = 134 \pm 93$ arcsec, the central maximum density $f_0 = 13618 \pm 1827$ and background density $f_b = 760 \pm 120$ stars per square arcminute. The two models are indistinguishable, except in the most outer parts out of the fitting area. The core-radius derived from the EFF87 model is, within the uncertainty, the same as the core-radius determined from King model fitting.

6.3.3 Colour-magnitude diagram and field decontamination

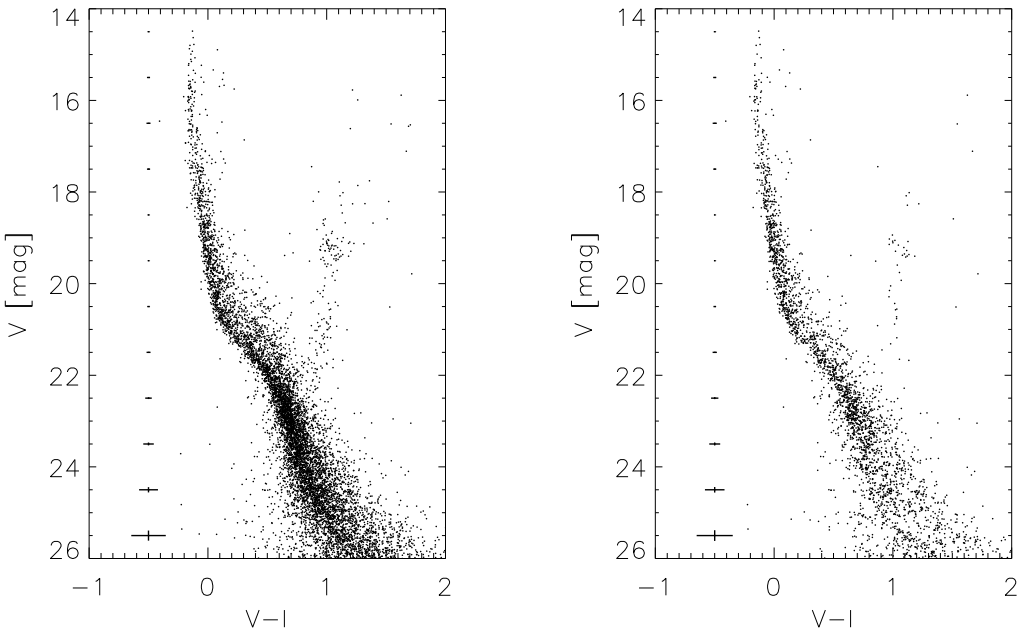

Figure 6.7: CMD of the cluster NGC 2004. Left panel: all objects from the photometry list. Right panel: Stars of the cluster population, after the field decontamination.

The observed $(V, V-I)$ colour-magnitude diagram (CMD) is presented in Figure 6.7, Left panel. Representative error bars along the two axes are shown to the left of the diagram. As expected, the observed CMD is affected by field stars from the host LMC galaxy. In order to account for the contamination of the LMC field stars on the NGC 2004 CMD stars from two different cluster fields was used to construct the CMD. The procedure is described in Bastian et al. (2016) and discussed in detail in Cabrera-Ziri et al. (2016a). In this approach two different regions, one in the central part and another representing the sparse outer regions of the cluster are chosen to build the observational CMD. The radius of the area centered on the cluster core was adopted in accordance with the core radius derived in the previous subsection being 6 times larger than r_c (72 arcsec).

The central region contains 5530 stars. As a second step a reference field covering approximately the same area as the first one, but not larger, was chosen. The field

reference region presents stellar density as far from the cluster center as possible, reaching up-to the outer edges of the WFC. In our case the reference region contains 3454 stars. As a final step for every star in the CMD of the reference field, the star in the cluster CMD that is closest to the reference field star in colour-magnitude space was rejected. This way stars of the field area were matched on the $(V, V-I)$ plane with stars of the inner area, the latter being flagged and removed from the photometry list. Matching is performed in *topcat* (Taylor 2005) by finding the closest match on the colour-magnitude diagram with tolerance 1 magnitude in both color $V-I$ and V magnitudes. In this way one reduced photometry list was derived. It contains 3201 stars all located in the inner area. These stars are considered to be real cluster stars, objects with highest probability of belonging to the cluster population (Figure 6.7, Right panel).

6.3.4 Isochrones fitting and synthetic cluster

To estimate the age of NGC 2004 the PARSEC isochrones from the Astronomical Observatory of Padova (Marigo et al. 2017) were used. Fitting is done on the cleaned decontaminated cluster population, by finding the isochrone that best represents the Main Sequence (MS) until the turn-off point. The isochrone itself represents the population of single stars forming the MS. This is the reason we fit the isochrone to this part of the observed CMD, ignoring unresolved binaries that lie above and to the red of the MS. In Figure 6.8, Left panel, the isochrones with logarithm of the age $logage = 7.0, 7.1, 7.2, 7.3, 7.4$ are shown with yellow lines.

The metallicity $Z = 0.008$ and reddening $E(V-I) = 0.3$ of NGC 2004 are accepted with accordance to other studies of LMC clusters (Brocato et al. 2001; Niederhofer et al. 2015). Taking into account these values and following the best-fitting isochrone from the used set of models (Figure 6.8) we accept the age of NGC 2004 to be 16 Myr ($logage = 7.2$). It confirms exactly the age determined based on HST data by Keller et al. (2000). For the completeness of the study we have to point that Niederhofer et al. (2015) found that the position of helium burning stars on their $(V, B-V)$ diagram is best reproduced by an isochrone corresponding to 20 Myr which resembles the value declared by Elson (1991). The CMD in our work based on deep HST WFPC2 data reaches a considerably deeper limit in magnitudes,

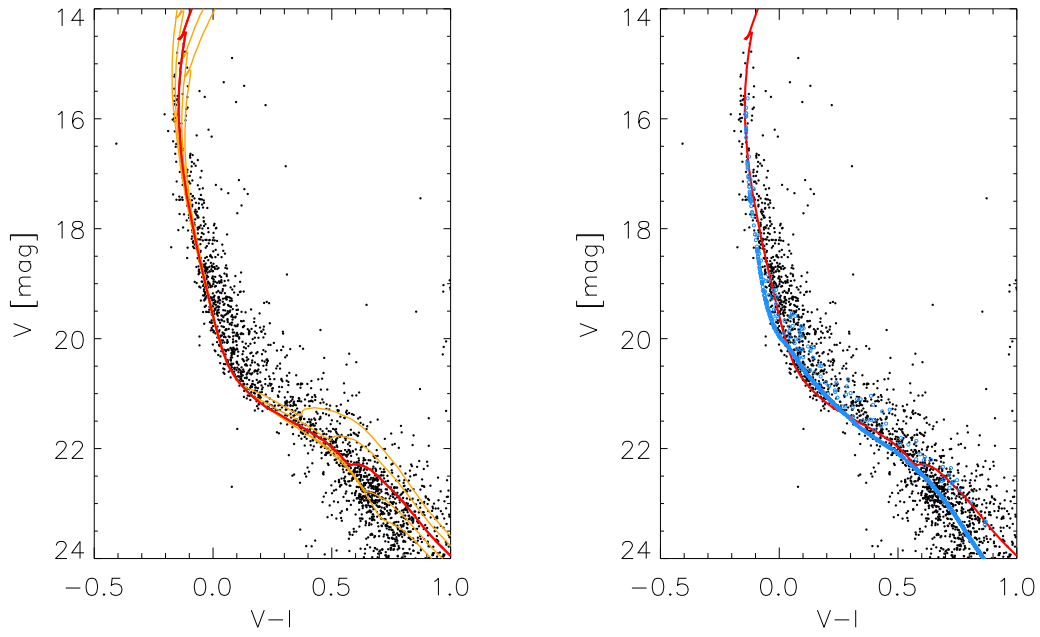

Figure 6.8: Final CMD of the cluster NGC 2004 cleaned for field stars contamination. Left panel: PARSEC isochrones of *logage* = 7.0, 7.1, 7.2, 7.3, 7.4 drawn, the one corresponding to an age of 16 Myr is shown with red line. Right panel: Best-fitting PARSEC isochrone of age 16 Myr is shown with red line, synthetic clusters simulated from SYCLIST are shown with blue and green circles

compared to other published studies of NGC 2004 (Brocato et al. 2001; Niederhofer et al. 2015).

For validation of the results from isochrones fitting, we requested a simulation of a synthetic cluster by the SYCLIST tool from the Geneva stellar models. Such approach is presented in Georgy et al. (2014) on the galactic cluster NGC 663.

In this work the number of simulated stars is 1000, a representative number comparable to the number of cluster stars cleaned of field. Using the age found from the isochrones fitting in the previous section and the accepted LMC metalicity, a synthetic cluster model was simulated from the available grids with two rotation rates and stellar masses covering a mass range from 0.8 to 120 solar masses (large grids). A binarity fraction of 30% was simulated, typical for LMC clusters (Li et al. 2013). From a spectroscopic study the fraction in this cluster is reported

to be 23% (Evans et al. 2010, 2006). A photometric noise of 0.1 magnitudes on the simulated stars was also accepted as a simulation parameter. The CMD of the synthetic clusters is presented in Figure 6.8, Right panel with blue circles. We found that the observed and synthetic CMDs are in good agreement. The observed discrepancies could be explained by the inherent differences between PARSEC and SYCLIST models and the lower metallicity (Z=0.002) of the best-fitting isochrone from the PARSEC models. The unresolved binaries, both synthetic and observed, are located above the Main Sequence population, while at magnitudes fainter than 22^m a negligible residue of field LMC stars can be identified.

Conclusion

In this work we present precise two band (V,I) photometry of more than 3000 stars, members of stellar cluster NGC 2004. Age estimation of 16 Myr was obtained using isochrone fitting and single stellar population models. A good agreement of the observed color-magnitude diagram with the one derived on the base of simulated synthetic cluster (Geneva SYCLIST tool) adopting 16 Myr cluster age with 30% binarity fraction is demonstrated.

6.4 Summary

In this Chapter we presented an age estimation of the LMC star clusters BSDL 103, BSDL 101, NGC2004, and NGC 2031 by fitting theoretical isochrones. The derived ages of NGC 2004 and NGC 2031 are compared to synthetic cluster models. The results presented in this Chapter are published in the following papers:

- Nikolov et al. (2009b): Nikolov G.; Kontizas, M.; Dapergolas, A.; Kontizas, E.; Golev, V.; Bellas-Velidis, I.; "The distortions in the density profiles of star clusters of the Magellanic clouds", 2009, Publ. Astr. Soc. "Rudjer Boskovic", No. 9, p.363

- Nikolov, G.; "Age determination of star cluster NGC 2031 through isochrones and a synthetic cluster model", 2017, Proceedings of "120 years Astronomical

Observatory at Sofia University "St. Kliment Ohridski"", (in Bulgarian), vol.1, p.22 fulltext

- Nikolov (2018a): Nikolov, G.; "Mimicking multiple stellar populations", 2018, Memorie della Societa Astronomica Italiana, vol.89, p.85
- Nikolov and Markov (2019): Nikolov, G.; Markov, H.; "Characterising LMC Star Cluster NGC 2004", 2019, AIP Conference Proceedings, vol.2075, p.090005

Chapter 7

Contributions

Main contributions:

- in this Thesis a detailed study on the Large Magellanic Cloud star clusters NGC 1711, NGC 1754, NGC 1984, NGC 1898, NGC 2004, NGC 2005, NGC 2011, NGC 2019, NGC 2031, and NGC 2214 is presented
- radial density profiles for various magnitudes of the stars were constructed for the studied clusters and the variation of the core-radii vs. magnitude is used as a method to assess mass segregation
- EFF87 model (Elson et al. 1987) is fitted to the RDP of the clusters NGC 1711, NGC 1984, NGC 2004, NGC 2011, NGC 2031, NGC 2214 and their structural parameters determined
- King model (King 1962) is fitted to the old LMC star clusters NGC 1754, NGC 1898, NGC 2005, NGC 2019 and their structural parameters determined
- mass segregation in NGC 1711 and NGC 2004 is confirmed
- an evidence of mass segregation in the clusters NGC 2011, NGC 2031, and NGC 2214 is observed, unlike NGC 1984
- an indication of stellar mass segregation, possibly of dynamical origin, is observed in the old star clusters NGC 1754, NGC 1898 and NGC 2005

- An isochrones fitting for the CMDs of BSDL 103 and BSDL 101 implies that the two clusters are the same age, $(6 \pm 1) \times 10^8$ years, and much younger than the field stars, whose age we assess to approximately 6.3 Gyrs. We argue that the similarity of BSDL 103 and BSDL 101 colour-magnitude diagrams suggests that both clusters are coeval and most probably are a physical pair

- the object, categorized as a cluster KMHK 156 is actually two bright stars of magnitudes G=13.08 and G=13.74 with a small separation of 4.1 arcsec on the sky. This result is obtained thanks to the use of high resolution WFPC2 images in this study

- we demonstrate on NGC 2031 how an eMSTO effect can be achieved only through the sky determination during photometry of multiple-CCD cameras. In the presented case, in the CMD of the cluster the stars from WF3 CCD are shifted in colour with respect to the other CCDs

- using synthetic cluster simulations and isochrone fitting, we estimated that the stellar population of NGC 2031 has an age of 227 ± 3 Myr and metallicity $Z = 0.0058 \pm 0.0002$ with reddening estimated to $E(V - I) = 0.17$ towards the cluster

- for cluster NGC 2004 an age estimation of 16 ± 4 Myr is obtained using single stellar population isochrone fitting and a synthetic cluster simulation. The reddening towards the cluster is estimated to be $E(V - I) = 0.3$

List of publications, talks and posters

This work is based on the following publications:

1. Nikolov G.; Kontizas, M.; Dapergolas, A.; Kontizas, E.; Golev, V.; Bellas-Velidis, I.; “The Distortions in the density profiles of star clusters of the Magellanic clouds”, 2009, Publ. Astr. Soc. "Rudjer Boskovic", No. 9, p.363 Nikolov et al. (2009b) 2009PASRB...9..363N

2. Nikolov, G.; Golev, V.; Kontizas, M.; Dapergolas, A.; Kontizas, E.; Bellas-Velidis, I., “The distortions in the density profiles in LMC clusters NGC 1850, NGC 2214 and BSDL 103”, 2009, Annual of Sofia University "St. Kliment Ohridski", Faculty of Physics, vol. 102, p.107 Nikolov et al. (2009a) fulltext

3. Nikolov, G.; Dapergolas, A.; Kontizas, M.; Golev, V.; Belcheva, M.; "Density profiles of populous star clusters in the Magellanic Clouds", 2010, Bulgarian Astronomical Journal, vol.14, p.43 Nikolov et al. (2010b) 2010BlgAJ..14...43N

4. Nikolov, G.; Dapergolas, A.; Kontizas, M.; Golev, V.; Belcheva, M.; "Density Profiles of Star Clusters in the Magellanic Clouds", 2010, Astronomical Society of the Pacific, vol.424, p.236 Nikolov et al. (2010c) 2010ASPC..424..236N

5. Nikolov, G.; Dapergolas, A.; Kontizas, M.; Golev, V.; "Indication of Stellar Stratification in Star Clusters in the Magellanic Clouds", 2010, Publications of the Astronomical Observatory of Belgrade, vol.90, p.73 Nikolov et al. (2010a) 2010POBeo..90...73N

6. Nikolov, G.; Kontizas, M.; Dapergolas, A.; Belcheva, M.; Golev, V.; Bellas-Velidis, I.; "Indication of Mass Segregation in LMC Star Clusters", 2012, Astrophysics and Space Science Proceedings, vol.29, p.227 Nikolov et al. (2012) 2012ASSP...29..227N

7. Nikolov, G.; Kontizas, M.; Dapergolas, A.; Belcheva, M.; Golev, V.; Bellas-Velidis, I.; "Distribution of stars in three Magellanic Clouds star clusters NGC 1754, NGC 2005, NGC 2019", 2013, Bulgarian Astronomical Journal, vol.19, p.9 Nikolov et al. (2013) 2013BlgAJ..19....9N

8. Nikolov, G.; "Age determination of star cluster NGC 2031 through isochrones and a synthetic cluster model", 2017, Proceedings of "120 years Astronomical Observatory at Sofia University "St. Kliment Ohridski"", (in Bulgarian), vol.1, p.22 fulltext

9. Nikolov, G. B.; "Precise astrometry from half-century long observations of star cluster M 15", 2018, Astronomical and Astrophysical Transactions, vol.30, p.417 Nikolov (2018b) 2018A&AT...30..417N

10. Nikolov, G.; "Mimicking multiple stellar populations", 2018, Memorie della Societa Astronomica Italiana, vol.89, p.85 Nikolov (2018a) 2018MmSAI..89...85N

11. Nikolov, G.; Markov, H.; "Characterising LMC Star Cluster NGC 2004", 2019, AIP Conference Proceedings, vol.2075, p.090005 Nikolov and Markov (2019) 2019AIPC.2075i0005N

Posters and oral presentations

Results are presented in the following meetings:

- 2008, VI Serbian-Bulgarian Astronomical Conference, Belgrade, Serbia
- 2009, IX Hellenic Astronomical Conference, Athens, Greece
- 2009, "Four centuries modern astronomy", Smolyan, Bulgaria (in Bulgarian)
- 2009, SREAC, Belgrade, Serbia
- 2010, JENAM, Lisbon, Portugal
- 2011, JENAM, St. Petersburg, Russia
- 2011, "30 years NAO", Smolyan, Bulgaria
- 2012, VIII SBAC, Leskovac, Serbia
- 2012, VII SAB, Dimitrovgrad, Bulgaria, (in Bulgarian)
- 2016, XI SAB, Kardjali, Bulgaria, (in Bulgarian)

- 2017, EWASS Symp. 9: Star cluster formation history in the Magellanic Clouds, Prague, Czech Republic
- 2017, "120 years Astronomical Observatory at Sofia University "St. Kliment Ohridski"", Sofia, Bulgaria, (in Bulgarian)
- 2018, 10th Jubilee Conference of the Balkan Physical Union, Sofia, Bulgaria

Participation in schools and workshops:

- 2008 Chemical Odyssey of the Elements, Aegina Greece
- 2008 III NEON Archive Observing School, ESO, Garching, Germany
- 2009 Euro-VO AIDA, ESO, Garching, Germany
- 2010 Gaia: at the frontiers of astrometry, Paris, France
- 2010 Extragalactic science with Gaia, IAP, Paris, France
- 2013 OPTICON Awareness conference, Bucharest, Romania
- 2014 GREAT Workshop: Young Clusters in the Gaia-ESO Survey, Palermo, Italy

Future prospects

In the current Thesis we determined structural parameters of the studied clusters. Now we are able to model them via direct N-body simulations. Especially since we know how various mass groups are distributed we can compare the model with the actual observations. We also have an accurate age estimation of NGC 2004 and NGC 2031 and have an adequate synthetic cluster population model simulated. This way we can compare the simulated results of the dynamical state at the actual age determined for a cluster. Next in this studies of LMC star clusters is to determine accurate age of the other star clusters in our sample.

List of Figures

List of Tables

Nomenclature

r_c Core-radius, King

r_t Tidal-radius, King

T_c Crossing time

T_e Evolution time

T_{rlx} Relaxation time

eMSTO extended Main Sequence Turn-Off

HST Hubble Space Telescope

LMC Large Magellanic Cloud

PC Plenetary Camera of WFPC2

PSF Point spread function

RDP Radial density profile

SMC Small Magellanic Cloud

WFC Wide Field Camera of WFPC2

WFPC2 Wide Field and Planetary Camera 2

References

Allison, R. J., Goodwin, S. P., Parker, R. J., de Grijs, R., Portegies Zwart, S. F., and Kouwenhoven, M. B. N. (2009a). Dynamical Mass Segregation on a Very Short Timescale. ApJ, 700:L99–L103. 5, 8

Allison, R. J., Goodwin, S. P., Parker, R. J., Portegies Zwart, S. F., de Grijs, R., and Kouwenhoven, M. B. N. (2009b). Using the minimum spanning tree to trace mass segregation. MNRAS, 395:1449–1454. 10

Anderson, J. and King, I. R. (1999). Astrometric and Photometric Corrections for the 34th Row Error in HST's WFPC2 Camera. PASP, 111:1095–1098. 27

Bastian, N., Cabrera-Ziri, I., Niederhofer, F., de Mink, S., Georgy, C., Baade, D., Correnti, M., Usher, C., and Romaniello, M. (2017). A high fraction of Be stars in young massive clusters: evidence for a large population of near-critically rotating stars. MNRAS, 465:4795–4799. 12

Bastian, N. and Lardo, C. (2018). Multiple Stellar Populations in Globular Clusters. *Annual Review of Astronomy and Astrophysics*, 56:83–136. 12

Bastian, N., Niederhofer, F., Kozhurina-Platais, V., Salaris, M., Larsen, S., Cabrera-Ziri, I., Cordero, M., Ekström, S., Geisler, D., Georgy, C., Hilker, M., Kacharov, N., Li, C., Mackey, D., Mucciarelli, A., and Platais, I. (2016). A young cluster with an extended main-sequence turnoff: confirmation of a prediction of the stellar rotation scenario. MNRAS, 460:L20–L24. 12, 67, 75

Baumgardt, H., Parmentier, G., Anders, P., and Grebel, E. K. (2013). The star cluster formation history of the LMC. MNRAS, 430:676–685. 3

Bertelli, G., Mateo, M., Chiosi, C., and Bressan, A. (1992). The star formation history of the Large Magellanic Cloud. ApJ, 388:400–414. 3

Bertelli, G., Nasi, E., Girardi, L., Chiosi, C., Zoccali, M., and Gallart, C. (2003). Testing Intermediate-Age Stellar Evolution Models with VLT Photometry of Large Magellanic Cloud Clusters. III. Padova Results. AJ, 125:770–784. 12

Besla, G., Kallivayalil, N., Hernquist, L., Robertson, B., Cox, T. J., van der Marel, R. P., and Alcock, C. (2007). Are the Magellanic Clouds on Their First Passage about the Milky Way? ApJ, 668:949–967. 1

Bhatia, R. K. and Hatzidimitriou, D. (1988). Binary star clusters in the Large Magellanic Cloud. MNRAS, 230:215–221. 3

Bhatia, R. K. and MacGillivray, H. T. (1988). NGC 2214 - A merging binary star cluster in the Large Magellanic Cloud? A&A, 203:L5–L8. 52

Bica, E., Bonatto, C., Dutra, C. M., and Santos, J. F. C. (2008). A general catalogue of extended objects in the Magellanic System. MNRAS, 389:678–690. 3

Bica, E., Claria, J. J., Dottori, H., Santos, Jr., J. F. C., and Piatti, A. E. (1996). Integrated UBV Photometry of 624 Star Clusters and Associations in the Large Magellanic Cloud. ApJS, 102:57. 53

Bica, E. L. D., Schmitt, H. R., Dutra, C. M., and Oliveira, H. L. (1999). A Revised and Extended Catalog of Magellanic System Clusters, Associations, and Emission Nebulae. II. The Large Magellanic Cloud. AJ, 117:238–246. 3, 53, 63

Binney, J. and Tremaine, S. (1987). *Galactic dynamics*. 4

Binney, J. and Tremaine, S. (2008). *Galactic Dynamics: Second Edition*. Princeton University Press. 4, 6

Bok, B. J. (1966). Magellanic Clouds. ARA&A, 4:95. 1

Bolte, M. (1989). Mass segregation in the globular cluster M30. ApJ, 341:168–174. 10

Bonnell, I. A. and Bate, M. R. (2006). Star formation through gravitational collapse and competitive accretion. MNRAS, 370:488–494. 9

Bonnell, I. A. and Davies, M. B. (1998). Mass segregation in young stellar clusters. MNRAS, 295:691. 5, 8, 39, 73

Brandl, B., Sams, B. J., Bertoldi, F., Eckart, A., Genzel, R., Drapatz, S., Hofmann, R., Loewe, M., and Quirrenbach, A. (1996). Adaptive Optics Near-Infrared Imaging of R136 in 30 Doradus: The Stellar Population of a Nearby Starburst. ApJ, 466:254. 11, 54

Brocato, E., Di Carlo, E., and Menna, G. (2001). Large Magellanic Cloud stellar clusters. I. 21 HST colour magnitude diagrams. A&A, 374:523–539. 76, 77

Cabrera-Ziri, I., Bastian, N., Hilker, M., Davies, B., Schweizer, F., Kruijssen, J. M. D., Mejía-Narváez, A., Niederhofer, F., Brandt, T. D., Rejkuba, M., Bruzual, G., and Magris, G. (2016a). Is the escape velocity in star clusters linked to extended star formation histories? Using NGC 7252: W3 as a test case. MNRAS, 457:809–821. 75

Cabrera-Ziri, I., Bastian, N., Longmore, S. N., Brogan, C., Hollyhead, K., Larsen, S. S., Whitmore, B., Johnson, K., Chandar, R., Henshaw, J. D., Davies, B., and Hibbard, J. E. (2015). Constraining globular cluster formation through studies of young massive clusters - V. ALMA observations of clusters in the Antennae. MNRAS, 448:2224–2231. 67

Cabrera-Ziri, I., Niederhofer, F., Bastian, N., Rejkuba, M., Balbinot, E., Kerzendorf, W. E., Larsen, S. S., Mackey, A. D., Dalessandro, E., Mucciarelli, A., Charbonnel, C., Hilker, M., Gieles, M., and Hénault-Brunet, V. (2016b). No evidence for younger stellar generations within the intermediate-age massive clusters NGC 1783, NGC 1806 and NGC 411. MNRAS, 459:4218–4223. 12

Chantereau, W., Salaris, M., Bastian, N., and Martocchia, S. (2019). Helium enrichment in intermediate-age Magellanic Clouds clusters: towards an ubiquity of multiple stellar populations? MNRAS, 484:5236–5244. 12

Choi, Y., Nidever, D. L., Olsen, K., Blum, R. D., Besla, G., Zaritsky, D., van der Marel, R. P., Bell, E. F., Gallart, C., Cioni, M.-R. L., Johnson, L. C., Vivas, A. K., Saha, A., de Boer, T. J. L., Noël, N. E. D., Monachesi, A., Massana, P., Conn, B. C., Martinez-Delgado, D., Muñoz, R. R., and Stringfellow, G. S. (2018). SMASHing the LMC: A Tidally Induced Warp in the Outer LMC and a Large-scale Reddening Map. ApJ, 866:90. 2

de Bruijne, J., Kohley, R., and Prusti, T. (2010). Gaia: 1,000 million stars with 100 CCD detectors. In *Space Telescopes and Instrumentation 2010: Optical, Infrared, and Millimeter Wave*, volume 7731 of Proc. SPIE, page 77311C. 70

de Grijs, R., Gilmore, G. F., Johnson, R. A., and Mackey, A. D. (2002a). Mass segregation in young compact star clusters in the Large Magellanic Cloud - II. Mass functions. MNRAS, 331:245–258. 11, 54

de Grijs, R., Gilmore, G. F., Mackey, A. D., Wilkinson, M. I., Beaulieu, S. F., Johnson, R. A., and Santiago, B. X. (2002b). Mass segregation in young compact clusters in the Large Magellanic Cloud - III. Implications for the initial mass function. MNRAS, 337:597–608. 36

Dieball, A., Müller, H., and Grebel, E. K. (2002). A statistical study of binary and multiple clusters in the LMC. A&A, 391:547–564. 3

Dirsch, B., Richtler, T., Gieren, W. P., and Hilker, M. (2000). Age and metallicity for six LMC clusters and their surrounding field population. A&A, 360:133–160. 40

Dolphin, A. E. (2000a). The Charge-Transfer Efficiency and Calibration of WFPC2. PASP, 112:1397–1410. 27, 28

Dolphin, A. E. (2000b). WFPC2 Stellar Photometry with HSTPHOT. PASP, 112:1383–1396. 25, 26, 27, 41, 54, 73

Dressel, L. (2017). *Wide Field Camera 3 Instrument Handbook*. 70

Ekström, S., Georgy, C., Eggenberger, P., Meynet, G., Mowlavi, N., Wyttenbach, A., Granada, A., Decressin, T., Hirschi, R., Frischknecht, U., Charbonnel, C., and

Maeder, A. (2012). Grids of stellar models with rotation. I. Models from 0.8 to 120 M_{sun} at solar metallicity (Z = 0.014). A&A, 537:A146. 71

Elson, R. A. W. (1991). The structure and evolution of rich star clusters in the Large Magellanic Cloud. ApJS, 76:185–214. 31, 76

Elson, R. A. W., Fall, S. M., and Freeman, K. C. (1987). The structure of young star clusters in the Large Magellanic Cloud. ApJ, 323:54–78. 7, 8, 36, 40, 42, 45, 74, 81, 88, 89

Elson, R. A. W., Freeman, K. C., and Lauer, T. R. (1989). Core expansion in young star clusters in the Large Magellanic Cloud. ApJ, 347:L69–L71. 7

Evans, C. J., Bastian, N., Beletsky, Y., Brott, I., Cantiello, M., Clark, J. S., Crowther, P. A., de Koter, A., de Mink, S. E., Dufton, P. L., Dunstall, P., Gieles, M., Gräfener, G., Hénault-Brunet, V., Herrero, A., Howarth, I. D., Langer, N., Lennon, D. J., Maíz Apellániz, J., Markova, N., Najarro, F., Puls, J., Sana, H., Simón-Díaz, S., Smartt, S. J., Stroud, V. E., Taylor, W. D., Trundle, C., van Loon, J. T., Vink, J. S., and Walborn, N. R. (2010). The VLT-FLAMES Tarantula Survey. In de Grijs, R. and Lépine, J. R. D., editors, *Star Clusters: Basic Galactic Building Blocks Throughout Time and Space*, volume 266 of *IAU Symposium*, pages 35–40. 78

Evans, C. J., Lennon, D. J., Smartt, S. J., and Trundle, C. (2006). The VLT-FLAMES survey of massive stars: observations centered on the Magellanic Cloud clusters NGC 330, NGC 346, NGC 2004, and the N11 region. A&A, 456:623–638. 78

Evans, II, N. J., Dunham, M. M., Jørgensen, J. K., Enoch, M. L., Merín, B., van Dishoeck, E. F., Alcalá, J. M., Myers, P. C., Stapelfeldt, K. R., Huard, T. L., Allen, L. E., Harvey, P. M., van Kempen, T., Blake, G. A., Koerner, D. W., Mundy, L. G., Padgett, D. L., and Sargent, A. I. (2009). The Spitzer c2d Legacy Results: Star-Formation Rates and Efficiencies; Evolution and Lifetimes. ApJS, 181:321–350. 9

Farouki, R. T., Hoffman, G. L., and Salpeter, E. E. (1983). The collapse and violent relaxation of N-body systems - Mass segregation and the secondary maximum. ApJ, 271:11–21. 9, 10

Fischer, P., Pryor, C., Murray, S., Mateo, M., and Richtler, T. (1998). Mass segregation in young Large Magellanic Cloud clusters. I - NGC 2157. AJ, 115:592. 67

Gaia Collaboration, Brown, A. G. A., Vallenari, A., Prusti, T., de Bruijne, J. H. J., Babusiaux, C., Bailer-Jones, C. A. L., Biermann, M., Evans, D. W., Eyer, L., Jansen, F., Jordi, C., Klioner, S. A., Lammers, U., Lindegren, L., Luri, X., Mignard, F., Panem, C., Pourbaix, D., Randich, S., Sartoretti, P., Siddiqui, H. I., Soubiran, C., van Leeuwen, F., Walton, N. A., Arenou, F., Bastian, U., Cropper, M., Drimmel, R., Katz, D., Lattanzi, M. G., Bakker, J., Cacciari, C., Castañeda, J., Chaoul, L., Cheek, N., De Angeli, F., Fabricius, C., Guerra, R., Holl, B., Masana, E., Messineo, R., Mowlavi, N., Nienartowicz, K., Panuzzo, P., Portell, J., Riello, M., Seabroke, G. M., Tanga, P., Thévenin, F., Gracia-Abril, G., Comoretto, G., Garcia-Reinaldos, M., Teyssier, D., Altmann, M., Andrae, R., Audard, M., Bellas-Velidis, I., Benson, K., Berthier, J., Blomme, R., Burgess, P., Busso, G., Carry, B., Cellino, A., Clementini, G., Clotet, M., Creevey, O., Davidson, M., De Ridder, J., Delchambre, L., Dell'Oro, A., Ducourant, C., Fernández-Hernández, J., Fouesneau, M., Frémat, Y., Galluccio, L., García-Torres, M., González-Núñez, J., González-Vidal, J. J., Gosset, E., Guy, L. P., Halbwachs, J. L., Hambly, N. C., Harrison, D. L., Hernández, J., Hestroffer, D., Hodgkin, S. T., Hutton, A., Jasniewicz, G., Jean-Antoine-Piccolo, A., Jordan, S., Korn, A. J., Krone-Martins, A., Lanzafame, A. C., Lebzelter, T., Löffler, W., Manteiga, M., Marrese, P. M., Martín-Fleitas, J. M., Moitinho, A., Mora, A., Muinonen, K., Osinde, J., Pancino, E., Pauwels, T., Petit, J. M., Recio-Blanco, A., Richards, P. J., Rimoldini, L., Robin, A. C., Sarro, L. M., Siopis, C., Smith, M., Sozzetti, A., Süveges, M., Torra, J., van Reeven, W., Abbas, U., Abreu Aramburu, A., Accart, S., Aerts, C., Altavilla, G., Álvarez, M. A., Alvarez, R., Alves, J., Anderson, R. I., Andrei, A. H., Anglada Varela, E., Antiche, E., Antoja, T., Arcay, B., Astraatmadja, T. L., Bach, N., Baker, S. G., Balaguer-Núñez, L., Balm, P., Barache, C., Barata, C., Barbato, D., Barblan, F., Barklem, P. S., Barrado, D., Barros, M.,

Barstow, M. A., Bartholomé Muñoz, S., Bassilana, J. L., Becciani, U., Bellazzini, M., Berihuete, A., Bertone, S., Bianchi, L., Bienaymé, O., Blanco-Cuaresma, S., Boch, T., Boeche, C., Bombrun, A., Borrachero, R., Bossini, D., Bouquillon, S., Bourda, G., Bragaglia, A., Bramante, L., Breddels, M. A., Bressan, A., Brouillet, N., Brüsemeister, T., Brugaletta, E., Bucciarelli, B., Burlacu, A., Busonero, D., Butkevich, A. G., Buzzi, R., Caffau, E., Cancelliere, R., Cannizzaro, G., Cantat-Gaudin, T., Carballo, R., Carlucci, T., Carrasco, J. M., Casamiquela, L., Castellani, M., Castro-Ginard, A., Charlot, P., Chemin, L., Chiavassa, A., Cocozza, G., Costigan, G., Cowell, S., Crifo, F., Crosta, M., Crowley, C., Cuypers, J., Dafonte, C., Damerdji, Y., Dapergolas, A., David, P., David, M., de Laverny, P., De Luise, F., De March, R., de Martino, D., de Souza, R., de Torres, A., Debosscher, J., del Pozo, E., Delbo, M., Delgado, A., Delgado, H. E., Di Matteo, P., Diakite, S., Diener, C., Distefano, E., Dolding, C., Drazinos, P., Durán, J., Edvardsson, B., Enke, H., Eriksson, K., Esquej, P., Eynard Bontemps, G., Fabre, C., Fabrizio, M., Faigler, S., Falcão, A. J., Farràs Casas, M., Federici, L., Fedorets, G., Fernique, P., Figueras, F., Filippi, F., Findeisen, K., Fonti, A., Fraile, E., Fraser, M., Frézouls, B., Gai, M., Galleti, S., Garabato, D., García-Sedano, F., Garofalo, A., Garralda, N., Gavel, A., Gavras, P., Gerssen, J., Geyer, R., Giacobbe, P., Gilmore, G., Girona, S., Giuffrida, G., Glass, F., Gomes, M., Granvik, M., Gueguen, A., Guerrier, A., Guiraud, J., Gutiérrez-Sánchez, R., Haigron, R., Hatzidimitriou, D., Hauser, M., Haywood, M., Heiter, U., Helmi, A., Heu, J., Hilger, T., Hobbs, D., Hofmann, W., Holland, G., Huckle, H. E., Hypki, A., Icardi, V., Janßen, K., Jevardat de Fombelle, G., Jonker, P. G., Juhász, Á. L., Julbe, F., Karampelas, A., Kewley, A., Klar, J., Kochoska, A., Kohley, R., Kolenberg, K., Kontizas, M., Kontizas, E., Koposov, S. E., Kordopatis, G., Kostrzewa-Rutkowska, Z., Koubsky, P., Lambert, S., Lanza, A. F., Lasne, Y., Lavigne, J. B., Le Fustec, Y., Le Poncin-Lafitte, C., Lebreton, Y., Leccia, S., Leclerc, N., Lecoeur-Taibi, I., Lenhardt, H., Leroux, F., Liao, S., Licata, E., Lindstrøm, H. E. P., Lister, T. A., Livanou, E., Lobel, A., López, M., Managau, S., Mann, R. G., Mantelet, G., Marchal, O., Marchant, J. M., Marconi, M., Marinoni, S., Marschalkó, G., Marshall, D. J., Martino, M., Marton, G., Mary, N., Massari, D., Matijevič, G., Mazeh, T., McMillan, P. J., Messina, S., Michalik, D., Millar, N. R., Molina, D., Molinaro, R., Molnár, L., Montegriffo, P., Mor, R., Morbidelli, R., Morel, T., Morris,

D., Mulone, A. F., Muraveva, T., Musella, I., Nelemans, G., Nicastro, L., Noval, L., O'Mullane, W., Ordénovic, C., Ordóñez-Blanco, D., Osborne, P., Pagani, C., Pagano, I., Pailler, F., Palacin, H., Palaversa, L., Panahi, A., Pawlak, M., Piersimoni, A. M., Pineau, F. X., Plachy, E., Plum, G., Poggio, E., Poujoulet, E., Prša, A., Pulone, L., Racero, E., Ragaini, S., Rambaux, N., Ramos-Lerate, M., Regibo, S., Reylé, C., Riclet, F., Ripepi, V., Riva, A., Rivard, A., Rixon, G., Roegiers, T., Roelens, M., Romero-Gómez, M., Rowell, N., Royer, F., Ruiz-Dern, L., Sadowski, G., Sagristà Sellés, T., Sahlmann, J., Salgado, J., Salguero, E., Sanna, N., Santana-Ros, T., Sarasso, M., Savietto, H., Schultheis, M., Sciacca, E., Segol, M., Segovia, J. C., Ségransan, D., Shih, I. C., Siltala, L., Silva, A. F., Smart, R. L., Smith, K. W., Solano, E., Solitro, F., Sordo, R., Soria Nieto, S., Souchay, J., Spagna, A., Spoto, F., Stampa, U., Steele, I. A., Steidelmüller, H., Stephenson, C. A., Stoev, H., Suess, F. F., Surdej, J., Szabados, L., Szegedi-Elek, E., Tapiador, D., Taris, F., Tauran, G., Taylor, M. B., Teixeira, R., Terrett, D., Teyssand ier, P., Thuillot, W., Titarenko, A., Torra Clotet, F., Turon, C., Ulla, A., Utrilla, E., Uzzi, S., Vaillant, M., Valentini, G., Valette, V., van Elteren, A., Van Hemelryck, E., van Leeuwen, M., Vaschetto, M., Vecchiato, A., Veljanoski, J., Viala, Y., Vicente, D., Vogt, S., von Essen, C., Voss, H., Votruba, V., Voutsinas, S., Walmsley, G., Weiler, M., Wertz, O., Wevers, T., Wyrzykowski, Ł., Yoldas, A., Žerjal, M., Ziaeepour, H., Zorec, J., Zschocke, S., Zucker, S., Zurbach, C., and Zwitter, T. (2018). Gaia Data Release 2. Summary of the contents and survey properties. A&A, 616:A1. 66

Georgy, C., Ekström, S., Granada, A., Meynet, G., Mowlavi, N., Eggenberger, P., and Maeder, A. (2013). Populations of rotating stars. I. Models from 1.7 to 15 M_{sun} at Z = 0.014, 0.006, and 0.002 with Ω/Ω_{crit} between 0 and 1. A&A, 553:A24. 71

Georgy, C., Granada, A., Ekström, S., Meynet, G., Anderson, R. I., Wyttenbach, A., Eggenberger, P., and Maeder, A. (2014). Populations of rotating stars. III. SYCLIST, the new Geneva population synthesis code. A&A, 566:A21. 37, 77

Girardi, L., Rubele, S., and Kerber, L. (2009). Discovery of two distinct red clumps in NGC 419: a rare snapshot of a cluster at the onset of degeneracy. MNRAS,

394:L74–L78. 67

Glatt, K., Grebel, E. K., and Koch, A. (2010). Ages and luminosities of young SMC/LMC star clusters and the recent star formation history of the Clouds. A&A, 517:A50. 3

Gouliermis, D. A., de Grijs, R., and Xin, Y. (2009). A New Diagnostic Method for Assessment of Stellar Stratification in Star Clusters. ApJ, 692:1678–1689. 10

Gratton, R. G., Carretta, E., and Bragaglia, A. (2012). Multiple populations in globular clusters. Lessons learned from the Milky Way globular clusters. A&A Rev., 20:50. 67

Grebel, E. K. (2016). Globular Clusters in the Local Group. In Meiron, Y., Li, S., Liu, F. K., and Spurzem, R., editors, *Star Clusters and Black Holes in Galaxies across Cosmic Time*, volume 312 of *IAU Symposium*, pages 157–170. 3

Gunn, J. E., Carr, M., Rockosi, C., Sekiguchi, M., Berry, K., Elms, B., de Haas, E., Ivezić, Ž., Knapp, G., Lupton, R., Pauls, G., Simcoe, R., Hirsch, R., Sanford, D., Wang, S., York, D., Harris, F., Annis, J., Bartozek, L., Boroski, W., Bakken, J., Haldeman, M., Kent, S., Holm, S., Holmgren, D., Petravick, D., Prosapio, A., Rechenmacher, R., Doi, M., Fukugita, M., Shimasaku, K., Okada, N., Hull, C., Siegmund, W., Mannery, E., Blouke, M., Heidtman, D., Schneider, D., Lucinio, R., and Brinkman, J. (1998). The Sloan Digital Sky Survey Photometric Camera. AJ, 116:3040–3081. 70

Hillenbrand, L. A. (1997). On the Stellar Population and Star-Forming History of the Orion Nebula Cluster. AJ, 113:1733–1768. 10

Hillenbrand, L. A. and Hartmann, L. W. (1998). A Preliminary Study of the Orion Nebula Cluster Structure and Dynamics. ApJ, 492:540–553. 10

Holtzman, J. A., Burrows, C. J., Casertano, S., Hester, J. J., Trauger, J. T., Watson, A. M., and Worthey, G. (1995a). The Photometric Performance and Calibration of WFPC2. PASP, 107:1065. 68

Holtzman, J. A., Hester, J. J., Casertano, S., Trauger, J. T., Watson, A. M., Ballester, G. E., Burrows, C. J., Clarke, J. T., Crisp, D., Evans, R. W., Gallagher, III, J. S., Griffiths, R. E., Hoessel, J. G., Matthews, L. D., Mould, J. R., Scowen, P. A., Stapelfeldt, K. R., and Westphal, J. A. (1995b). The performance and calibration of WFPC2 on the Huble Space Telescope. PASP, 107:156–178. 27, 73

Inno, L., Bono, G., Matsunaga, N., Fiorentino, G., Marconi, M., Lemasle, B., da Silva, R., Soszyński, I., Udalski, A., Romaniello, M., and Rix, H.-W. (2016). The Panchromatic View of the Magellanic Clouds from Classical Cepheids. I. Distance, Reddening, and Geometry of the Large Magellanic Cloud Disk. ApJ, 832:176. 2, 71

Kallivayalil, N., van der Marel, R. P., Anderson, J., Besla, G., and Alcock, C. (2009). New analysis of the proper motions of the Magellanic Clouds using HST/WFPC2. In Van Loon, J. T. and Oliveira, J. M., editors, *The Magellanic System: Stars, Gas, and Galaxies*, volume 256 of *IAU Symposium*, pages 93–98. 2

Keller, S. C., Bessell, M. S., and Da Costa, G. S. (2000). Wide Field Planetary Camera 2 Imaging of Young Clusters in the Magellanic Clouds. AJ, 119:1748–1759. 76

Khalisi, E., Amaro-Seoane, P., and Spurzem, R. (2007). A comprehensive NBODY study of mass segregation in star clusters: energy equipartition and escape. MNRAS, 374:703–720. 9

King, I. (1962). The structure of star clusters. I. an empirical density law. AJ, 67:471. 6, 7, 35, 36, 40, 54, 81

King, I. R. (1965). The structure of star clusters. II. Steady-state velocity distributions. AJ, 70:376. 6, 7

King, I. R. (1966). The structure of star clusters. III. Some simple dynamical models. AJ, 71:64. 6, 7, 74

King, I. R. (2008). The Simple Underlying Dynamics of Globular Clusters. In Vesperini, E., Giersz, M., and Sills, A., editors, *Dynamical Evolution of Dense Stellar Systems*, volume 246 of *IAU Symposium*, pages 131–140. 5, 6, 11, 73

Kontizas, E. and Kontizas, M. (1983). Observed radii and structural parameters of clusters in the SMC. II. A&AS, 52:143–159. 7

Kontizas, E., Kontizas, M., Sedmak, G., and Smareglia, R. (1989). Ellipticities at R(h) of LMC star clusters. AJ, 98:590–595. 11

Kontizas, M. (1984). Dynamical parameters of 43 old and young clusters in the SMC. A&A, 131:58–62. 7

Kontizas, M., Chrysovergis, M., and Kontizas, E. (1987). Observed dynamical parameters of the disk clusters of the LMC. I. A&AS, 68:147–169. 7, 51

Kontizas, M., Hatzidimitriou, D., Bellas-Velidis, I., Gouliermis, D., Kontizas, E., and Cannon, R. D. (1998). Mass segregation in two young clusters in the Large Magellanic Cloud: SL 666 and NGC 2098. A&A, 336:503–517. 8

Kontizas, M. and Kontizas, E. (1991). Are there two disk star cluster systems in the LMC? In Janes, K., editor, *The Formation and Evolution of Star Clusters*, volume 13 of *Astronomical Society of the Pacific Conference Series*, pages 407–409. 3

Kontizas, M., Kontizas, E., and Michalitsianos, A. G. (1993). Radial distribution of metallicity in the LMC cluster systems. A&A, 269:107–110. 3

Kontizas, M., Morgan, D. H., Hatzidimitriou, D., and Kontizas, E. (1990). The cluster system of the Large Magellanic Cloud. A&AS, 84:527–547. 3, 66

Krumholz, M. R., McKee, C. F., and Klein, R. I. (2005). The formation of stars by gravitational collapse rather than competitive accretion. Nature, 438:332–334. 9

Lada, C. J. and Lada, E. A. (2003). Embedded Clusters in Molecular Clouds. ARA&A, 41:57–115. 3, 9, 65

Li, C., de Grijs, R., and Deng, L. (2013). The binary fractions in the massive young Large Magellanic Cloud star clusters NGC 1805 and NGC 1818. MNRAS, 436:1497–1512. 77

Li, C., de Grijs, R., and Deng, L. (2014). The exclusion of a significant range of ages in a massive star cluster. Nature, 516:367–369. 12

Li, C., de Grijs, R., Deng, L., Geller, A. M., Xin, Y., Hu, Y., and Faucher-Giguère, C.-A. (2016). Formation of new stellar populations from gas accreted by massive young star clusters. Nature, 529:502–504. 12

Lightman, A. P. and Shapiro, S. L. (1978). The dynamical evolution of globular clusters. *Reviews of Modern Physics*, 50:437–481. 8, 39

Livanou, E., Dapergolas, A., Kontizas, M., Nordström, B., Kontizas, E., Andersen, J., Dirsch, B., and Karampelas, A. (2013). Age - metallicity relation in the Magellanic Clouds clusters. A&A, 554:A16. 71

Mackey, A. D. and Gilmore, G. F. (2003). Surface brightness profiles and structural parameters for 53 rich stellar clusters in the Large Magellanic Cloud. MNRAS, 338:85–119. 28, 33, 34, 40, 53, 59, 60, 61, 62, 89

Mackey, A. D., Wilkinson, M. I., Davies, M. B., and Gilmore, G. F. (2008). Black holes and core expansion in massive star clusters. MNRAS, 386:65–95. 73

Marigo, P., Girardi, L., Bressan, A., Groenewegen, M. A. T., Silva, L., and Granato, G. L. (2008). Evolution of asymptotic giant branch stars. II. Optical to far-infrared isochrones with improved TP-AGB models. A&A, 482:883–905. 36, 64

Marigo, P., Girardi, L., Bressan, A., Rosenfield, P., Aringer, B., Chen, Y., Dussin, M., Nanni, A., Pastorelli, G., Rodrigues, T. S., Trabucchi, M., Bladh, S., Dalcanton, J., Groenewegen, M. A. T., Montalbán, J., and Wood, P. R. (2017). A New Generation of PARSEC-COLIBRI Stellar Isochrones Including the TP-AGB Phase. ApJ, 835:77. 36, 71, 76

Markwardt, C. B. (2009). Non-linear Least-squares Fitting in IDL with MPFIT. In Bohlender, D. A., Durand, D., and Dowler, P., editors, *Astronomical Data*

Analysis Software and Systems XVIII, volume 411 of *Astronomical Society of the Pacific Conference Series*, page 251. 35, 42

Martins, F. and Palacios, A. (2013). A comparison of evolutionary tracks for single Galactic massive stars. A&A, 560:A16. 70

Mathewson, D. S. and Ford, V. L. (1984). H I surveys of the Magellanic System. In van den Bergh, S. and de Boer, K. S. D., editors, *Structure and Evolution of the Magellanic Clouds*, volume 108 of *IAU Symposium*, pages 125–136. 1

McLaughlin, D. E. and van der Marel, R. P. (2005). Resolved Massive Star Clusters in the Milky Way and Its Satellites: Brightness Profiles and a Catalog of Fundamental Parameters. ApJS, 161:304–360. 40, 53

McMaster, M. and et al. (2008). *Wide Field and Planetary Camera 2 Instrument Handbook v. 10.0*. 16

McMillan, S., Vesperini, E., and Kruczek, N. (2015). Rapid Mass Segregation in Massive Star Clusters. *Highlights of Astronomy*, 16:259–261. 5

Meylan, G. and Heggie, D. C. (1997). Internal dynamics of globular clusters. A&A Rev., 8:1–143. 39, 73

Mould, J. R., Xystus, D. A., and Da Costa, G. S. (1993). The age of the Large Magellanic Cloud cluster NGC 2031. ApJ, 408:108–114. 70

Niederhofer, F., Hilker, M., Bastian, N., and Silva-Villa, E. (2015). No evidence for significant age spreads in young massive LMC clusters. A&A, 575:A62. 40, 67, 76, 77

Nikolov, G. (2018a). Mimicking multiple stellar populations. Mem. Soc. Astron. Italiana, 89:85. 26, 79, 84

Nikolov, G., Dapergolas, A., Kontizas, M., and Golev, V. (2010a). Indication of Stellar Stratification in Star Clusters in the Magellanic Clouds. *Publications de l'Observatoire Astronomique de Beograd*, 90:73–76. 62, 83

Nikolov, G., Dapergolas, A., Kontizas, M., Golev, V., and Belcheva, M. (2010b). Density profiles of populous star clusters in the Magellanic Clouds. *Bulgarian Astronomical Journal*, 14:43. 62, 83

Nikolov, G., Dapergolas, A., Kontizas, M., Golev, V., and Belcheva, M. (2010c). Density Profiles of Star Clusters in the Magellanic Clouds. In Tsinganos, K., Hatzidimitriou, D., and Matsakos, T., editors, *9th International Conference of the Hellenic Astronomical Society*, volume 424 of *Astronomical Society of the Pacific Conference Series*, page 236. 62, 83

Nikolov, G., Golev, V., Kontizas, M., Dapergolas, A., Kontizas, E., and Bellas-Velidis, I. (2009a). The distortions in the density profiles in LMC clusters NGC 1850, NGC 2214 and BSDL 103. *Annual of Sofia University "St. Kliment Ohridski", Faculty of Physics*. 62, 83

Nikolov, G., Kontizas, M., Dapergolas, A., Kontizas, E., Golev, V., and Bellas-Velidis, I. (2009b). The distortions in the density profiles of star clusters in the Magellanic Clouds. *Publications of the Astronomical Society "Rudjer Boskovic"*, 9:363–368. 78, 83

Nikolov, G. and Markov, H. (2019). Characterising lmc star cluster ngc 2004. *AIP Conference Proceedings*, 2075(1):090005. 79, 84

Nikolov, G. B. (2018b). Precise astrometry from half-century long observations of star cluster M 15. *Astronomical and Astrophysical Transactions*, 30:417–420. 30, 84

Nikolov, G. B., Kontizas, M., Dapergolas, A., Belcheva, M. K., Golev, V., and Bellas-Velidis, I. (2012). Indication of Mass Segregation in LMC Star Clusters. *Astrophysics and Space Science Proceedings*, 29:227. 62, 83

Nikolov, G. B., Kontizas, M., Dapergolas, A., Belcheva, M. K., Golev, V. K., and Ioannis Bellas-Velidis, I. (2013). Distribution of stars in three Magellanic Clouds star clusters NGC 1754, NGC 2005, NGC 2019. *Bulgarian Astronomical Journal*, 19:9. 83

Olsen, K. A. G., Hodge, P. W., Mateo, M., Olszewski, E. W., Schommer, R. A., Suntzeff, N. B., and Walker, A. R. (1998). HSTcolour-magnitude diagrams of six old globular clusters in the LMC. MNRAS, 300:665–685. 3, 40, 53

Pandey, A. K., Mahra, H. S., and Sagar, R. (1992). Effect of mass segregation on mass function of young open clusters. *Bulletin of the Astronomical Society of India*, 20:287–295. 10

Piatti, A. E. (2018). Sizing the star cluster population of the Large Magellanic Cloud. MNRAS, 475:2553–2559. 3

Pietrzyński, G., Graczyk, D., Gieren, W., Thompson, I. B., Pilecki, B., Udalski, A., Soszyński, I., Kozłowski, S., Konorski, P., Suchomska, K., Bono, G., Moroni, P. G. P., Villanova, S., Nardetto, N., Bresolin, F., Kudritzki, R. P., Storm, J., Gallenne, A., Smolec, R., Minniti, D., Kubiak, M., Szymański, M. K., Poleski, R., Wyrzykowski, Ł., Ulaczyk, K., Pietrukowicz, P., Górski, M., and Karczmarek, P. (2013). An eclipsing-binary distance to the Large Magellanic Cloud accurate to two per cent. Nature, 495:76–79. 2

Piotto, G., King, I. R., Djorgovski, S. G., Sosin, C., Zoccali, M., Saviane, I., De Angeli, F., Riello, M., Recio-Blanco, A., Rich, R. M., Meylan, G., and Renzini, A. (2002). HST color-magnitude diagrams of 74 galactic globular clusters in the HST F439W and F555W bands. A&A, 391:945–965. 28

Portegies Zwart, S. F. and Chen, H.-C. (2008). Reconstructing the Initial Relaxation Time of Young Star Clusters in the Large Magellanic Cloud: The Evolution of Star Clusters. In de Koter, A., Smith, L. J., and Waters, L. B. F. M., editors, *Mass Loss from Stars and the Evolution of Stellar Clusters*, volume 388 of *Astronomical Society of the Pacific Conference Series*, page 329. 5

Richtler, T., Fischer, P., Mateo, M., Pryor, C., and Murray, S. (1997). Mass segregation in dynamically unevolved LMC star clusters. In Schielicke, R. E., editor, *Astronomische Gesellschaft Abstract Series*, volume 13 of *Astronomische Gesellschaft Abstract Series*, page 75. 51

Santos-Silva, T. and Gregorio-Hetem, J. (2012). Characterisation of young stellar clusters. A&A, 547:A107. 65

Schechter, P. L., Mateo, M., and Saha, A. (1993). DOPHOT, a CCD photometry program: Description and tests. PASP, 105:1342–1353. 33

Shaklan, S., Sharman, M. C., and Pravdo, S. H. (1995). High-precision measurement of pixel positions in a charge-coupled device. Appl. Opt., 34:6672. 27

Simon, J. D., Bolatto, A. D., Whitney, B. A., Robitaille, T. P., Shah, R. Y., Makovoz, D., Stanimirović, S., Barbá, R. H., and Rubio, M. (2007). The Spitzer Survey of the Small Magellanic Cloud: Discovery of Embedded Protostars in the H II Region NGC 346. ApJ, 669:327–336. 8

Spitzer, L. (1987). *Dynamical evolution of globular clusters*. 39

Spitzer, Jr., L. (1968). Astronomical Research with the Large Space Telescope. *Science*, 161:225–229. 15

Spitzer, Jr., L. (1969). Equipartition and the Formation of Compact Nuclei in Spherical Stellar Systems. ApJ, 158:L139. 9

Spitzer, Jr., L. and Shull, J. M. (1975). Random gravitational encounters and the evolution of spherical systems. VII - Systems with several mass groups. ApJ, 201:773–782. 5

Spurzem, R. and Takahashi, K. (1995). Comparison between Fokker-Planck and gaseous models of star clusters in the multi-mass case revisited. MNRAS, 272:772–784. 9

Stetson, P. B. (1987). DAOPHOT - A computer program for crowded-field stellar photometry. PASP, 99:191–222. 25

Stolte, A., Brandner, W., Brandl, B., and Zinnecker, H. (2006). The Secrets of the Nearest Starburst Cluster. II. The Present-Day Mass Function in NGC 3603. AJ, 132:253–270. 10

Subramaniam, A., Sagar, R., and Bhatt, H. C. (1993). Spatial Distribution of Stellar Mass in the Large Magellanic Cloud Star Clusters. A&A, 273:100. 8, 51

Taylor, M. B. (2005). TOPCAT & STIL: Starlink Table/VOTable Processing Software. In Shopbell, P., Britton, M., and Ebert, R., editors, *Astronomical Data Analysis Software and Systems XIV*, volume 347 of *Astronomical Society of the Pacific Conference Series*, page 29. 76

Weidner, C., Bonnell, I. A., and Zinnecker, H. (2010). Super Star Clusters Versus OB Associations. ApJ, 724:1503–1508. 3

Westerlund, B. (1961). Population I in the Large Magellanic Cloud. *Uppsala Astronomical Observatory Annals*, 5:1–28. 8

Westerlund, B. E. (1990). The Magellanic Clouds - Their evolution, structure and composition. A&A Rev., 2:29–78. 2

Wolf, M. J., Drory, N., Gebhardt, K., and Hill, G. J. (2007). Ages and Metallicities of Extragalactic Globular Clusters from Spectral and Photometric Fits of Stellar Population Synthesis Models. ApJ, 655:179–211. 40